

# **A Study on Mechanisms for Multicopter Consisting of Passive Joints Capable of Plane Perching and Rough Terrain Landing**

(不整地への着陸および平面への  
パーチング動作ができる受動関節で構成された  
マルチコプターのための着陸機構の研究)

by

Xu Maozheng

Graduate School of Engineering  
Hiroshima University  
March, 2022



# Contents

1. Introduction . . . . .	1
1.1 Background . . . . .	3
1.1.1 Concept of perching and landing . . . . .	3
1.1.2 Device for a multicopter capable of perching . . . . .	5
1.1.3 Device for multicopter capable of rough terrain landing . . . . .	7
1.2 Outline of thesis . . . . .	9
2. Development of an underactuated parallel-link gripper for multicopter plane perching . . . . .	11
2.1 Underactuated parallel-link gripper prototype (multicopter included) . . . . .	12
2.2 Motion of perching on plane . . . . .	13
2.3 Available condition for stable perching . . . . .	13
2.3.1 Anatomy of the static model . . . . .	15
2.3.2 Target thickness classification discussion . . . . .	17
2.3.3 Determination of the COG of each link . . . . .	22
2.3.4 Classification discussion of the location of the COG . . . . .	23
2.3.5 Categorize and integrate various situations . . . . .	25
2.4 Perching state judgment . . . . .	27
2.4.1 The friction cone theory . . . . .	27
2.4.2 Judgment based on friction cone theory . . . . .	29
2.4.3 Necessary contact condition for perching . . . . .	31
2.5 Experiment . . . . .	33
2.5.1 Friction coefficient measuring experiment. . . . .	33
2.5.2 Perching experiment . . . . .	34
2.5.3 Takeoff-perching experiment . . . . .	36
2.6 Concluding Remark . . . . .	37

3. Development of a passive skid for multicopter landing on rough terrain . . . . .	39
3.1 Skid structure and basic landing device . . . . .	39
3.2 Range of slopes for available landing . . . . .	41
3.3 Frictional torque of passive joint . . . . .	46
3.4 Prototype of the entire device . . . . .	49
3.5 Experiments . . . . .	50
3.5.1 Experimental settings . . . . .	50
3.5.2 Maintenance of multicopter horizontal states . . . . .	51
3.5.3 Verification of frictional torque of passive joint . . . . .	52
3.5.4 Landing experiment on rough plane . . . . .	54
3.6 Concluding Remark . . . . .	54
4. Analysis of a multicopter carried with passive skid for rough terrain landing . .	56
4.1 Reconstruction of the static model . . . . .	57
4.2 The capable range of slope for landing . . . . .	58
4.2.1 Judgment of the ground-contacting state . . . . .	61
4.2.2 Condition of non-tilting . . . . .	63
4.3 Numerical analysis and theoretical value . . . . .	65
4.4 Experiment . . . . .	68
4.4.1 Experimental environment . . . . .	68
4.4.2 Experimental result of arbitrary area . . . . .	69
4.4.3 Experimental result of area near the border . . . . .	71
4.5 Concluding Remark . . . . .	74
5. Conclusion . . . . .	76
Bibliography . . . . .	78
Acknowledgement . . . . .	94

## List of Figures

1.1	Concept of perching and landing. . . . .	4
1.2	Multicopter with simple underactuated device can perch on veranda easily for delivery, security monitoring, etc. . . . .	6
1.3	(a).Normal multicopters utilize electrical skid for landing or perching; (b). Although, when a multicopter carried with an electrical arm and skid can achieve both catching (or grasping) and landing, it consumes much more energy, and loading batteries also increases the weight of the entire device; (c). Based on the arm-attached multicopter, the idea of substituting an underactuated skid with an electrical skid for landing on rough terrain is performed.	8
2.1	Multicopter carried with the proposed device successful perches on several objects: (a) handrail. (b) chair. (c) desk. (d) ladder. (e) a book held by a person. (f) is the prototype of the proposed device. . . . .	12
2.2	Perching process of the underactuated parallel-link-passive gripper. . . . .	14
2.3	Static model of the gripper device. . . . .	15
2.4	Definition of $L_0$ , $a$ , and $b$ . . . . .	17
2.5	Situation analysis of $L \leq L_0$ . . . . .	18
2.6	Situation analysis of $L > L_0$ . . . . .	19
2.7	Schematic diagram of center of gravity (COG) of Link 1, Link2, Link3 and Link4. . . . .	21
2.8	Factor of the Position of the COG. . . . .	24
2.9	Categorize and integrate various situations. . . . .	26
2.10	Concept of the friction cone. . . . .	28
2.11	Theoretical value conclusion when value of $s$ varies. . . . .	31

2.12	Necessary contact condition for perching. . . . .	32
2.13	The measurement of the friction coefficient . . . . .	33
2.14	Comparison of theoretical value and experimental value. . . . .	35
2.15	The experiment process of takingoff. . . . .	36
2.16	The experiment process of hovering. . . . .	36
2.17	The experiment process of perching. . . . .	37
3.1	Structure of the skid. . . . .	40
3.2	Proposed skid landing flow as seen from direction A. . . . .	41
3.3	Arm and landing flow as seen from direction B. . . . .	41
3.4	Proposed skid structure. . . . .	42
3.5	Inclination $\alpha$ of plane 3 viewed from direction A. . . . .	43
3.6	Inclination $\beta$ of plane 3 viewed from direction B. . . . .	45
3.7	Relationship between plane inclination $\alpha$ and $\beta$ that can land, the range between $\beta_{max}$ and $\beta_{min}$ (range in blue) expresses the cases when the entire device maintain horizontal. . . . .	46
3.8	Static model of the skid and the frictional torque. . . . .	47
3.9	Prototype of the entire device. . . . .	49
3.10	Experimental settings. . . . .	50
3.11	Experimental result (a) Landing on a 120 mm step (b) Landing on a slope of 16 deg (c) 0 deg, 10 deg, 20 deg and 30 deg when $\beta$ is $\beta_{max}$ (d) 0 deg, 10 deg, 20 deg and 30 deg when $\beta$ is $\beta_{min}$ . . . . .	51
3.12	Relationship between incilination $\alpha$ and roll angle and pitch angle of the multicopter based on the result of Figure 3.7. . . . .	52
3.13	Experimental verification of the frictional torque of the passive joint. . . . .	53
3.14	Relationship between the passive joint and the frictional torque. . . . .	54
4.1	Static model of the entire device. . . . .	57
4.2	View of the device from A and B directions. . . . .	59
4.3	The positional relationship between $p_2$ and the slope. . . . .	63

4.4	The positional relationship between $p_{all}$ and $\Delta p_{r1}p_{r2}p_2$ . . . . .	65
4.5	Range of $\alpha$ and $\beta$ under landable conditions. . . . .	66
4.6	The relationship of the inclination angle $\alpha, \beta$ and the angle of robot arm $\theta_1, \theta_2$ when landing is achievable. . . . .	67
4.7	The Experimental environment. (a). is the overview of the experimental environment.(b). and (c). are the view from x and y direction of the environment respectively. . . . .	68
4.8	The selected sample area for experiment. . . . .	69
4.9	Landing situation when $\alpha$ is equal to 0[deg]. . . . .	69
4.10	Landing situation when $\alpha$ is equal to 10[deg]. . . . .	70
4.11	Landing situation when $\alpha$ is equal to 20[deg]. . . . .	70
4.12	Landing situation when $\alpha$ is equal to 30[deg]. . . . .	70
4.13	The enlarged view of the sample area's landing range illustrated in Figure 4.8. . . . .	71
4.14	The selected points near the border for experiment. . . . .	72
4.15	Experiment of the area near the border in Figure 4.5. . . . .	73
4.16	Explanation for the optimal location of the $P_{all}$ and the contact point. . . . .	74

## List of Tables

2.1	Properties of components of the entire system . . . . .	30
2.2	Necessary contact condition for perching. . . . .	32
2.3	Perching experimental result . . . . .	34
4.1	Properties of items of the entire perching system. . . . .	66

# Chapter 1

## Introduction

Multicopters are now utilized frequently in the field owing to their outstanding advantages, such as low weight [1, 2, 3] and low cost [4, 5, 6, 7]. Occasionally, multicopters perform tasks that humans cannot realize with high precision, such as rescue [8, 9, 10, 11, 12, 13, 14], inspection [15, 16, 17], and express delivery [18, 19, 20, 21]. Multicopters equipped with different devices will play different roles in various applications. For example, multicopters carrying monitors are utilized in the fields of rescue and aerial photography [22, 23, 24]; multicopter carrying pesticide spraying devices [25, 26, 27, 28] are utilized in agriculture. However, perching or landing are inevitable challenges regardless of the type of outdoor mission multicopter utilized. For example, when a multicopter is performing surveillance or aerial photography missions at a fixed position with a certain height, it needs to perch there firmly like a bird; similarly, the multicopter needs to land after finishing the missions. In general, landing on a relatively flat ground is the best choice for multicopters. However, when multicopter have to land at a disaster site [29, 30], such as the site of an earthquake, mudslide or tsunami, to transport medical equipment or necessary supplies, a device that can make the multicopter land on a uneven ground, especially on a rough terrain is particularly important. Additionally, when performing the aforementioned tasks, the devices attached to the multicopter that consume less power, are light weight, and require less manipulation, will be the optimal choice.

Perching and landing have a similarity, that is, they both approach the target slowly from the hovering state, and finally attach to the target and remain relatively static state. Both perching and landing is necessary for our studies on multicopter and practically, sev-

eral researches have been carried out in the perching field. This includes the modeling and simulation of perching [31, 32, 33, 34], the algorithm research of perching [35, 36], the system development of perching [37, 38, 39, 40, 41, 42, 43, 44, 45], the control method of perching [46, 47, 48, 49, 50, 51, 52], and especially, the development of the mechanical structure of perching devices. In the design of a mechanical structure, various types of mechanical structures have been developed. This includes grippers [53, 54, 55, 56], claws [57, 58] or hands [59, 60], perching foot [61, 62] and other mechanisms. However, comparing with these previous studies in perching mechanism, an unactuated parallel-link gripper is suitable for achieving perching on a planar object. It has a purely mechanical structure; therefore, it does not consume any additional electrical energy. In particular, under the action of the parallel-link mechanism and the principle of leverage, the entire device, including the gripper and multicopter body, can always maintain a horizontal posture while perching, which can be a necessary feature for the subsequent takeoff of the multicopter.

Similar to the researches on perching, countless researchers are also committed to the research of multicopter landing. Compared with the research on mechanism design in the field of perching, there seems to be more research on system development, algorithm [63, 64, 65, 66] and simulation [67, 68, 69, 70] in the field of multicopter landing. In the aspect of system development in field of multicopter landing, many researchers have developed new systems for different landing conditions. For example, several researchers developed visual navigation [71, 72, 73, 74] or vision aided [75, 76] systems for multicopter landing, and other researchers, focused on the development of polarimetric system [77], monitoring system [78], and airborne wind energy system [79], etc [80, 81, 82, 83]. Although many researchers have focused on the research of system and control for multicopter landing, it does not mean that the research on the mechanical structure of landing is not important. Many researchers still focus on the research on the relevant mechanical structure of multicopter landing. Researchers from Xiamen University and Korea Advanced Institute of Science and Technology have developed twin-rotor mechanism for multicopter landing [84, 85], and in addition, a number of researcher developed safeguarded landing mechanism [86] and other effective mechanisms [87]. However, beside

the aforementioned previous studies, landing on a rough terrain is another problem it may face during missions. Under such situations, the parallel-link gripper utilized for planar perching has difficulty performing its function. To cope with this problem, I developed a passive skid that facilitates the landing of multicopters on a rough terrain or uneven ground. However, most of the previous studies have focused on electrical skids. Therefore, based on the robot arm attached multicopter, the idea of substituting an underactuated skid with an electrical skid for landing on a rough terrain is performed. The combined structure of the robot arm and underactuated skid can maximize the functionality of the multicopter. While the multicopter retains its catching or grasping function through the robot arm, it can also achieve smooth landing on uneven ground.

As the initial step, the mechanical structure of the underactuated skid was proposed, and the entire device can be considered a three-legged mechanism consisting of a passive joint and two feet. Then the non-tilting condition of the entire device was analyzed, and a judgment method was proposed to determine the possibility of landing on a rough terrain. To simplify the complex environment, I simulated a rough terrain with slopes with different inclination angles. By analyzing the positional relationship between the contact point and the inclined plane, and the contact points and the center of gravity, the possibility of landing the multicopter on different inclined planes can be concluded. According to the analysis and conclusion, the judgment regarding whether smooth landing can be successfully achieved is also feasible.

## **1.1 Background**

### **1.1.1 Concept of perching and landing**

Perching, for its meaning in the Cambridge English Dictionary [88], implies that to be in a high position or in a position near the edge of something, or to put something in this position; and Landing, used to describe the motion that arriving on the ground or other surface after moving down through the air [89]. Compared with perching, landing seems to have a wider range of applications, because no multicopters can stay in the sky without landing after all, no matter the landing site is on ground or on water. However,

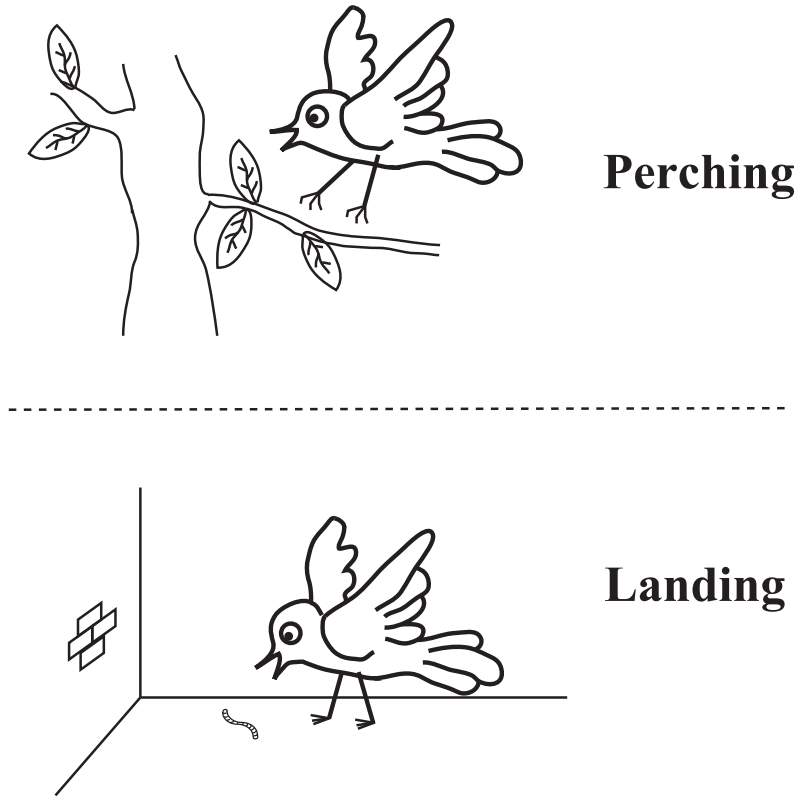


**Figure 1.1: Concept of perching and landing.**

this does not mean that perching is less important than landing. We can take birds as an example. Most of the time, birds prefer to perch on objects with a certain height, such as branches, telegraph poles or chimneys. In addition to foraging, birds rarely land on the ground. This is not only because there are more predators on the ground, but also because the field of vision is wider and safer for birds. Although in human society, multicopters are different from birds and do not have to worry about predators on the ground, there is no doubt that the field of vision in high places is wider than the ground. This advantage is the fundamental reason for the existence of perching, and it is also the significance of our research on perching for multicopters. On the other hand, as mentioned above, landing as an essential behavior for multicopters, plays an important role when multicopters conducting tasks. However, most of the previous studies concentrated on plane landing and we think that it may case some limitations. Thus, in our research, the new device is proposed to make the multicopter land on a rough terrain.

### 1.1.2 Device for a multicopter capable of perching

Recently, there has been an increase in the use of multicopters for rescue and transportation[90], and environmental monitoring [91, 92], and for express home delivery, whereby a robot arm is attached to the multicopter[93]. Express delivery using a multicopter, in response to people's consumption requirements, has several advantages [94, 95]. Therefore, many researchers have focused on the evaluation of multicopter application field [96, 97], and additionally, studies need to be conducted on multicopters equipped with a mechanism for catching, and more importantly, perching.

The word *perching* was originally used to describe bird landing behavior. Extended to multicopter behavior, the term indicates a process in which the multicopter flies to land or sit on targets, such as pipes, sticks, or branches. However, the multicopter requires a certain mechanical device to execute the maneuver for perching on targets. The design of the device depends on the shape and properties of the target. For example, for the multicopter to perch on a branch or cylindrical target, the gripper must be designed with birdlike talons; to perch on horizontal and vertical platforms, the gripper must be designed so that it can grasp the target firmly, without sliding down. In general, studies on perching can be divided into two categories: those on the control of perching and those on the mechanical structure of perching. In a previous study on perching control, researchers from New Mexico State University and Shanghai University developed bio-inspired trajectory generation for unmanned aerial vehicle (UAV) perching based on the tau theory[98, 99]. A number of other researchers have focused on the mechanical structures of perching. These mechanical structures include grippers[100, 101, 102, 103], robot hands[104, 105], landing legs[106, 107], and other advanced mechanisms [108, 109, 110, 111] for grasping and perching. For example, researchers at the University of Twente and Aalborg University developed a mechanism that facilitates the reliable perching of UAVs on smooth vertical surfaces using a lightweight passive vacuum-cup technology and the absorption of aerial impacts[112].

However, the aforementioned mechanical structures for perching are actuated because they carry power supply devices. This increases the mass of the entire aerial sys-



**Figure 1.2: Multicopter with simple underactuated device can perch on veranda easily for delivery, security monitoring, etc.**

tem, which may result in an overload of the multicopter when flying or perching. Thus, studies on perching via passive mechanisms have been conducted to solve this problem. Researchers at the University of Utah developed an avian-inspired passive mechanism for quadrotor perching[113, 114]. In this study, the proposed passive mechanism is capable of perching on a pipe-like object. Although this avian-inspired device can perch on a cylindrical object, it is composed of numerous complex mechanical structures. For the purpose of delivery or security monitoring, the target of perching often involves a man-made object, such as a planar structure, which only needs a simpler mechanism. Therefore, to achieve this purpose, we proposed an underactuated device with a simpler mechanical structure, which is shown in Figure 1.

We successfully developed this underactuated parallel-link gripper in an earlier study[115]; however, there was an insufficient discussion on perching. For example, to simplify the calculation, we assumed that the contact point of the upper side of the gripper was at the innermost position. However, in the real world, we must consider cases where

the contact point of the gripper is at an arbitrary position, which is one of the focus areas of this study.

### 1.1.3 Device for multicopter capable of rough terrain landing

Owing to the outstanding advantages such as light weight and low cost, multicopters are now utilized frequently in fields. Although people are enjoying the innumerable conveniences that multicopters provide, more researchers are beginning to realize the importance of landing condition to the multicopter. Suitable landing conditions can be important, especially in several fields, such as inspection and express delivery, otherwise the multicopter may crash, and cause mission failure. As an essential part of landing, the condition of the landing site is also critical, among other factors. Generally, for multicopters, a flat ground is the best condition for landing when conducting missions. However, landing on flat ground is only in ideal situations. In an environment where severe disasters, such as earthquakes, mudslides, or tsunamis have occurred, the terrain becomes irregular, and even contains numerous obstacles such as rocks or broken debris. In these cases, a multicopter that can land on uneven ground or rough terrain is required.

Generally, research on uneven ground mobile robots, including multicopters, can be divided into three categories: research on control system, research on obstacle avoidance, and research on mechanism design for perching or landing on uneven ground. To control robots moving on uneven ground, researchers from Easwari Engineering College monitored the landing mechanism of the multicopter, by using gyroscope and accelerometer[116], and researchers from The University of Tokyo proposed a vision-based autonomous landing system for a fixed wing multicopter[117]. In contrast, lots of researchers have focused on the development of a control system for multicopters, to achieve a better result, not solely for landing, but also for action synchronization of the mechanism[118, 119, 120, 121]. For uneven ground or rough terrains, a number of researchers have focused on obstacle avoidance mechanism, such as stair-climbing robots[122, 123, 124, 125, 126], wall-climbing devices[127], and even mobile robots with semicircular wheels[128]. Considering that solely moving on uneven ground is inadequate, more researchers are begin-

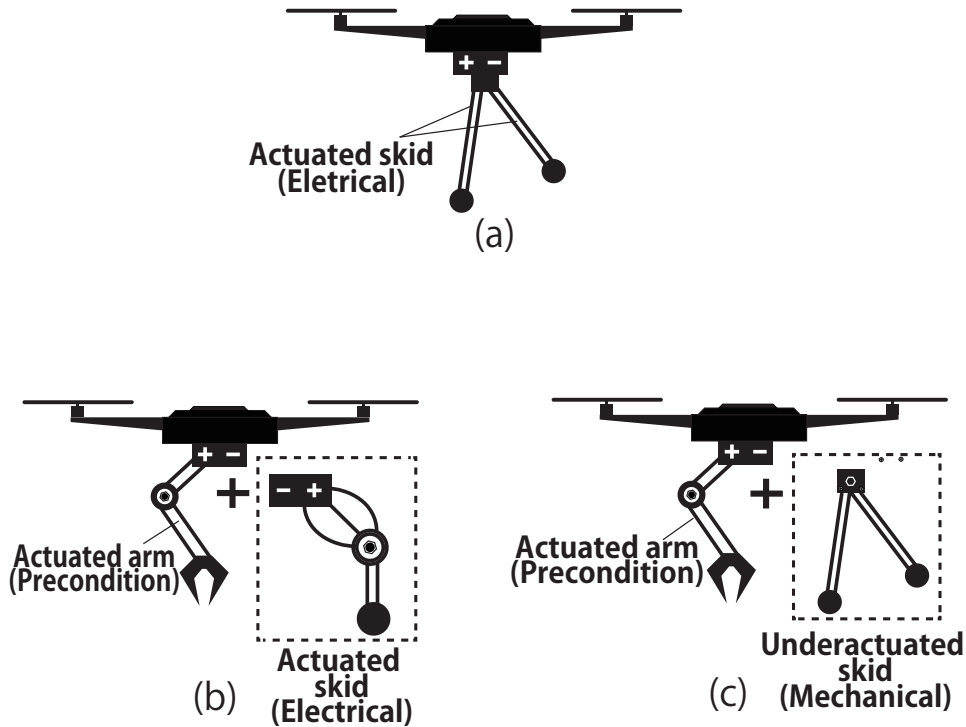


**Figure 1.3:** (a). Normal multicopters utilize electrical skid for landing or perching; (b). Although, when a multicopter carried with an electrical arm and skid can achieve both catching (or grasping) and landing, it consumes much more energy, and loading batteries also increases the weight of the entire device; (c). Based on the arm-attached multicopter, the idea of substituting an underactuated skid with an electrical skid for landing on rough terrain is performed.

ning to focus on the mechanical structure that can make the unmanned aerial vehicle (UAV) land steady.

Landing refers to a series of processes from the moving state of the flying object in the air, to contact with the ground, and then to the static state, rather than constant motion. Thus, studies on the development of the mechanism for landing or perching may have greater reference significance. Previously, I developed a parallel-link-passive gripper for multicopters perching on plane-like targets by its own gravity, and researchers from University of Utah developed an avian-inspired passive mechanism for quadrotor perching. However, for some special occasions such as events succeeding a natural disaster, a multicopter is unable to find a plane or pipe-like object for perching or landing. Thus, the research on enabling multicopters to land on uneven ground or rough terrain is consid-

ered. A few researchers developed novel multicopters which can land on water[129] or even asteroid ground[130].

However, the aforementioned devices for landing utilize electrical power. These actuated landing devices need to be carried with power supply devices, such as power source or several batteries, and this increases the mass of the entire system, which may result in the multicopter overload. As illustrated in Figure 1(a), most of the previous researches regard landing as its only achievable function, which may limit the diversity of multicopter functions. Therefore, to make the multicopter not only land smoothly on a rough terrain, but also realize functions such as grasping, we proposed the device which is illustrated in Figure 1.3(c)[131]. In previous studies[131], although the structure of the landing device was proposed, for the proposed skid, we did not indicate how to determine whether it can land on a rough terrain or not. Therefore, in this study, we describe the judgment method of its landing possibility. In addition, considering the posture of the arm, the range of the uneven ground which can be landed is presented.

## 1.2 Outline of thesis

This thesis is organized as 5 chapters including this introduction chapter.

In Chapter 2, the development of an underactuated parallel-link gripper for multicopter plane perching is described. Besides, the conditions and range of available perching is summarized by both theoretical analysis and experiment.

In Chapter 3, the development of a passive skid for multicopter landing on rough terrain is introduced. Not only the landing process of the proposed device is explained, but also, the analysis of the static model is described, and the theory is verified by several experiments.

Chapter 4 described the expanded research based on Chapter 3 and proposed the analysis of the multicopter carrying with passive skid for rough terrain landing. In this chapter, the influence of different postures of robot arm on the possibility of multicopter rough terrain landing, is concentrated. By simulating rough terrain with slopes with different inclination angles, the correctness of the theory and analysis is demonstrated.

Chapter 5 is the final chapter, and it concludes the contribution of my study, and the future work is also described in Chapter 5.

## **Chapter 2**

# **Development of an underactuated parallel-link gripper for multicopter plane perching**

The need for a perching robot is increasing in the field of rescue and transportation, and the research on perching an object by attaching a robot arm to the perching robot has been conducted. However, almost all the studies related to perching have been conducted using an actuated or electric device. However, perching by using an electric device has several disadvantages such as additional power consumption and an increase in the mass of the multicopter used to load an electric source. Instead of using an electric device, perching by using an underactuated gripper can effectively avoid these disadvantages. and this idea inspired us to develop an underactuated passive gripper, which has the advantage of not consuming electric power for perching.

In this chapter, we proposed a underactuated passive gripper for plane perching. However, only mechanism development is not enough: a method to confirm the available range for stable perching is one of the problems of using an underactuated passive gripper. Therefore, in this chapter, we also analyze a multicopter carried with an underactuated parallel link passive gripper for available plane perching. To enable perching on planes having different thicknesses and that are embedded at different depths, we summarize the available perching range and limitations based on friction cone theory. Our conclusion is supported by both theoretical and experimental results.

## 2.1 Underactuated parallel-link gripper prototype (multicopter included)

In this section, the prototype, especially the mechanism and structure for each part of the proposed perching device is described. The following is a description of the centering device mass, including the mechanism integration of parts and structure.

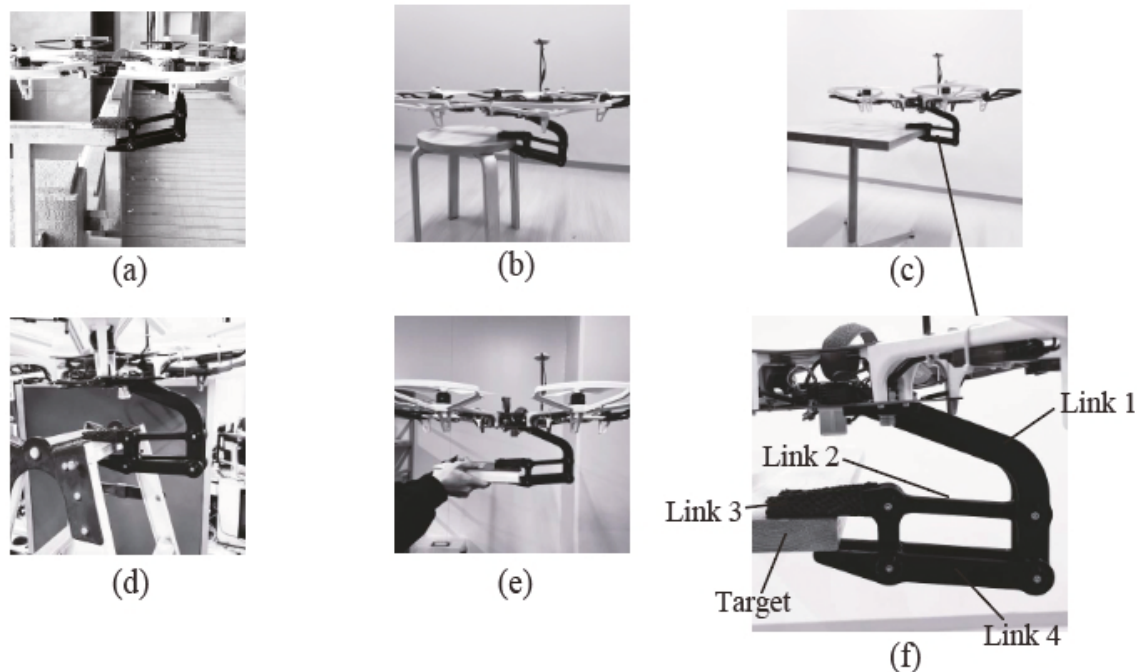


**Figure 2.1: Multicopter carried with the proposed device successful perches on several objects: (a) handrail. (b) chair. (c) desk. (d) ladder. (e) a book held by a person. (f) is the prototype of the proposed device.**

A prototype of the proposed perching device is shown in Figure 2.1. The entire device comprises two parts, a multicopter body and a perching gripper. For the multicopter body, we chose the DJI FlameWheel 550 type [132] as the carrier of our perching device. This type of multicopter has a diagonal wheelbase that is approximately 550 mm. It is a multi-rotor UAV that can achieve hovering, cruising, rolling, and other flight elements. Thus we were able to perform the perching experiment using this type of multicopter. The frame weighed 478 g; the takeoff weight was approximately 1200-2400 g, which we subsequently utilized in calculating the COG of the entire device. A 3S LiPo battery was used

as the power source for the multicopter when hovering. Based on previous experimental findings, the hovering time for the DJI FlameWheel 550 with a full 3S LiPo battery can be maintained for approximately 10-12 min.

## 2.2 Motion of perching on plane

Perching system can be divided into four parts, as shown in the left of Figure 2.2. Link 1 is the assembling bar that connects the body of the multicopter and other parts of the gripper. Link 2, which is in the middle, is called the connecting bar, and its function is to connect the gripper and assembling bar. Link 3 is the gripper, and it plays a role in grasping the upper side of the table. Link 4, which is the part beneath the table, is called the underside link bar, and it contacts the table and provides the grasping force for perching. Link 1 to 4 are composed of parallel devices, and as shown in the left of Figure 2.2, the distance between each joint was assumed to be  $l_1$ ,  $l_2$ ,  $l_3$  and  $l_4$ . Then, we can obtain the relationships  $l_1=l_3$  and  $l_2=l_4$ .

Figures 2.2(a), (b), and (c) describe the process of the perching motion, which consists of three stages. The first stage, shown in Figure 2.2(a), has to do with when the multicopter is approaching. When it is set to land on the target and maintain a horizontal posture to perch on the target smoothly. Then, in the second stage of perching, the underside of Link 3 contacts the upper side of the target surface, as shown in Figure 2.2(b). At the same time, the motors of the multicopter stop running and the entire device will decline because of its own gravity, and the front side of Link 4 rise until it touches the underside of the target. In the entire process, the body of the multicopter is maintained in a horizontal state, parallel the target surface, so that the entire device will not be tilted and maintain its balance. (Figure 2.2(c)).

## 2.3 Available condition for stable perching

In a previous study we performed a preliminary analysis on a specific situation. In this case, the object to be perched on was a table with a constant thickness. In addition, for case of analysis and calculation, we assumed that the contact point  $P_6$  was in the in-

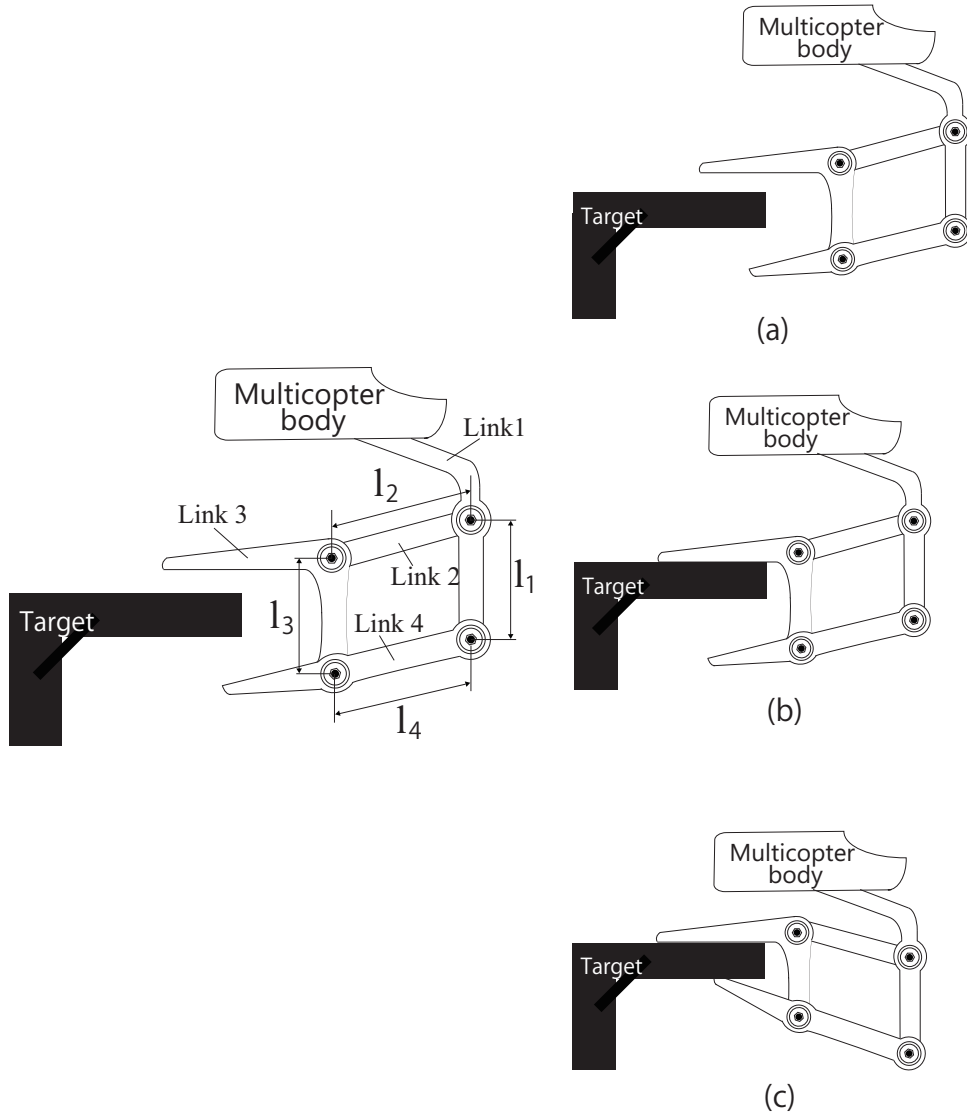


**Figure 2.2: Perching process of the underactuated parallel-link-passive gripper.**

nermost part of the gripper shown in Figure 2.3. This could be considered a very special case. However, in reality, it is necessary to extend the generalizability of the model by varying the condition. Thus, the main objective of this study is the analysis of perching success on a plane of varying thicknesses, embedded at an arbitrary depth (arbitrary contact point  $P_6$ ).

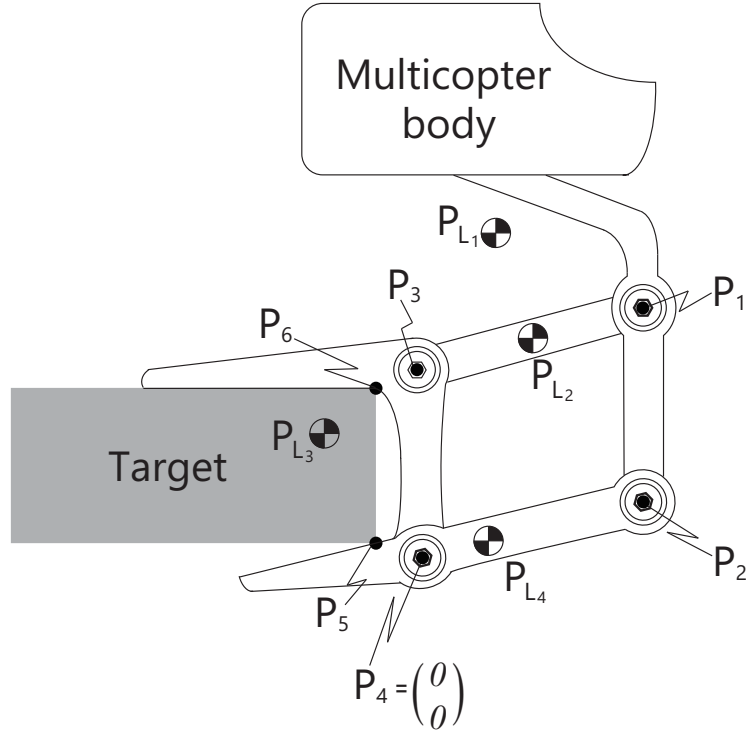


**Figure 2.3: Static model of the gripper device.**

### 2.3.1 Anatomy of the static model

In the entire system, as depicted in Figure 2.3, there are four parts and six positions in the static model of this device. Here, we assume that the gripper comes in contact with the target at points 5 and 6, which are indicated by  $P_5$  and  $P_6$ , respectively, as shown in Figure 2.3. Based on this assumption, a component analysis can be performed on the entire device. We assume that  $\mathbf{P}_i (i = 1, 2, \dots, 6)$  and  $\mathbf{F}_i (i = 1, 2, \dots, 6)$  are the position and force vectors, respectively.

We define  $\mathbf{F}_i = [F_{ix}, F_{iy}]^T$ ,  $\mathbf{P}_i = [P_{ix}, P_{iy}]^T$  and  $\mathbf{S}(\mathbf{P}_i) = [-P_{iy}, P_{ix}]$ . Subsequently, the torque  $\tau_i$  can be defined as follows:

$$\tau_i = P_{ix}f_{iy} - P_{iy}f_{ix} = \begin{bmatrix} -P_{iy} & P_{ix} \end{bmatrix} \begin{bmatrix} f_{ix} \\ f_{iy} \end{bmatrix} = \mathbf{S}(\mathbf{P}_i)\mathbf{F}_i. \quad (2.1)$$

Furthermore, we define  $\mathbf{F}_{L_i} (i = 1, 2, 3, 4)$  as the gravitational force of Link  $i$ , and  $\mathbf{P}_{L_i} (i = 1, 2, 3, 4)$  as the position of the gravitational force of Link  $i$ . Similar to Equation

(2.1), the torque  $\tau_{L_i}$  can be defined as:

$$\tau_{L_i} = \mathbf{S}(\mathbf{P}_{L_i})\mathbf{F}_{L_i}. \quad (2.2)$$

As mentioned above, the entire device can be divided into four parts. It is important to note that six forces are active during perching.  $\mathbf{F}_1$  to  $\mathbf{F}_4$  denote the forces at the joints and  $\mathbf{F}_5$  to  $\mathbf{F}_6$  denote the forces at the contact points. Each part of the device during the perching process is analyzed individually .

$$\mathbf{F}_1 + \mathbf{F}_2 + \mathbf{F}_{L_1} = \mathbf{0} \quad (2.3)$$

$$\tau_1 + \tau_2 + \tau_{L_1} = 0 \quad (2.4)$$

$$-\mathbf{F}_1 + \mathbf{F}_3 + \mathbf{F}_{L_2} = \mathbf{0} \quad (2.5)$$

$$-\tau_1 + \tau_3 + \tau_{L_2} = 0 \quad (2.6)$$

$$-\mathbf{F}_3 + \mathbf{F}_4 + \mathbf{F}_6 + \mathbf{F}_{L_3} = \mathbf{0} \quad (2.7)$$

$$-\tau_3 + \tau_4 + \tau_6 + \tau_{L_3} = 0 \quad (2.8)$$

$$-\mathbf{F}_2 - \mathbf{F}_4 + \mathbf{F}_5 + \mathbf{F}_{L_4} = \mathbf{0} \quad (2.9)$$

$$-\tau_2 - \tau_4 + \tau_5 + \tau_{L_4} = 0 \quad (2.10)$$

Here, we can combine Equations (2.1)-(2.10) into the formula  $\mathbf{A}\mathbf{x} = \mathbf{b}$ , where  $\mathbf{A} \in \mathfrak{R}^{12 \times 12}$ ,  $\mathbf{x} \in \mathfrak{R}^{12}$ , and  $\mathbf{b} \in \mathfrak{R}^{12}$ . Specifically,

$$\mathbf{A} = \begin{bmatrix} \mathbf{I} & \mathbf{I} & \mathbf{0} & \mathbf{0} & \mathbf{0} & \mathbf{0} \\ \mathbf{S}(\mathbf{P}_1) & \mathbf{S}(\mathbf{P}_2) & \mathbf{0} & \mathbf{0} & \mathbf{0} & \mathbf{0} \\ -\mathbf{I} & \mathbf{0} & \mathbf{I} & \mathbf{0} & \mathbf{0} & \mathbf{0} \\ -\mathbf{S}(\mathbf{P}_1) & \mathbf{0} & \mathbf{S}(\mathbf{P}_3) & \mathbf{0} & \mathbf{0} & \mathbf{0} \\ \mathbf{0} & \mathbf{0} & -\mathbf{I} & \mathbf{I} & \mathbf{0} & \mathbf{I} \\ \mathbf{0} & \mathbf{0} & -\mathbf{S}(\mathbf{P}_3) & \mathbf{S}(\mathbf{P}_4) & \mathbf{0} & \mathbf{S}(\mathbf{P}_6) \\ \mathbf{0} & -\mathbf{I} & \mathbf{0} & -\mathbf{I} & \mathbf{I} & \mathbf{0} \\ \mathbf{0} & -\mathbf{S}(\mathbf{P}_2) & \mathbf{0} & -\mathbf{S}(\mathbf{P}_4) & \mathbf{S}(\mathbf{P}_5) & \mathbf{0} \end{bmatrix}, \quad (2.11)$$

$$\mathbf{x} = \left[ \mathbf{F}_1^T, \mathbf{F}_2^T, \mathbf{F}_3^T, \mathbf{F}_4^T, \mathbf{F}_5^T, \mathbf{F}_6^T \right]^T \quad (2.12)$$

$$\mathbf{b} = - \left[ \mathbf{F}_{L_1}^T, \tau_{L_1}, \mathbf{F}_{L_2}^T, \tau_{L_2}, \mathbf{F}_{L_3}^T, \tau_{L_3}, \mathbf{F}_{L_4}^T, \tau_{L_4} \right]^T, \quad (2.13)$$

Therefore, the force  $\mathbf{x}$  can be obtained using the following equation:

$$\mathbf{x} = \mathbf{A}^{-1} \mathbf{b}. \quad (2.14)$$

### 2.3.2 Target thickness classification discussion

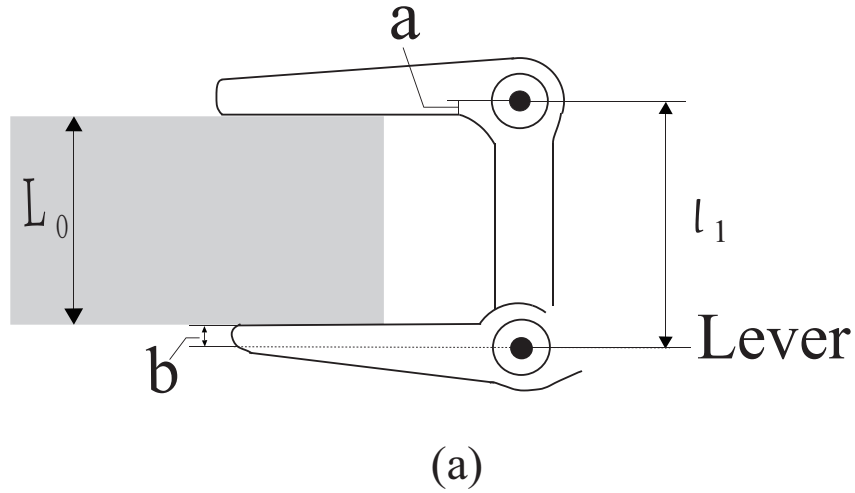


**Figure 2.4: Definition of  $L_0$ ,  $a$ , and  $b$ .**

As shown in Figure 2.4, we assume that the ordinate distance between the lower surface of the gripper and  $\mathbf{P}_3$  as  $a$  and the ordinates distant between the upper surface of gripper and  $\mathbf{P}_4$  is  $b$ . Then, when the lower surface of Link 3 and the upper surface of Link 4 are parallel, we assume that the target thickness  $L$  is  $L_0$ , which can be obtained as follows:

$$L_0 = l_1 - a - b. \quad (2.15)$$

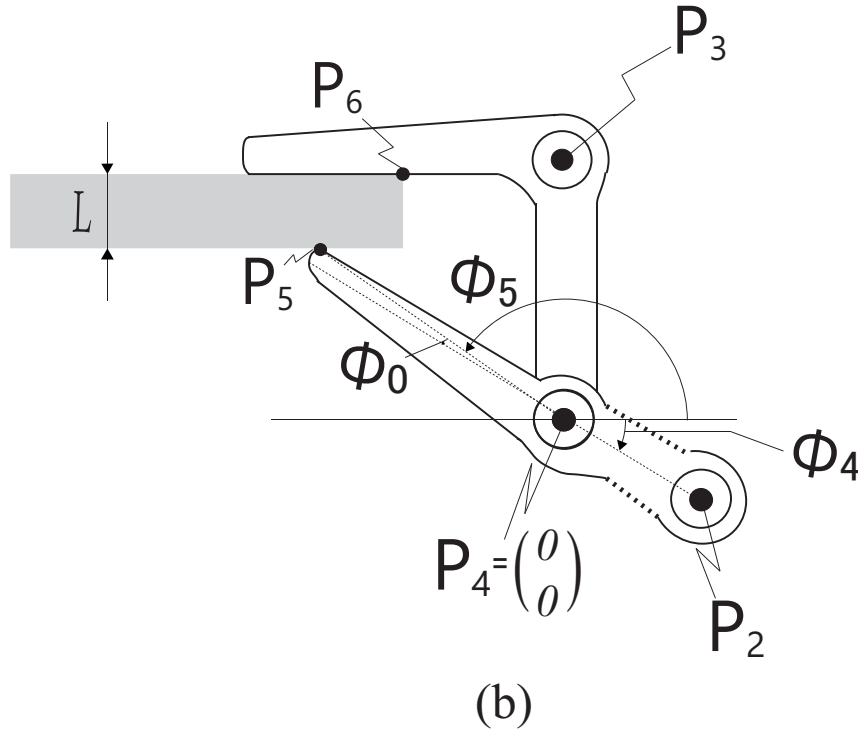


**Figure 2.5:** Situation analysis of  $L \leq L_0$ .

As can be observed from Figure 2.5 and Figure 2.6, that in the cases of  $L \leq L_0$  and  $L > L_0$ , the representations of the position vector  $\mathbf{P}_5$  are different. Thus, it is necessary to classify both situations separately. Specifically, during the analysis of the perching state, we assume that the gripper of Link 3 maintains a fixed position, and set  $\mathbf{P}_4$  as the origin. Then, we can obtain the vector coordinates as follows:

$$\mathbf{P}_3 = \begin{bmatrix} P_{3x} \\ P_{3y} \end{bmatrix} = \begin{bmatrix} 0 \\ l_1 \end{bmatrix}. \quad (2.16)$$

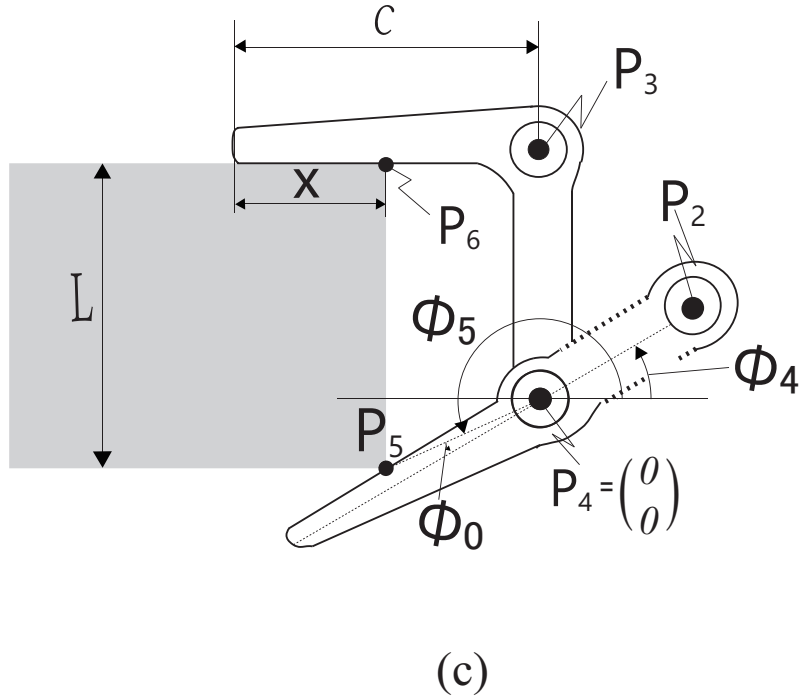


**Figure 2.6: Situation analysis of  $L > L_0$ .**

$$\mathbf{P}_4 = \begin{bmatrix} P_{4x} \\ P_{4y} \end{bmatrix} = \begin{bmatrix} 0 \\ 0 \end{bmatrix}. \quad (2.17)$$

The position vector  $\mathbf{P}_5$  is at the farthest end of Link 4. As shown in Figure 2.5 and Figure 2.6,  $\phi_5$  is the angle between the lever and the line  $\mathbf{P}_4\mathbf{P}_5$ , which can be expressed as a two-variable formula:

$$\phi_5 = A \tan 2(P_{5y}, P_{5x}). \quad (2.18)$$

Then, as shown in Figure 2.5 and Figure 2.6, we assume that  $\phi_0$  is the angle between the line  $\mathbf{P}_2\mathbf{P}_4$  and the line  $\mathbf{P}_4\mathbf{P}_5$ , which can be obtained as follows:

$$\phi_0 = \sin^{-1}\left(\frac{b}{|\mathbf{P}_4 - \mathbf{P}_5|}\right). \quad (2.19)$$

We assume that  $\phi_4$  is the angle between the lever and the central axis of Link 4, which can be obtained as follows:

$$\phi_4 = (\phi_5 + \phi_0) - 180^\circ. \quad (2.20)$$

Thus, the position vectors of  $\mathbf{P}_1$  and  $\mathbf{P}_2$  can be obtained as follows:

$$\mathbf{P}_2 = \begin{bmatrix} P_{2x} \\ P_{2y} \end{bmatrix} = \begin{bmatrix} l_4 \cos \phi_4 \\ l_4 \sin \phi_4 \end{bmatrix}. \quad (2.21)$$

$$\mathbf{P}_1 = \begin{bmatrix} P_{1x} \\ P_{1y} \end{bmatrix} = \begin{bmatrix} P_{2x} \\ P_{2y} \end{bmatrix} + \begin{bmatrix} 0 \\ l_1 \end{bmatrix}. \quad (2.22)$$

**(a) When thickness  $L \leq L_0$**

A situation analysis of the target thickness  $L \leq L_0$  is shown in Figure 2.5. In the range of  $0 < L \leq L_0$ , an increase in the thickness  $L$  will cause the changing of each position vector. We define the distance between  $\mathbf{P}_4$  and  $\mathbf{P}_5$  as  $l_s$ . Then,  $\mathbf{P}_5$  can be obtained as follows:

$$\mathbf{P}_5 = \begin{bmatrix} P_{5x} \\ P_{5y} \end{bmatrix} = \begin{bmatrix} -l_s \cos \phi_5 \\ l_1 - a - L \end{bmatrix}. \quad (2.23)$$

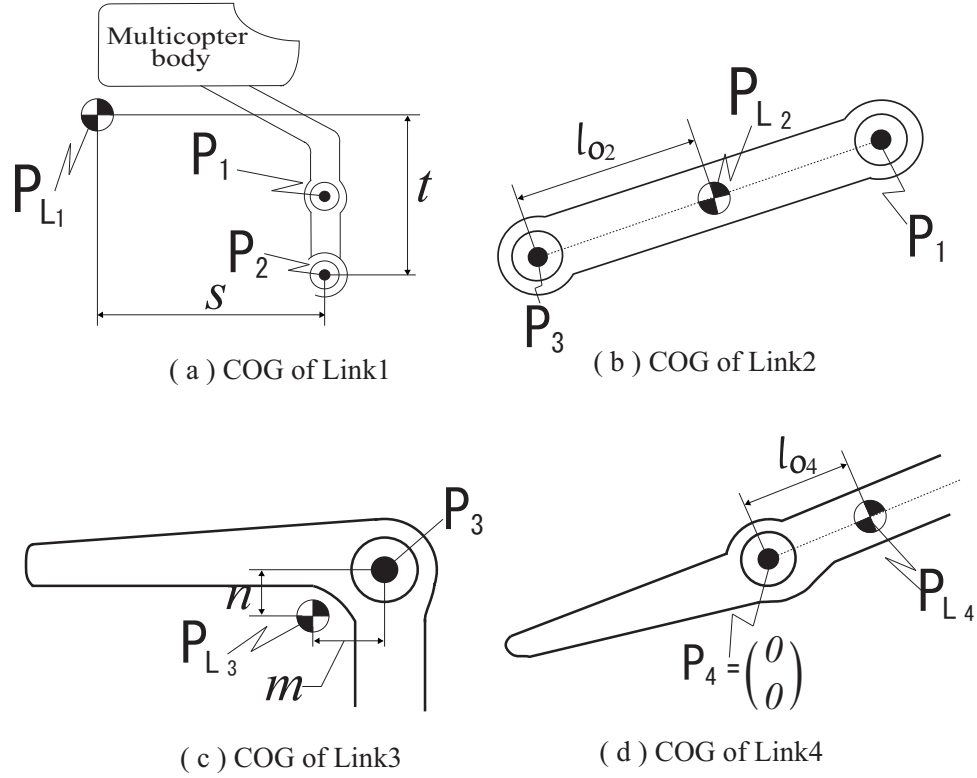


**Figure 2.7: Schematic diagram of center of gravity (COG) of Link 1, Link2, Link3 and Link4.**

(b).When thickness  $L > L_0$

As shown in Figure 2.6, in the cases where  $L > L_0$  the contact point  $P_5$  is no longer the leftmost point; thus, not only the thickness  $L$  but the embedded depth  $x$  will also have an influence on the coordinates of other position vectors. Here, we assume that  $c$  is the horizontal distance between  $P_3$  and the tip of the upper side of Link 3. The coordinates of the position vector  $P_5$  can be obtained as follows:

$$\mathbf{P}_5 = \begin{bmatrix} P_{5x} \\ P_{5y} \end{bmatrix} = \begin{bmatrix} x - c \\ l_1 - a - L \end{bmatrix}. \quad (2.24)$$

### 2.3.3 Determination of the COG of each link

The center of gravity (COG) of each link is presented Figure 2.7. As shown in Figure 2.7(a), Link 1 is based on  $P_2$ ; it is offset by two parameters, namely  $s$  and  $t$ , in horizontal and vertical directions, respectively. Thus, the COG of Link 1 can be obtained as follows:

$$\mathbf{P}_{L_1} = \begin{bmatrix} P_{L_1x} \\ P_{L_1y} \end{bmatrix} = \begin{bmatrix} P_{2x} + s \\ P_{2y} + t \end{bmatrix}. \quad (2.25)$$

Figure 2.7(b) shows that Link 2 rotates based on  $P_3$ , and because of it can be deduced that its COG is in the middle of the line  $P_1P_3$ , and the distance between the COG and  $P_3$  is assumed to be  $l_{o2}$ . Then, the COG of Link 2 can be obtained as follows:

$$\mathbf{P}_{L_2} = \begin{bmatrix} P_{L_2x} \\ P_{L_2y} \end{bmatrix} = \begin{bmatrix} P_{3x} + l_{o2} \cos \phi_4 \\ P_{3y} + l_{o2} \sin \phi_4 \end{bmatrix}. \quad (2.26)$$

Figure 2.7(c) shows that Link 3 is based on  $P_3$  and is offset by two parameter, namely  $m$  and  $n$ , in the horizontal and vertical directions, respectively. Thus, its COG can be obtained as follows:

$$\mathbf{P}_{L_3} = \begin{bmatrix} P_{L_3x} \\ P_{L_3y} \end{bmatrix} = \begin{bmatrix} P_{3x} + m \\ P_{3y} + n \end{bmatrix}. \quad (2.27)$$

As can be observed from Figure 2.7(d), similar to Link 2, Link 4 is rotated based on  $P_4$  and the COG is considered to be on the central axis of Link 4. We assume that the distance between the COG of Link 4 and  $P_4$  is  $l_{o4}$ ; the COG of Link 4 can be obtained as follows:

$$\mathbf{P}_{L_4} = \begin{bmatrix} P_{L_4x} \\ P_{L_4y} \end{bmatrix} = \begin{bmatrix} P_{4x} + l_{o4} \cos \phi_4 \\ P_{4y} + l_{o4} \sin \phi_4 \end{bmatrix}. \quad (2.28)$$

Specifically, the COG of the entire device is calculated by obtaining the COG of each part:

$$\mathbf{P}_{all} = \begin{bmatrix} P_{allx} \\ P_{ally} \end{bmatrix} = \begin{bmatrix} \frac{\sum_{i=1}^4 m_i P_{L_ix}}{\sum_{i=1}^4 m_i} \\ \frac{\sum_{i=1}^4 m_i P_{L_iy}}{\sum_{i=1}^4 m_i} \end{bmatrix}. \quad (2.29)$$

### 2.3.4 Classification discussion of the location of the COG

In the previous subsection, we discussed the effect of the target factor on the perching state. Here, we will conduct a classification discussion on the impact of the location of the COG on the perching situation. As shown in Figure 2.8, when the COG of the entire device changes, the location of  $\mathbf{P}_6$  is changed. Thus, when analyzing the impact of the COG, the difference in the horizontal position is key, and the position where the arm is implemented depends on the parameter  $s$ . Compared with the other parameters,  $s$  is the most significant. Therefore, we assume that  $s$  is a variable, where as  $t$  is constant. Consequently, the change in  $s$  would change the COG of the entire device  $\mathbf{P}_{allx}$ .

#### (a) COG is to the right of the rightmost border.

As shown in Figure 2.8(a), with the change in the variable  $s$ , the COG of the entire device is to the right of the rightmost border, and we assume that the contact point of the target and lower surface of Link 3 and  $\mathbf{P}_6$  is located at the edge of the target. Therefore, in this case, the vector of  $\mathbf{P}_6$  can be obtained as follows:

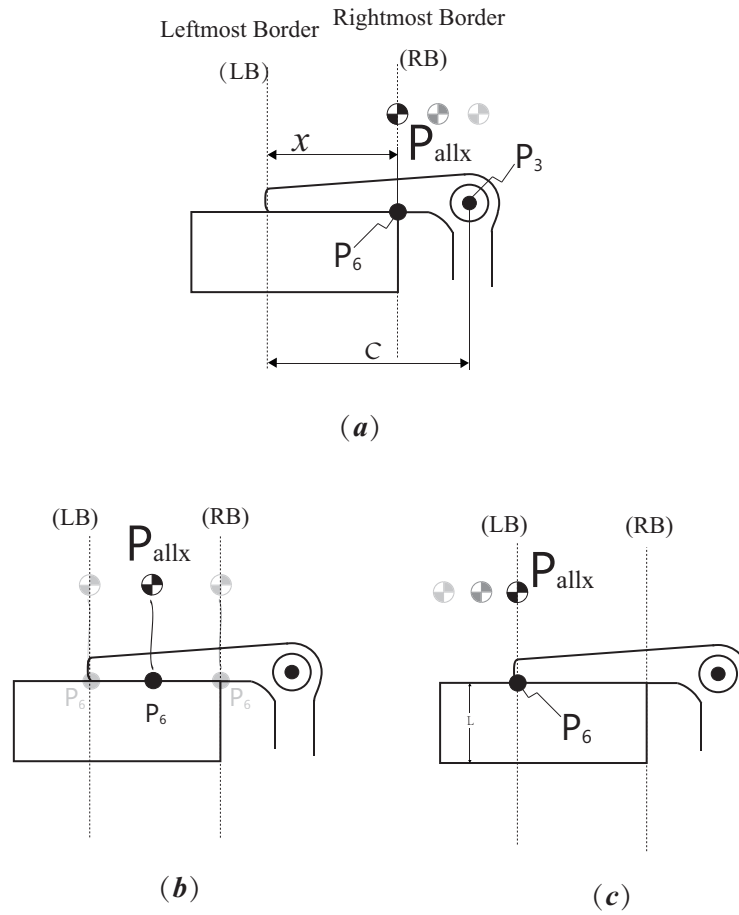


**Figure 2.8: Factor of the Position of the COG.**

$$\mathbf{P}_6 = \begin{bmatrix} P_{6x} \\ P_{6y} \end{bmatrix} = \begin{bmatrix} x - c \\ l_1 - a \end{bmatrix}. \quad (2.30)$$

**(b) COG is between two sides of the border**

As shown in Figure 2.8(b), when the COG of the whole device is between both sides of the border, we assume that the contact point of the target and the lower surface of Link 3 and  $\mathbf{P}_6$  has the same horizontal coordinate. Therefore, in this case, the vector of  $\mathbf{P}_6$  can be obtained as follows:

$$\mathbf{P}_6 = \begin{bmatrix} P_{6x} \\ P_{6y} \end{bmatrix} = \begin{bmatrix} P_{allx} \\ l_1 - a \end{bmatrix}. \quad (2.31)$$

**(c) COG is to the left of the leftmost border**

As shown in Figure 2.8(c), when the COG of the entire device is to the left of the leftmost border, we assume that the contact point of the target and the lower surface of Link 3 and  $\mathbf{P}_6$  is at the edge of the gripper. Therefore, in this case, the vector of  $\mathbf{P}_6$  can be obtained as follows:

$$\mathbf{P}_6 = \begin{bmatrix} P_{6x} \\ P_{6y} \end{bmatrix} = \begin{bmatrix} -c \\ l_1 - a \end{bmatrix}. \quad (2.32)$$

### 2.3.5 Categorize and integrate various situations

In the previous section, we separately analyzed the different factors that influence perching. However, in reality, several of these factors can occur simultaneously. In this case, we need to classify and integrate various situations as shown in Figure 2.9.

**(Case1)  $L \leq L_0$ , and COG is to the right of the rightmost border**

As shown in Figure 2.9(a), for the situation that when target thickness  $L \leq L_0$  and the COG of the whole device is to the right of the Rightmost border, we define that this case as *Case1*.

**(Case2)  $L > L_0$ , and COG is to the right of the rightmost border**

As shown in Figure 2.9(b), for the situation that when target thickness larger than  $L_0$  and the COG of the whole device is also to the right of the Rightmost border, we define that this case as *Case2*.

**(Case3)  $L \leq L_0$ , and COG between the two sides of the border**

As shown in Figure 2.9(c), for the situation that when target thickness  $L \leq L_0$  and the COG of the whole device is between the two sides of the border, we define that this case as *Case3*.

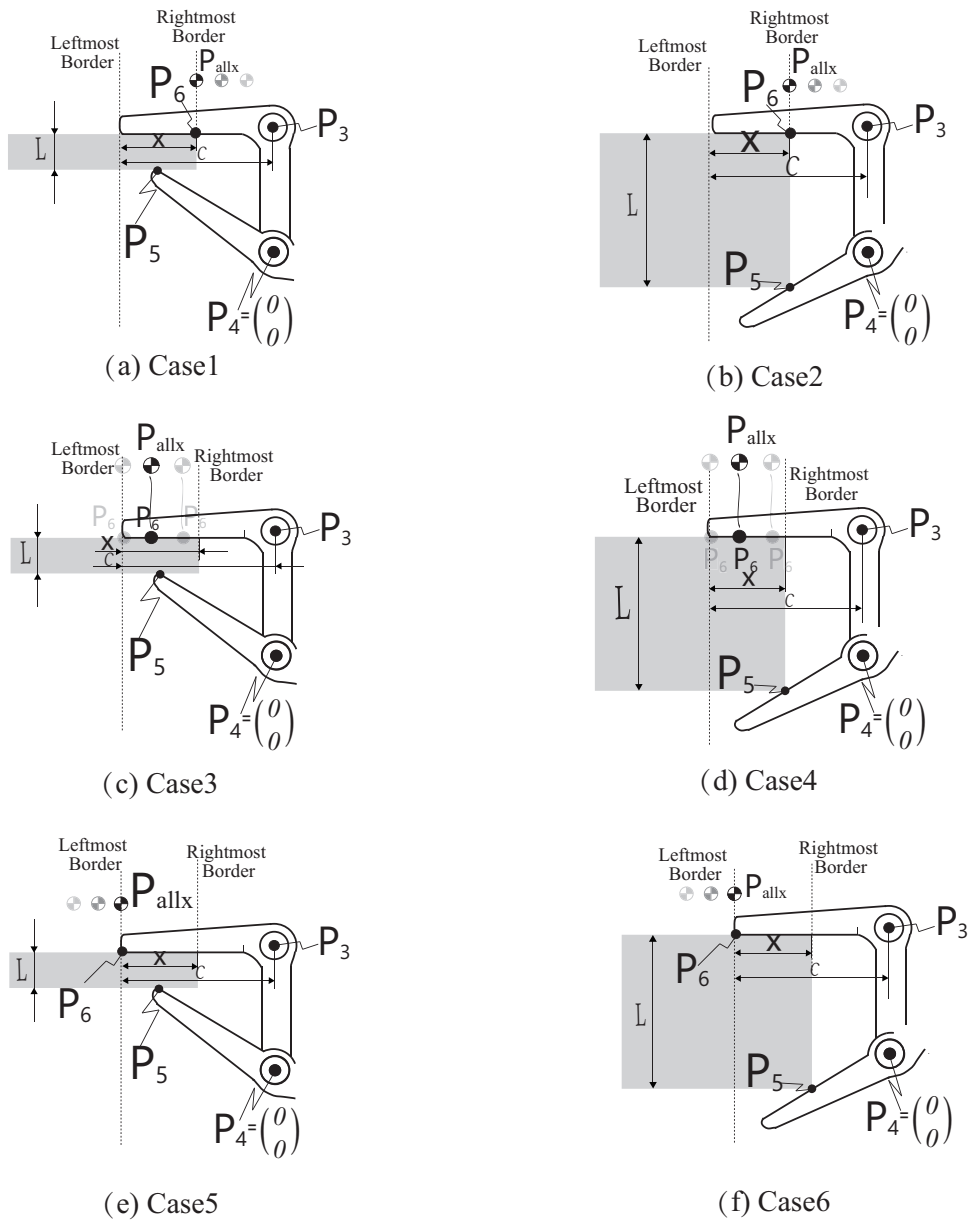


**Figure 2.9: Categorize and integrate various situations.**

**(Case4)  $L > L_0$ , and COG between the two sides of the border**

As shown in Figure 2.9(d), for the situation that when target thickness larger than  $L_0$  and the COG of the whole device is between the two sides of the border, we define that this case as *Case4*.

**(Case5)  $L \leq L_0$ , and COG is to the left of the leftmost border**

As shown in Figure 2.9(e), for the situation that when target thickness  $L \leq L_0$  and the COG of the whole device is to the left of the Leftmost border, we define that this case as *Case5*

**(Case6)  $L > L_0$ , and COG is to the left of the leftmost border**

As shown in Figure 2.9(f), for the situation that when target thickness larger than  $L_0$  and the COG of the whole device is to the left of the Leftmost border, we define that this case as *Case6*

All the situations are analyzed and the properties of items are established. Subsequently, the forces required for perching in a certain condition can be determined using Eq.(14). Based on these forces, the perching state can be assessed.

## 2.4 Perching state judgment

In Section 2.3, we analyzed of each situation related to perching. In this section, the process of judging the perching state is described; we conclude that there is an optimal range for available perching in different situations.

### 2.4.1 The friction cone theory

As shown in Figure 2.10(a), the gripper finger contacts the target table at Point  $P$ , the starting point of the force. Then, we decompose the force in the horizontal and vertical directions. We assume that the horizontal component is  $F$  and the vertical component is

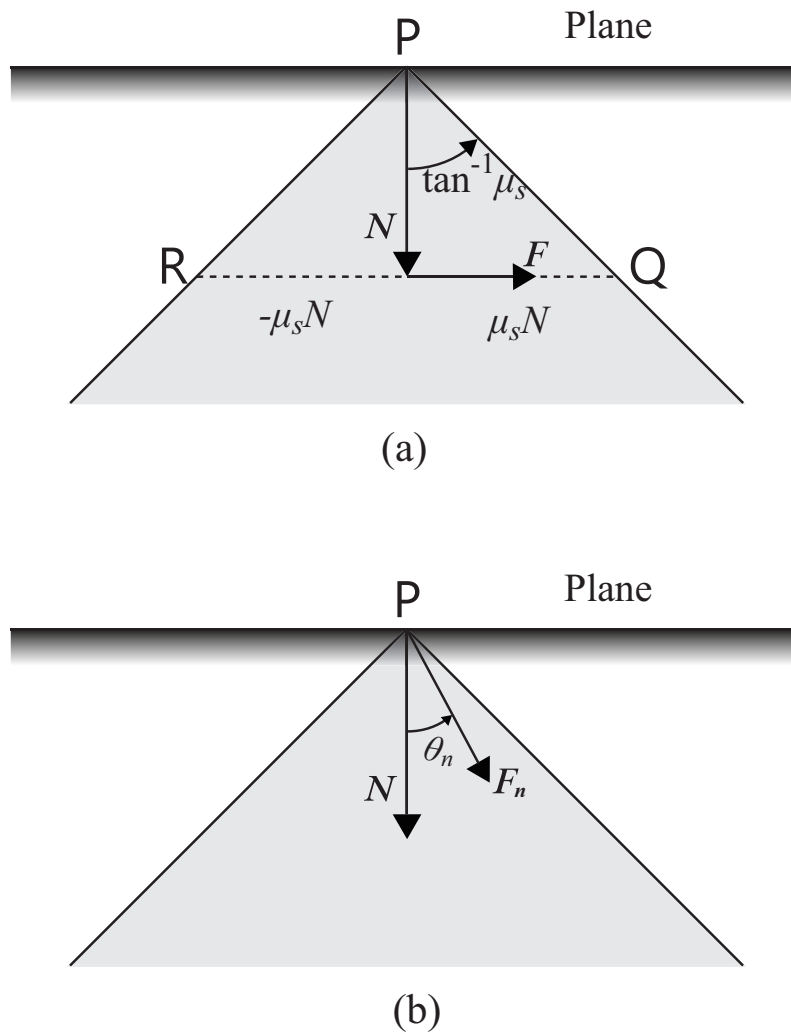


**Figure 2.10: Concept of the friction cone.**

the normal vector  $N$ . We assume that the coefficient of friction is  $\mu_s$ ; thus, the maximum static friction force can be  $\mu_s N$  or  $-\mu_s N$ . When  $F$  is equal to  $\mu_s N$ , we assume that the end point of the force is Point  $Q$ . When  $F$  is equal to  $-\mu_s N$ , we consider the end point of the force as Point  $P$ . Then we obtain two lines,  $PQ$  and  $PR$ . Here, the angle between the normal vector and  $PQ$  can be obtained as  $\tan^{-1} \mu_s$ . (The angle between the normal vector and  $PR$  is  $\tan^{-1}(-\mu_s)$ ). We define the area inside the line  $PQ$  and  $PR$  as the "friction cone".

However, if the end point of the force (Point  $R$  or  $Q$ ) is inside the friction cone, the value of  $F$  will be smaller than the maximum static friction force. Otherwise, the value of  $F$  will be larger than the maximum static friction force. Therefore, if we describe the

force, starting from  $P$  as a vector, and the end point of the vector is inside the friction cone, the gripper finger will be able to grasp the target. However, if the end point of the vector is outside the friction cone, the gripper finger will be unable to grasp the target and the perching state cannot be maintained.

### 2.4.2 Judgment based on friction cone theory

As shown in Figure 2.10(b), if there is an external force  $F_n$  and it forms an angle  $\theta_n$  with the normal vector  $N$ , the necessary condition achieve grasping is that  $\theta_n$  is smaller than  $\tan^{-1}(-\mu_s)$ . Specifically, in our study, we assume that the angle between the grasping force and normal vector, which starts at  $P_5$ , is  $\theta_5$ , and the frictional coefficient is assumed to be  $\theta_{\mu 5}$ . Similarly, we assume that the angle between the grasping force and normal vector, which starts at  $P_6$ , is  $\theta_6$ , and the frictional coefficient here is assumed as  $\theta_{\mu 6}$ . According to the friction cone theory, if the condition of the angle  $\theta_5 \leq \theta_{\mu 5}$  and  $\theta_6 \leq \theta_{\mu 6}$  can be satisfied, the perching state can be achieved. The friction cone angles  $\theta_{\mu 5}$  and  $\theta_{\mu 6}$  can be determined through experiments. For angles  $\theta_5$  and  $\theta_6$ , we have:

$$\mathbf{F}_5 \cdot \mathbf{n} = |\mathbf{F}_5| |\mathbf{n}| \cos \theta_5. \quad (2.33)$$

$$\mathbf{F}_6 \cdot \mathbf{n} = |\mathbf{F}_6| |\mathbf{n}| \cos \theta_6. \quad (2.34)$$

Where  $\mathbf{n}$  is the normal vector and  $|\mathbf{n}| = 1$ .

Therefore, we can reduce the following:

$$\theta_5 = \cos^{-1}\left(\frac{\mathbf{F}_5 \cdot \mathbf{n}}{|\mathbf{F}_5| |\mathbf{n}|}\right). \quad (2.35)$$

$$\theta_6 = \cos^{-1}\left(\frac{\mathbf{F}_6 \cdot \mathbf{n}}{|\mathbf{F}_6| |\mathbf{n}|}\right). \quad (2.36)$$

**Table 2.1: Properties of components of the entire system.**

Mass [kg]	$m_{L1}$	1.738
	$m_{L2}$	0.022
	$m_{L3}$	0.025
	$m_{L4}$	0.025
Length [mm]	$l_1$	50.000
	$l_2$	120.000
	$l_s$	61.200
	$l_{o2}$	60.000
	$l_{o4}$	21.000
	$a$	7.500
	$b$	10.800
	$c$	100.000
	$s$	-160.000
	$t$	96.000
Static Position Vector	$\mathbf{P}_3$	$(0.000, 50.000)^T$
	$\mathbf{P}_4$	$(0.000, 0.000)^T$
	$\mathbf{P}_{L3}$	$(-2.000, 49.000)^T$

Thus, we can determine whether perching space is available by comparing the relationship between  $\theta_5$  and  $\theta_{\mu 5}$ , and  $\theta_6$  and  $\theta_{\mu 6}$ . The simulation result is derived using the parameters in Table 2.1. For different  $s$  values with an arbitrary target thickness  $L$  and embedded depth  $x$ , the range of the available perching space is summarized as shown in Figure 2.11. In this figure, it is difficult to show all cases of  $s$  with different values. Therefore, we list the cases of  $s$  in the range of -60 mm to -220 mm, with an interval of 20 mm.

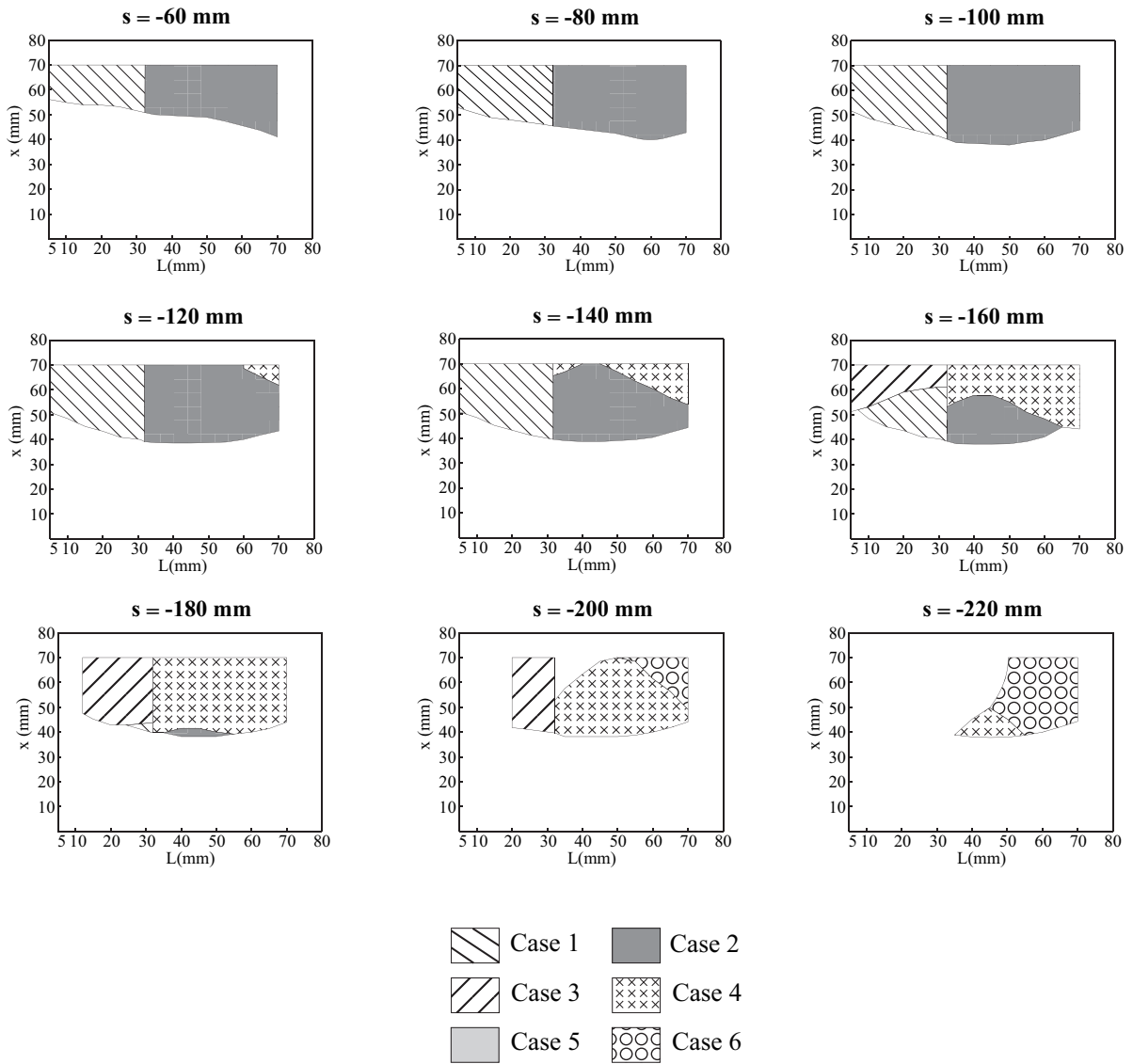


**Figure 2.11: Theoretical value conclusion when value of  $s$  varies.**

### 2.4.3 Necessary contact condition for perching

Although the contact points  $P_5$  and  $P_6$  are calculated in previous section, the achievement of actual contact conditions still need to be considered. As shown in Figure 2.12(a), if the embedded depth  $x$  is large enough, it is possible to make the entire device perch successfully. However, as shown in Figure 2.12(b), when the embedded depth  $x$  is too small, that is, if the edge of the object is to the left of the trajectory of farthest point of Link 3, it will fail to make the perching achieve. Therefore, it is necessary to analysis the

relationship between the embedded depth  $x$  and the trajectory of farthest point of Link 3.

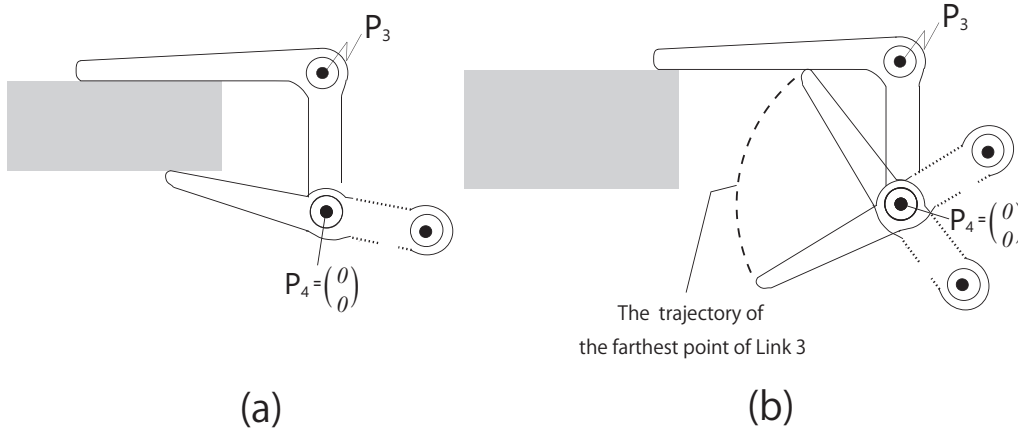


**Figure 2.12: Necessary contact condition for perching.**

According to equation.(2.23), we obtained the coordinates of all the boundary points of  $P_{5x}$ , and summarized the minimum embedded depths in Table 2.2.

**Table 2.2: Necessary contact condition for perching.**

L (mm)	Outmost coordinate of $P_{5x}$ (mm)	Minimum embedded depth (mm)
5.0	-50.0	50.0
10.0	-52.0	48.0
15.0	-55.0	45.0
20.0	-54.0	46.0
25.0	-57.0	43.0
30.0	-59.0	41.0
35.0	-62.0	38.0
40.0	-62.0	38.0
45.0	-62.0	38.0
50.0	-63.0	37.0
55.0	-60.0	40.0
60.0	-58.0	42.0
65.0	-53.0	47.0
70.0	-44.0	56.0

## 2.5 Experiment

In this section, we describe an experiment on perching. In the experiment, we evaluated the possibility of perching when the gripper device was aimed at the target planes with varying thicknesses. According to the experiment, the actual plane perching conditions were clearly executed, and the process of comparing the experimental and theoretical data is presented in this section.

### 2.5.1 Friction coefficient measuring experiment.

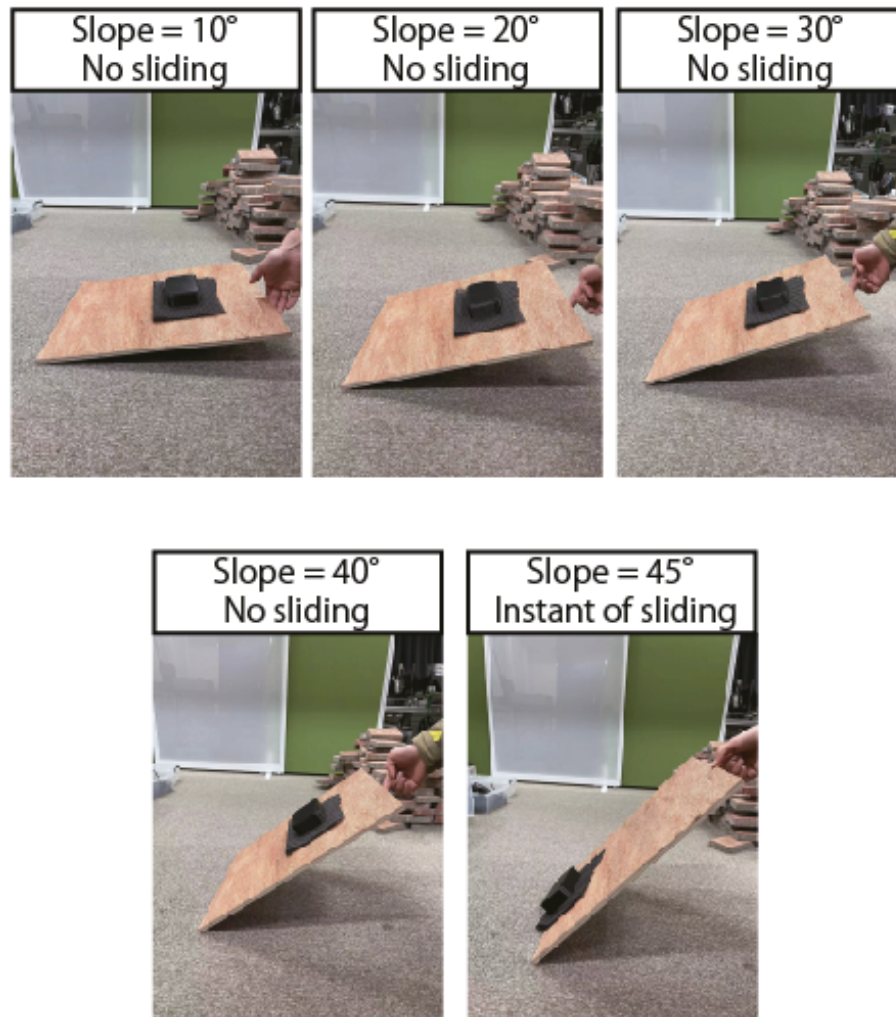


Figure 2.13: The measurement of the friction coefficient.

As shown in Figure 2.13, the measuring experiment of the friction coefficient is given. To judge whether or not that  $\theta_5$  and  $\theta_6$  are smaller than  $\theta_{\mu 5}$  and  $\theta_{\mu 6}$  respectively, it is necessary to conduct the friction coefficient measuring experiment first. Since the methods for measuring  $\theta_{\mu 5}$  and  $\theta_{\mu 6}$  are the same, here we only take the measuring of  $\theta_{\mu 5}$  as an example to illustrate the experiment.

A wooden board, which surface roughness is basically the same as the perching target is prepared. We also prepared a block with the same material as the proposed gripper as the experimental object. (Since the part of the contact point  $P_{5x}$  is wrapped with anti-slid, here we also put the anti-slid between the wooden board and the block.) We place the block and the anti-slid in the middle of the board, and then lift one side of the board slowly. At the beginning, the block did not slide due to the elevation of the board. However, when we lift one side of the wooden board to approximately  $45^\circ$  to the ground, it sided at the moment. Then we recorded this angle as the friction coefficient. After that, in the same way, we measured  $\theta_{\mu 6}$  is  $40^\circ$ .

## 2.5.2 Perching experiment

**Table 2.3: Perching experimental result.**

L (mm)	Min x (mm)	Max x (mm)
5.0	50.0	70.0
10.0	48.0	70.0
15.0	45.0	70.0
20.0	46.0	70.0
25.0	43.0	70.0
30.0	41.0	70.0
35.0	38.0	70.0
40.0	38.0	70.0
45.0	38.0	70.0
50.0	37.0	70.0
55.0	40.0	70.0
60.0	42.0	70.0
65.0	47.0	70.0
70.0	56.0	70.0

In the experiment, we selected boards with thicknesses ranging from 5 mm to 70 mm. Table 2.3 shows the correspondence between different cases with different plane thicknesses and different embedded depths in the perching experiment. By comparing the theoretical and experimental values shown in Figure 2.14, the area in the shadow (50% transparency) indicates the experimental result. We can see that the common areas of the theoretical value and experimental value account for a considerable proportion. The comparison in Figure 2.14 demonstrates the accuracy of the analysis performed in the previous sections.

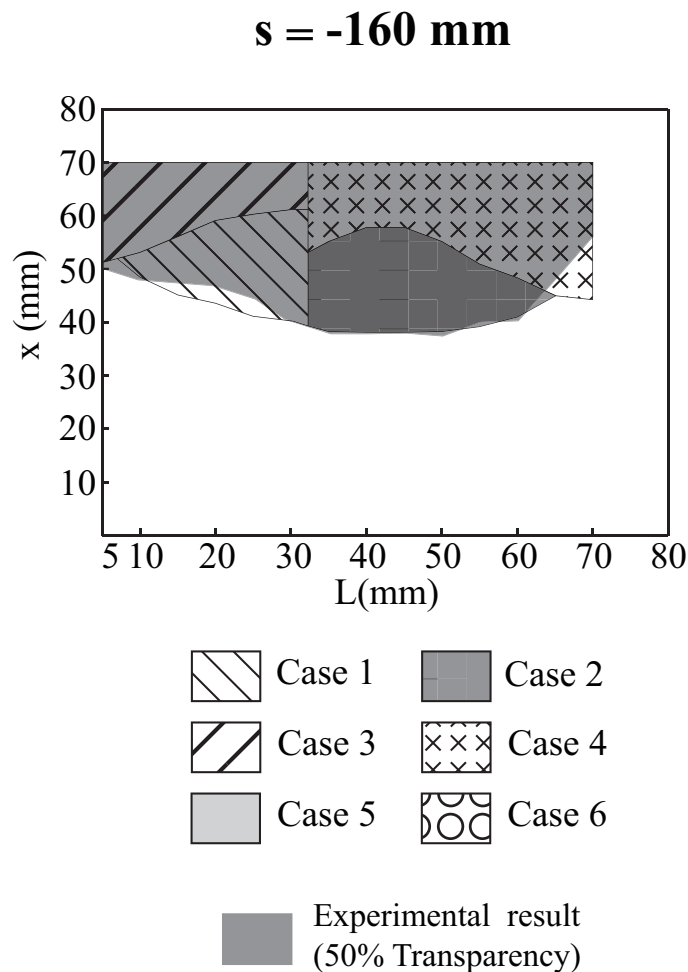


**Figure 2.14: Comparison of theoretical value and experimental value.**

### 2.5.3 Takeoff-perching experiment

To verify the perching motion shown in Figure 2.2, we prepared a table as the perching target, and then the takeoff-perching experiment is conducted. In the takeoff-perching experiment, the multicopter was able to release from the table and keep hovering for several seconds. Then finally multicopter perch on the table again and end the release - perching again experiment. The whole experiment kept about 27 second from beginning to ending.

We can see that the process of Takeoff-perching experiment can be divided into 3 steps:

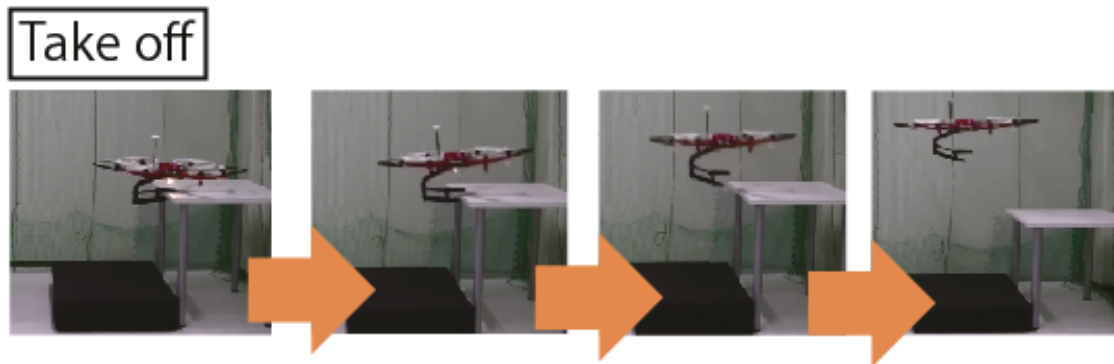


**Figure 2.15: The experiment process of takingoff.**

(1) Takeoff/Release In this process, multicopter's motor active and leave the target table gradually.

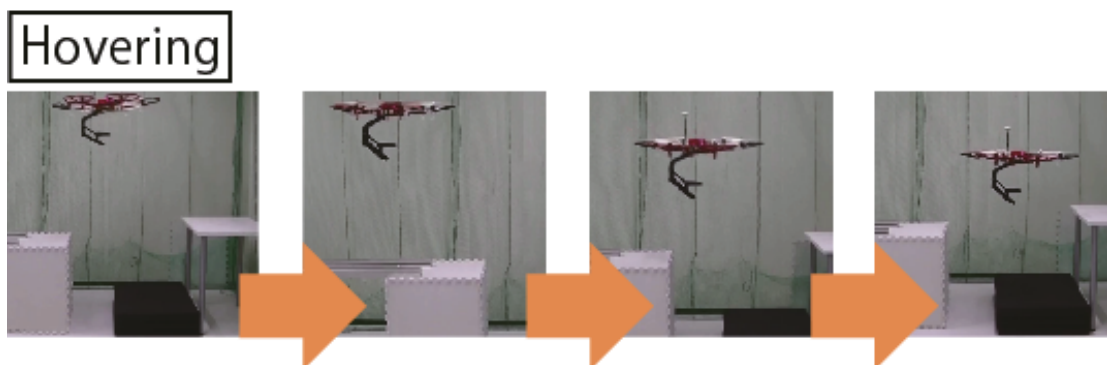


**Figure 2.16: The experiment process of hovering.**

(2) Hovering. After taking off from target table, multicopter start the process of hovering. In this step, multicopter keeps adjusting altitude and angle in order to get into next step.

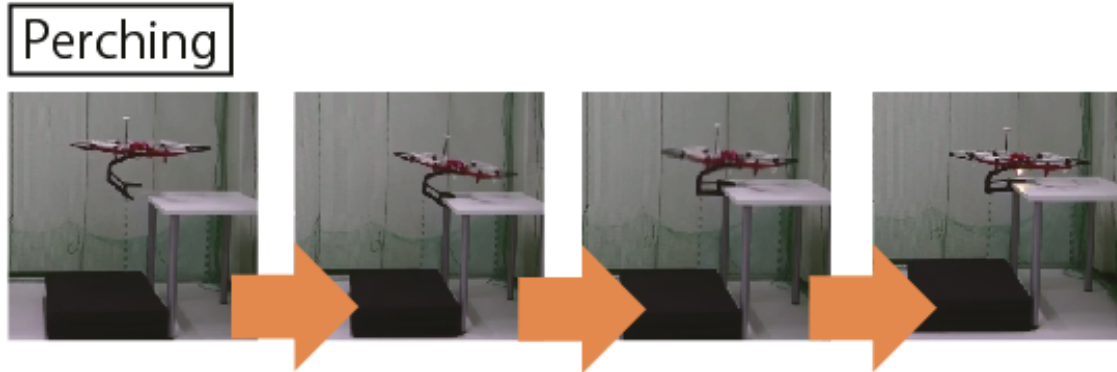


**Figure 2.17: The experiment process of perching.**

(3)Perching (again). In this process, multicopter should has well-adjusted its altitude, angle and position. Then it approaches the target table, land and perch on it eventually.

The purpose of this experiment is to show that my research of development of parallel-link-passive-gripper can not only achieve the mission of taking off and perching on table, but also can achieve release from the target and landing or perching again.

## 2.6 Concluding Remark

In this study, a multicopter carrying with a parallel-link passive gripper for available plane perching was analyzed. The judgment basis and principles were also described. The ideal condition for effective multicopter plane perching was demonstrated by comparing the theoretical and experimental results. The results indicate that there is an optimal range for possible perching for targets with varying plane thicknesses and embedded depths. However, some weaknesses and improvements also need to be considered. For example, so far, we have been unable to determine the restriction and optimal length for our gripper. Therefore, we intend to investigate this aspect in the future.

Although the current study focused on perching on a plane-like target, non-horizontal targets, such as slopes or pipe-like objects, should also be considered as the target for perching. This will increase the possibility of perching in a complex environment.

## **Chapter 3**

# **Development of a passive skid for multicopter landing on rough terrain**

Landing is an essential part of multicopter task operations. A multicopter has relatively stringent requirements for landing, particularly for achieving flatness. Currently, landing on rough terrain with normal skids is difficult. Therefore, research is being conducted to obtain skids capable of landing on rough terrain. In this chapter, a passive skid for multicopter landing on rough terrain is proposed. The proposed device is based on an existing previous study of the multicopter carried with a electric robo-arm only for object manipulation. This innovative idea stems from the aim of giving the multicopter carried with a electric robo-arm the ability to land on various occasions and then the passive skid is designed. By using a slope to simulate a rough terrain, the range of available landing in which a multicopter can maintain its pose and the frictional torque of the passive joint are analyzed. Further, experiments are conducted to demonstrate that landing can be achieved using the skid proposed in our study.

### **3.1 Skid structure and basic landing device**

Figure 3.1 presents the structural diagram of the entire device. The proposed skid consists of two feet with one passive joint. In this proposed device, the arm needs only one degree of freedom (DoF) to move vertically; therefore, for the other parts (except the arm) of the skid, it is not necessary to utilize any other actuator while still achieving its operation. This is an important feature of the device, and the proposed skid struc-

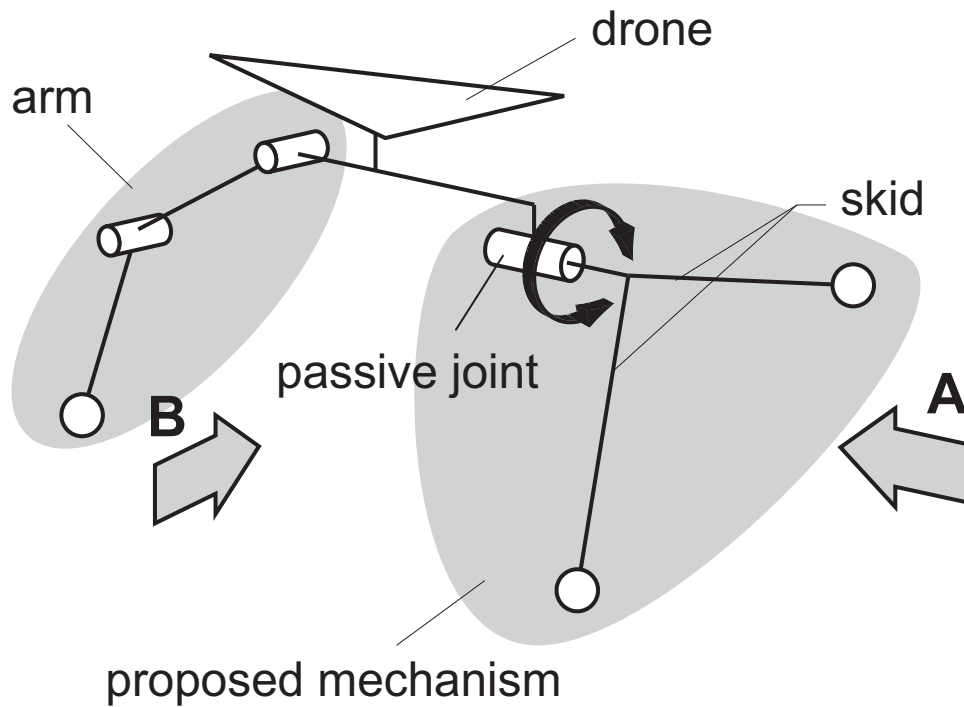


**Figure 3.1: Structure of the skid.**

ture achieves the earlier mentioned objectives of not increasing the weight of the device maximally.

The landing process of the proposed-skid-driven multicopter on a rough terrain is depicted in Figure 3.2 and Figure 3.3. In Figure 3.2(a), (b), and (c), the view is from direction *A*, which is shown in Figure 3.1. Figure 3(b) details the process when landing. When descending, one side of the foot contacts the ground initially, and with the multicopter in a horizontal state, the passive joint rotates. Finally, the other side of the foot descends and then lands on the lower-level ground, as presented in Figure 3.2(c).

In Figures 3.3(a) and (b), the view is from direction *B*, and they display the scenario after the two feet have landed. As shown in Figure 3.3(b), using the degree of freedom of the arm, its front-end can be grounded while keeping the multicopter horizontal.

In summary, the skid-driven multicopter can land on a rough terrain and maintain its horizontal attitude during the entire process with a three-point (two feet and one arm) contact with the ground surface. In the entire process, we assume that there is no sliding

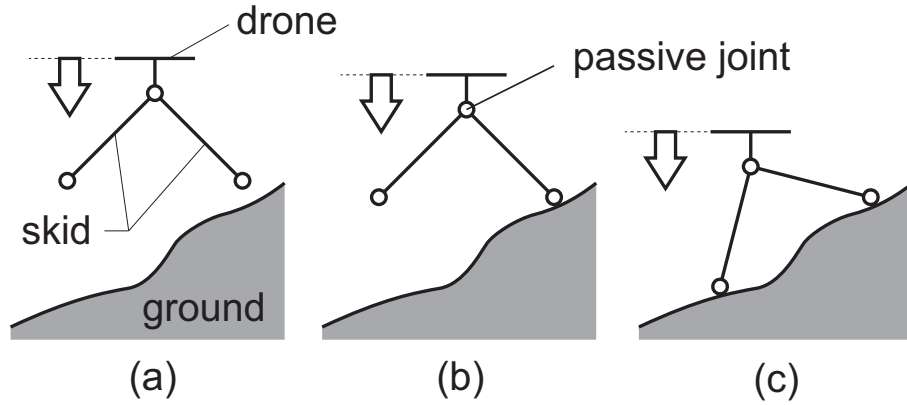


**Figure 3.2:** Proposed skid landing flow as seen from direction A.

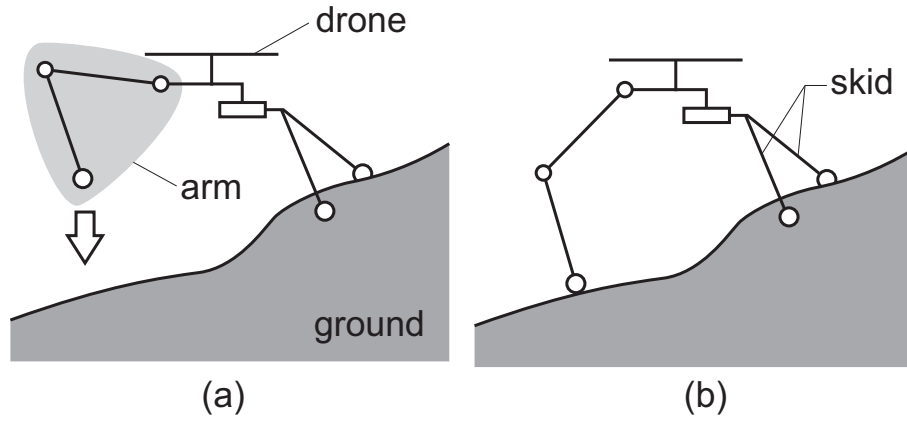


**Figure 3.3:** Arm and landing flow as seen from direction B.

at the contact points when the arm and feet land on the terrain and the lengths between contact points and multicopter remain unchanged. Thus, we can consider that if the skid-driven multicopter maintains its horizontal state when landing, it can remain in that pose after landing.

## 3.2 Range of slopes for available landing

In this section, we present an analysis of the range of slopes for the available landing of the skid-driven multicopter. As displayed in Figure 3.4, we assume that the contact points at which the arm and the skid contact a slope are  $P_f$ ,  $P_{r1}$  and  $P_{r2}$ . Furthermore, if the center of gravity (COG) of the entire device can be inside the triangle consisting of

$P_f P_{r1} P_{r2}$ , the skid-driven multicopter can remain balanced and not fall.

Figure 3.5 is an analytical graph of Figure 3.4 as viewed from direction A. In this case, we analyze from the  $y - z$  plane composed of  $y$  and  $z$  axes and assume that the plane on which the slope is located is plane 3. Then if we define that the inclination angle and the normal vector of plane 3 are  $\alpha$  and  $\mathbf{n} = [a \ b \ c]$ , respectively, we can obtain the followings:

$$\alpha = \tan^{-1} \frac{\partial z}{\partial y}. \quad (3.1)$$

$$ax + by + cz = d. \quad (3.2)$$

From Equation (3.1) and (3.2), we can express inclination angle  $\alpha$  as

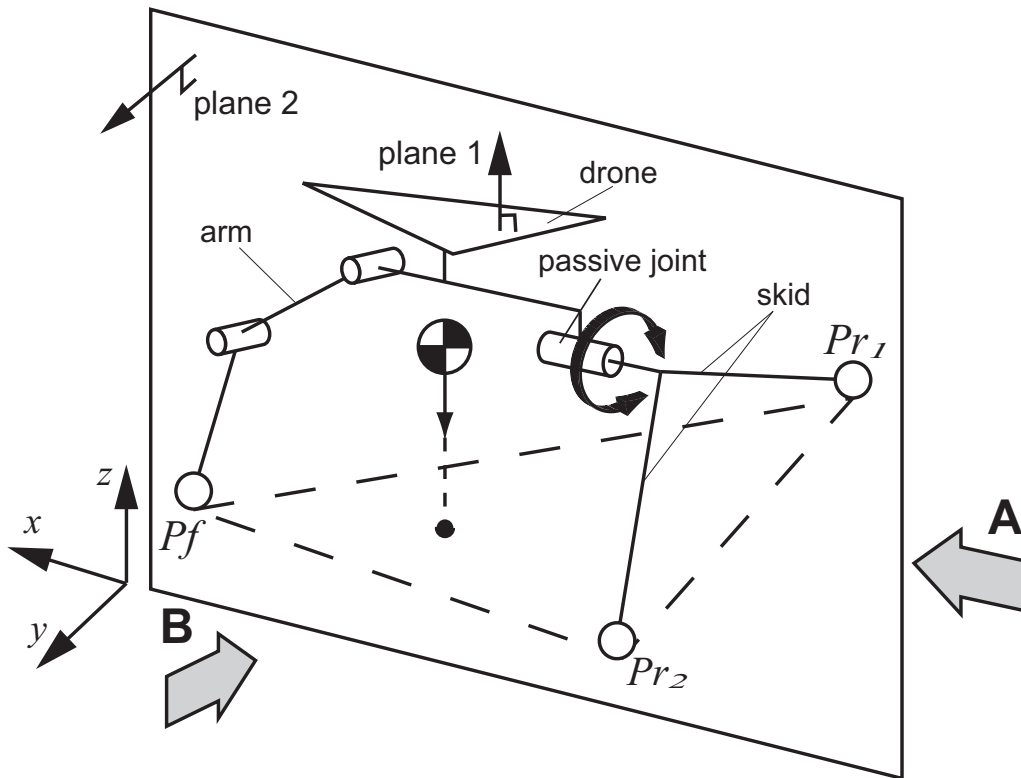
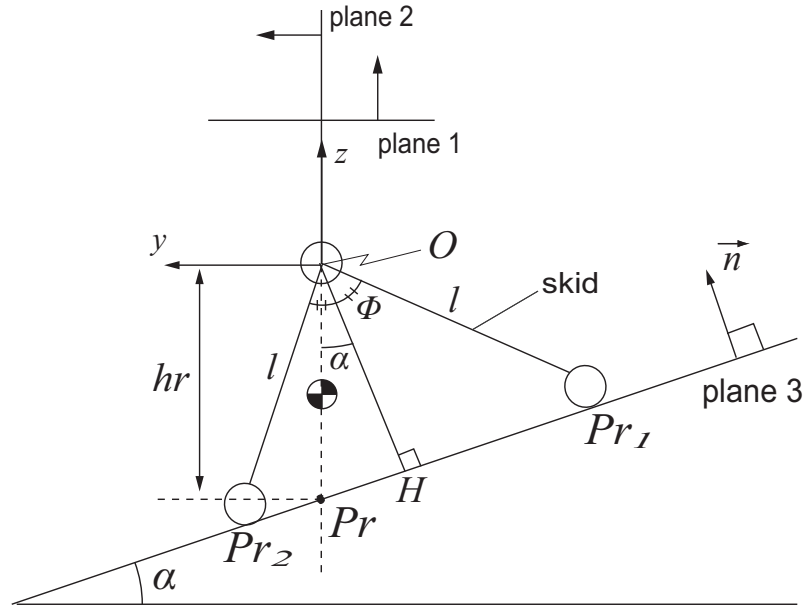


Figure 3.4: Proposed skid structure.



**Figure 3.5: Inclination  $\alpha$  of plane 3 viewed from direction A.**

$$\alpha = -\tan^{-1} \frac{b}{c}. \quad (3.3)$$

Here we define that angle  $\angle HOP_{r1}$  between  $OH$  and  $OP_{r1}$  as  $\phi$  ( $O$  is the origin of the skid axis and  $H$  is the intersection of  $O$  and normal vector of plane 3). The location of COG of the entire system changes with  $\alpha$ , and the limiting case for maintaining the balance is that COG is on  $OP_{r1}$  and  $OP_{r2}$ . Therefore we can obtain the range of inclination angle  $\alpha$  as

$$-\phi < \alpha < \phi. \quad (3.4)$$

Here, we define that the intersection of plane 3 and the perpendicular of COG as  $P_r$  and the length between the origin and  $P_r$  as  $h_r$ . Then  $P_{r1}$ ,  $P_{r2}$ , and  $P_r$  can be obtained as

$$\mathbf{P}_{r1} = \begin{pmatrix} l \cos(\frac{3}{2}\pi + \alpha + \phi) \\ l \sin(\frac{3}{2}\pi + \alpha + \phi) \end{pmatrix}. \quad (3.5)$$

$$\mathbf{P}_{r2} = \begin{pmatrix} l \cos(\frac{3}{2}\pi + \alpha - \phi) \\ l \sin(\frac{3}{2}\pi + \alpha - \phi) \end{pmatrix}. \quad (3.6)$$

$$\mathbf{P}_r = \mathbf{P}_{r2} + t(\mathbf{P}_{r1} - \mathbf{P}_{r2}) = \begin{pmatrix} 0 \\ -h_r \end{pmatrix}. \quad (3.7)$$

where  $t$  is an arbitrary constant.

Then we can obtain  $t$  by substituting  $\mathbf{P}_{r1}$  and  $\mathbf{P}_{r2}$  in Equation (3.7) by Equations (3.5) and (3.6) as

$$t = \frac{\sin(\phi - \alpha)}{2 \cos \alpha \sin \phi}. \quad (3.8)$$

Thus, length  $h_r$  can be obtained by substituting constant  $t$  in Equation (3.7) as

$$h_r = l \cos(\alpha - \phi) - l \tan \alpha \sin(\phi - \alpha). \quad (3.9)$$

Figure 3.6 presents the analytical graph of Figure 3.4 as viewed from direction  $B$ . In this case, we analyze from the  $x - z$  plane composed of  $x$  and  $z$  axes and assume that the inclination angle of plane 3 is  $\beta$ . We define that the distant between  $\mathbf{P}_f$  (which is the contact point of the arm and plane 3) and the  $x$  axis is  $h_f$ . Similarly, we define that the distant between  $\mathbf{P}_r$  (which is the contact point of the feet and plane 3) and the  $x$  axis is  $h_r$ .  $L$  is defined as the distant between  $\mathbf{P}_f$  and  $\mathbf{P}_r$  in the direction of the  $x$  axis. Then the inclination angle,  $\beta$ , can be obtained as

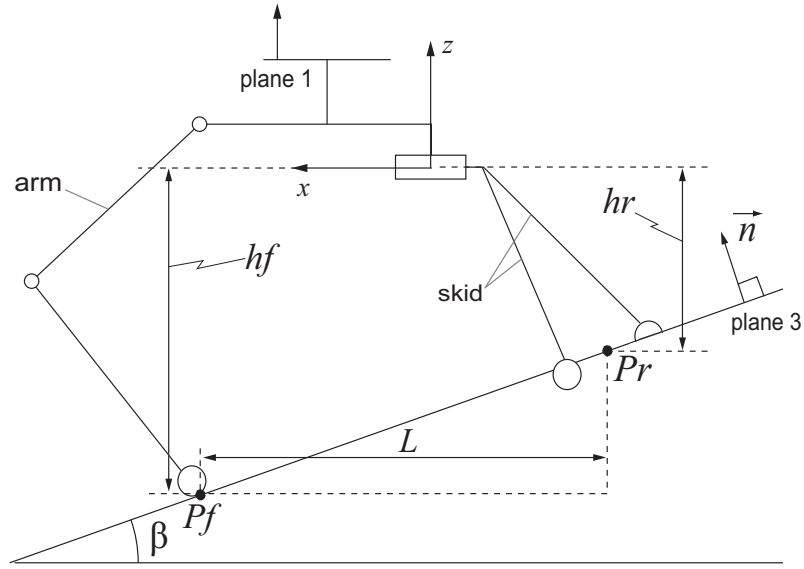


**Figure 3.6:** Inclination  $\beta$  of plane 3 viewed from direction B.

$$\beta = \tan^{-1} \frac{h_f - h_r}{L}. \quad (3.10)$$

Substituting Equation (3.9) into Equation(3.10), we obtain

$$\beta = \tan^{-1} \frac{h_f - l \cos(\alpha - \phi) - l \tan \alpha \sin(\phi - \alpha)}{L}. \quad (3.11)$$

To simplify the calculation, we assume length  $L$  as a constant. When  $\beta$  is maximum, i.e.,  $\beta_{max}$ , we assume that  $\alpha = \alpha_0$  and that  $h_f$  is also maximum value  $h_{fmax}$ .

$$\beta_{max} = \tan^{-1} \frac{h_{fmax} - l \cos(\alpha_0 - \phi) - l \tan \alpha_0 \sin(\phi - \alpha_0)}{L}. \quad (3.12)$$

Similarly, when  $\beta$  is minimum, i.e.,  $\beta_{min}$ , we assume that  $h_f$  is minimum  $h_{fmin}$ .

$$\beta_{min} = \tan^{-1} \frac{h_{fmin} - l \cos(\alpha_0 - \phi) - l \tan \alpha_0 \sin(\phi - \alpha_0)}{L}. \quad (3.13)$$

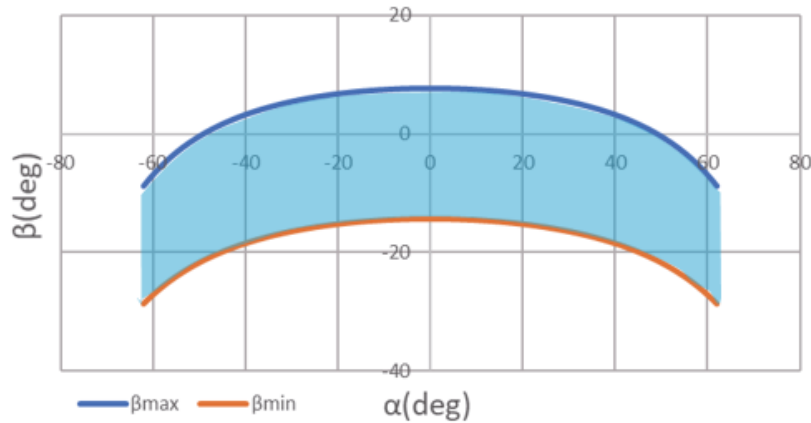


**Figure 3.7: Relationship between plane inclination  $\alpha$  and  $\beta$  that can land, the range between  $\beta_{max}$  and  $\beta_{min}$  (range in blue) expresses the cases when the entire device maintain horizontal.**

In the above equations,  $\alpha_0$  is a case of  $\alpha$ , and it should be in the range shown in Equation (3.4).  $\beta_{max}$  and  $\beta_{min}$  are obtained from Equations (3.12) and (3.13). Therefore, the range of slope for the available landing can be obtained from inclination angles  $\alpha$  and  $\beta$ , and the results are summarized in Figure 3.7.

### 3.3 Frictional torque of passive joint

In this section, we discuss the frictional torque of the passive joint, which plays an important role when landing. However, if the passive joint has no frictional torque, then the skid-driven multicopter will fall down, even if it is slightly tilted. Thus, it is necessary to calculate the angle at which the multicopter will not fall down even if it tilts, owing to the existence of the frictional torque. Prior to that, it is necessary to introduce the following assumptions: (1) For easy analysis and calculation, the surfaces involved in this section are considered as planes; (2) There is no friction between the ground and the skid (The plane is absolutely smooth). The analysis can now be described as follows.

As shown in Figure 3.8, there are several forces existed in the device:  $F_2$ ,  $F_3$  and  $F_4$  stand for the force at the position  $P_2$ ,  $P_3$  and  $F_4$  and force  $F_5$  stands for the force at the CoG of the whole device. When the entire device maintains its static state, we can obtain its statics equations as

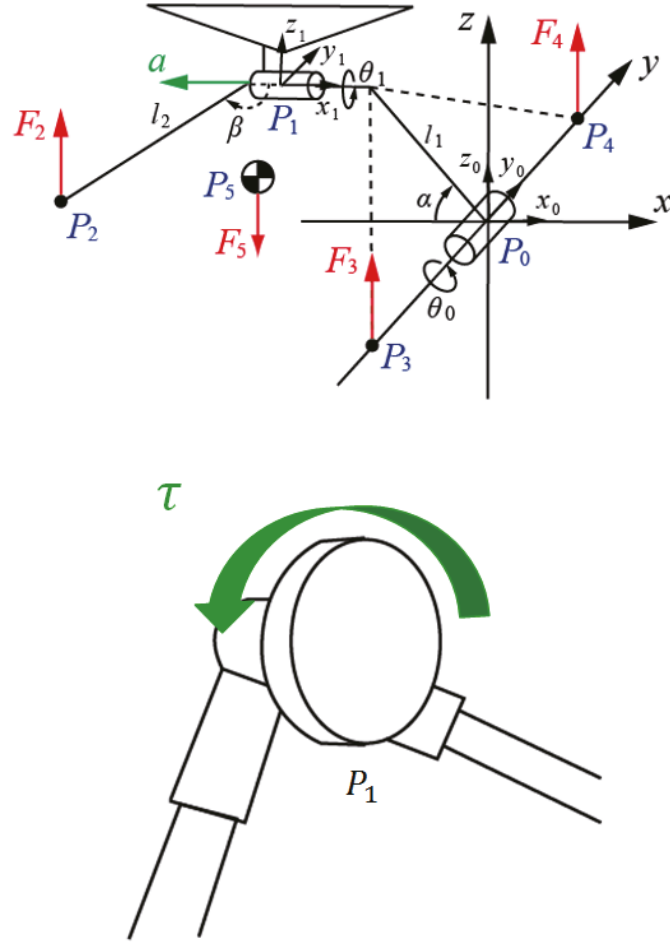


Figure 3.8: Static model of the skid and the frictional torque.

$$\begin{cases} \mathbf{F}_2 + \mathbf{F}_3 + \mathbf{F}_4 + \mathbf{F}_5 = \mathbf{0} \\ \sum_{i=2}^5 (\mathbf{P}_i \times \mathbf{F}_i) = \mathbf{0}. \end{cases} \quad (3.14)$$

From the above equation, we can conclude that if we can calculate the position vector of each force, then all the forces can be obtained. As presented in Figure 3.8, for simplicity, we assume that this skid rotates on an axis passing through  $\mathbf{P}_3$ ,  $\mathbf{P}_4$  and consider a joint that can rotate around the  $y$  axis on  $\mathbf{P}_0$ . The angle at this joint is defined as  $\theta_0$ . Then the passive joint that rotates around the  $a$  axis is defined as  $\mathbf{P}_1$ , and the angle at this joint is defined as  $\theta_1$ . Here, we define the distant between  $\mathbf{P}_0$  and  $\mathbf{P}_1$  as  $l_1$  and the

angle between the  $x$  axis and line  $\mathbf{P}_0\mathbf{P}_1$  as  $\alpha$ .

We assume the front end of the arm, which is contact with the plane, as  $\mathbf{P}_2$ , and when the arm does not move, we do not consider the arm joint. Then the distant between  $\mathbf{P}_1$  and  $\mathbf{P}_2$  is defined as  $l_2$ , and the angle between the passive joint of the rotary axis and line  $\mathbf{P}_1\mathbf{P}_2$  is defined as  $\beta$ .

For the static model analysis,  $\mathbf{P}_3$  and  $\mathbf{P}_4$  are the points at which the front end of the two skids contact the plane. We assume that the distant between  $\mathbf{P}_0$  and  $\mathbf{P}_3$  is  $y_3$  and that between  $\mathbf{P}_0$  and  $\mathbf{P}_4$  is  $y_4$ . Then the coordinates of  $\mathbf{P}_3$  and  $\mathbf{P}_4$  can be described as  $\mathbf{P}_3 = {}^t(0 \ -y_3 \ 0)$  and  $\mathbf{P}_4 = {}^t(0 \ y_4 \ 0)$ , respectively.

We establish different space rectangular coordinate systems at  $\mathbf{P}_0$  and  $\mathbf{P}_1$ . To simplify the explanation, we define  ${}^j\mathbf{P}_i$ .  ${}^j\mathbf{P}_i$  denotes the position vector of  $\mathbf{P}_i$  based on point  $\mathbf{P}_j$  ( $i, j$  are arbitrary real numbers). Another definition of  $\mathbf{R}_m(\theta_n)$  is that it is a coordinate transformation determinant (CTD), which implies that the direction of the vector changes from direction  $n$  to direction  $m$ . Then the coordinate of  $\mathbf{P}_2$  can be obtained by the static model displayed in Figure 3.8.

$$\begin{aligned} {}^0\mathbf{P}_2 &= {}^0\mathbf{P}_1 + \mathbf{R}_y(\theta_0)\mathbf{R}_x(\theta_1){}^2\mathbf{P}_2 \\ &= \begin{pmatrix} -l_1 \cos(\alpha + \theta_0) + l_2 \cos\beta \cos\theta_0 + l_2 \sin\beta \sin\theta_0 \cos\theta_1 \\ -l_2 \sin\beta \sin\theta_1 \\ l_1 \sin(\alpha + \theta_0) - l_2 \cos\beta \sin\theta_0 + l_2 \sin\beta \cos\theta_0 \cos\theta_1 \end{pmatrix}. \end{aligned} \quad (3.15)$$

$\mathbf{P}_5$  denotes the position vector of point  $P_5$ , which is COG of the entire device, and we obtain it by experimental measurement.  $\mathbf{P}_5$  is defined as  $\mathbf{P}_5 = {}^t(x_5 \ y_5 \ z_5)$ .

Here, all the position vectors,  $\mathbf{P}_2$ ,  $\mathbf{P}_3$ ,  $\mathbf{P}_4$ , and  $\mathbf{P}_5$  expressed in Equation (3.14), are obtained. Then the forces can be obtained by Equation (3.14).

$$\boldsymbol{\tau} = (\mathbf{P}_2 - \mathbf{P}_1) \times \mathbf{F}_2. \quad (3.16)$$

Considering the direction, the torque with the unit direction vector,  $\mathbf{a}$ , can be expressed as follows:

$$\mathbf{T} = \mathbf{a}^T \boldsymbol{\tau}. \quad (3.17)$$

Therefore, if the frictional torque in the direction of the rotary axis is defined as  $T_\mu$  and  $T < T_\mu$  can be satisfied, then we can determine that the skid-driven multicopter can remain in its horizontal state without falling.

### 3.4 Prototype of the entire device

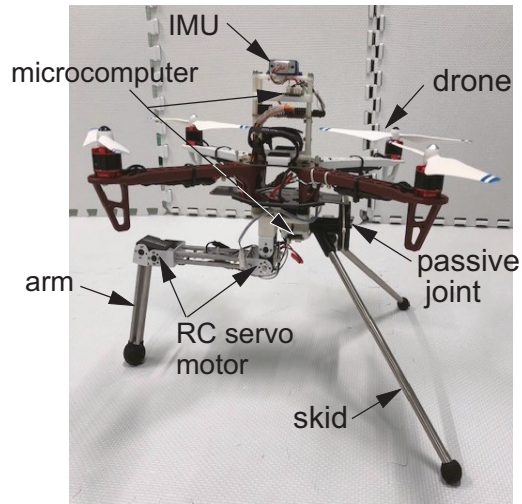


**Figure 3.9: Prototype of the entire device.**

Figure 3.9 displays the prototype of the entire device. It can be divided into two main parts: the multicopter body and the proposed skid. For the multicopter, we selected DJI FlameWheel450 as the carrier and equipped it with an LPMS-CU2 gyroscope (LP-RESEARCH company). The skid has a length of  $l = 300$  mm and two DoFs. The arm is equipped with RC servo motors at the joints, and it can achieve flexible movement under the control by a program. The skid is passive and consists of one passive joint and two feet. Therefore, during the landing maneuver, the multicopter driven by the developed skid will have three contact points with the ground.

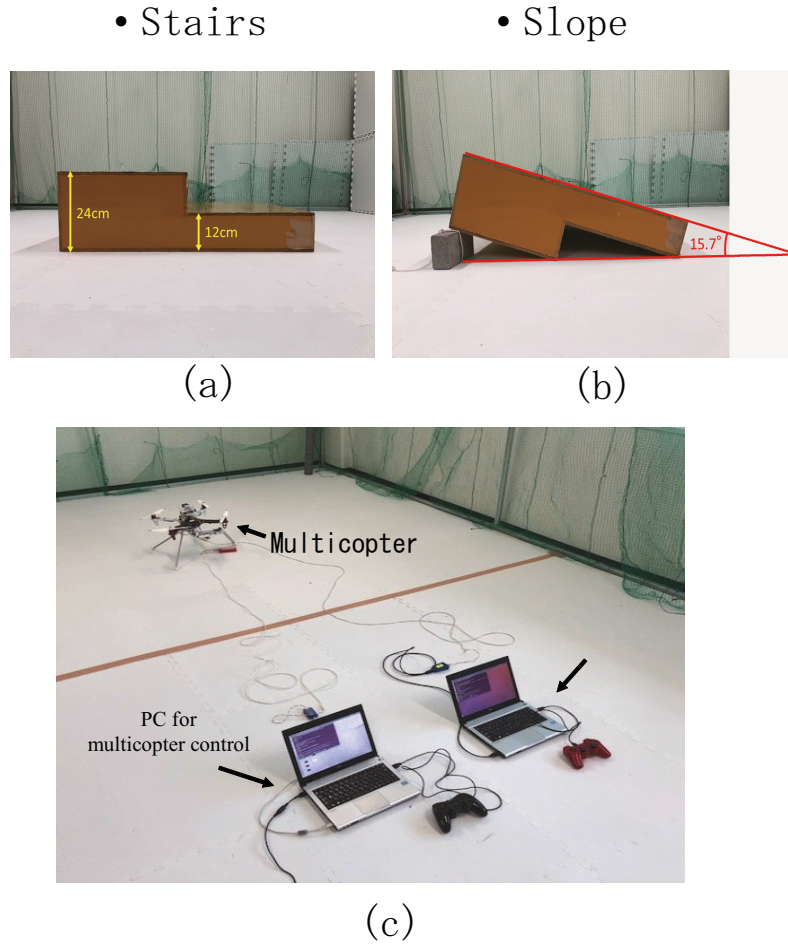


**Figure 3.10: Experimental settings.**

## 3.5 Experiments

### 3.5.1 Experimental settings

For the landing experiment on rough terrain, we utilized two patterns of rough terrain, steps and slopes, which is shown in the Figures 3.10(a) and 3.10(b), to simulate the landing experiment. As shown in Figure 3.10(c), two PCs are utilized for controlling, the left one is for flying the multicopter and the right one is for controlling the robot arm. Besides, the left joystick connected with the PC is for the drone, and the right controller is for the robot arm. Then the landing experiment can be conducted by two operators.

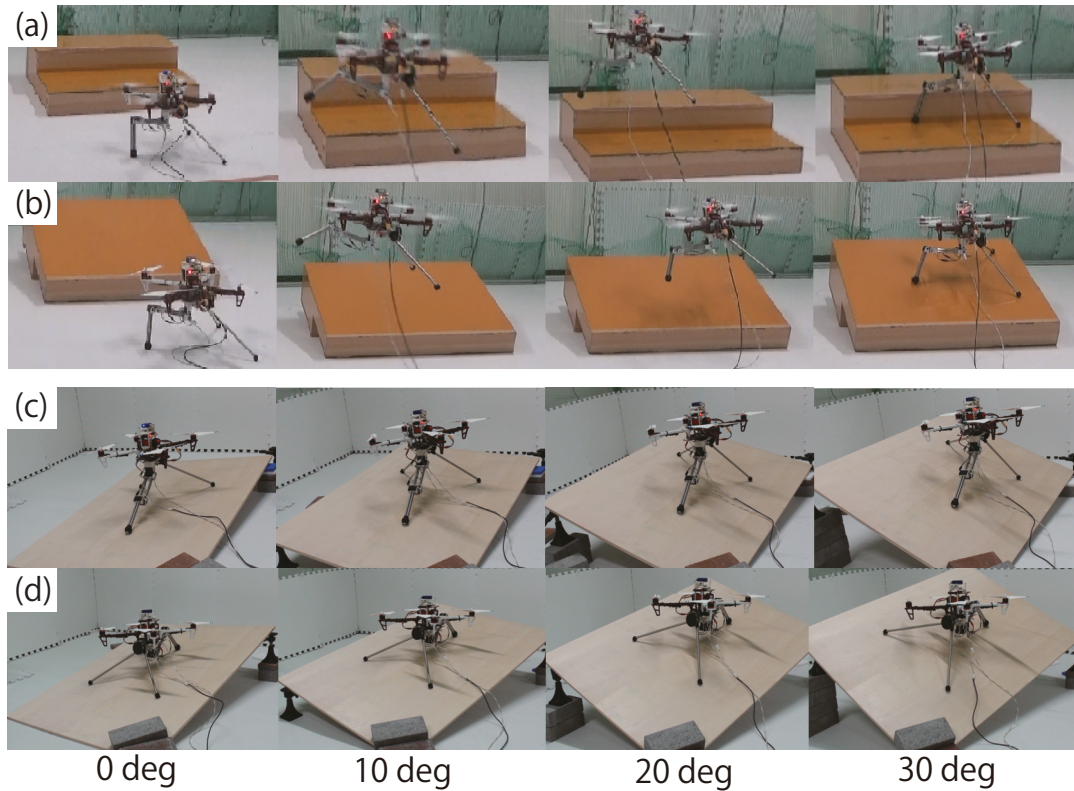


**Figure 3.11:** Experimental result (a) Landing on a 120 mm step (b) Landing on a slope of 16 deg (c) 0 deg, 10 deg, 20 deg and 30 deg when  $\beta$  is  $\beta_{max}$  (d) 0 deg, 10 deg, 20 deg and 30 deg when  $\beta$  is  $\beta_{min}$ .

### 3.5.2 Maintenance of multicopter horizontal states

From the analysis and summary based on Figure 3.7, we have proved that the skid driven multicopter can maintain its horizontal state without falling, within a certain range. Furthermore, we also measured the roll angle and the pitch angle of the skid driven multicopter. Figures 3.11(c), and 11(d) display the cases of  $\beta_{max}$  and  $\beta_{min}$ , respectively, for  $\alpha = 0$  deg, 10 deg, 20 deg and 30 deg.

In addition, the roll and pitch angles of the skid-driven multicopter are shown in Figure 3.12. Remarkably, when the roll and pitch angles approach 0, the skid-driven multicopter can noticeably maintain a horizontal state. However when the inclination angle exceeds 30 deg or is less than -30 deg, the skid cannot maintain its horizontal state and will slide. In this scenario, the friction between the contact points of the feet and the ground is not sufficient so that the posture of the device can be remained only till

approximately 30 deg. Thus, we speculate that if the friction can be relatively larger, then the posture will be maintained with a tilt angle of more than 30 deg.

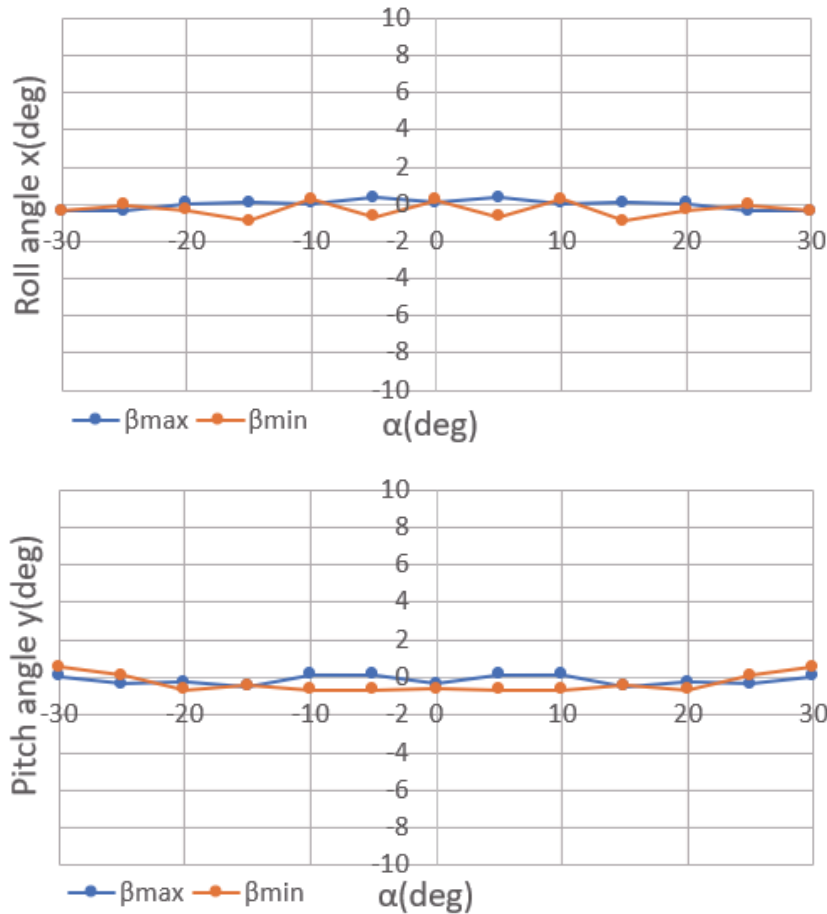


**Figure 3.12: Relationship between incilation  $\alpha$  and roll angle and pitch angle of the multicopter based on the result of Figure 3.7.**

### 3.5.3 Verification of frictional torque of passive joint

In this subsection, we discuss the range of angles for which the skid-driven multicopter remains in a horizontal state without falling. This is based on the relationship between the inclination angle  $\theta_1$ , and the frictional torque of the passive joint, which was discussed in Section V. We used a plastic wrap band around the passive joint to adjust the tightness (roughness) and divide it into three patterns. Then, we defined the torques generated by the frictional force as  $\tau_{max_1}$ ,  $\tau_{max_2}$ , and  $\tau_{max_3}$  corresponding to the three patterns of tightness. Following this, we conducted the experiment (Figure 3.13).

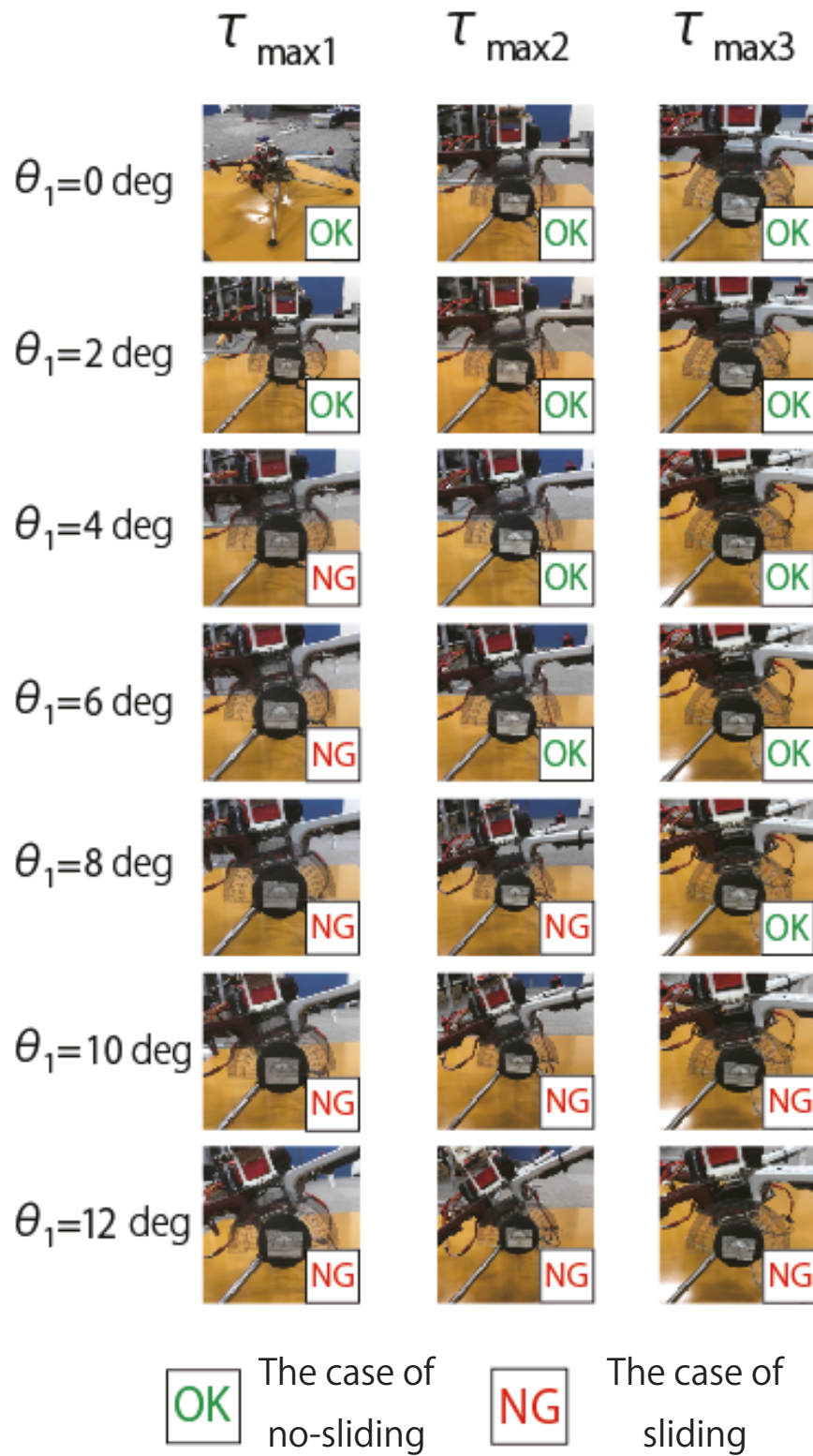


**Figure 3.13: Experimental verification of the frictional torque of the passive joint.**

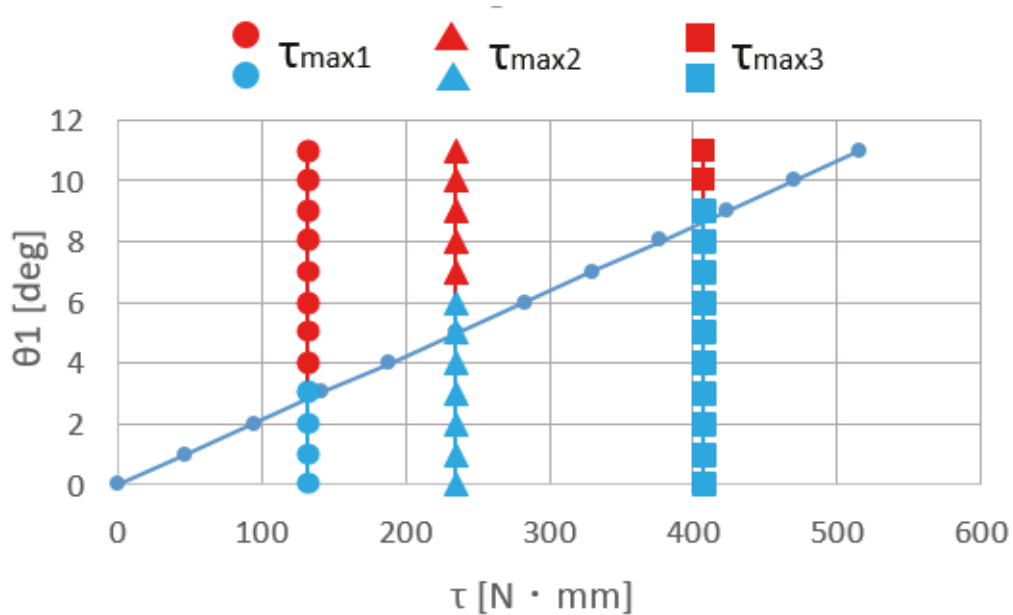


**Figure 3.14: Relationship between the passive joint and the frictional torque.**

The relationship between the passive joint and the frictional torque is shown in Figure 3.14. The patterns under the line in Figure 3.14 represents the cases when the skid-driven multicopter maintains its horizontal state without sliding and the patterns above the line denotes the cases when the device tilts. The graph exhibits that the experimental result is similar to the expected theoretical value.

### 3.5.4 Landing experiment on rough plane

In this subsection, the experiment of the skid-driven multicopter landing on a non-planar terrain is presented. To model a non-planar terrain, we used a slope with a height of 120 mm and an inclination angle of  $16^\circ$  (as displayed in Figures 3.11(a) and 3.11(b)).

## 3.6 Concluding Remark

In this study, a passive skid was developed enabling a multicopter to land on rough terrain. We have expanded the function based on previous research on the electric-arm-equipped multicopter and successfully combined the arm and the skid so that it allows the multicopter to both manipulate and land in complex environments.

Although the design of the passive landing device is still in its infancy, we are planning to conduct additional experiments. For example, we want to determine how different materials affect the landing result. Therefore, we decided to conduct another comparison experiment by using various materials on the ends of the feet and then analyze the results. We expect this research to have meaningful implications for the future in this field.

## **Chapter 4**

### **Analysis of a multicopter carried with passive skid for rough terrain landing**

In Chapter 3, we described an underactuated passive skid for multicopter landing on a rough terrain. However, in Chapter 3, the posture and condition of link 1 and link 2 are not considered. Although the passive joint and the skid play an important role in rough terrain landing, the robot arm, which is consisted of link 1 and link 2, is also important for landing. Therefore, in this chapter, we focus on the influence of different postures of link 1 and link 2 on the possibility of multicopter's rough terrain landing. We reconstruct the static model of the entire device described in Chapter 3, and analyzed the conditions under which the arm and skid can contact the arbitrary plane and the COG (Center of Gravity), which includes the mass of passive skid, multicopter body and each link of the robot arm. Further, we proposed a method to analyze whether the entire device can land stably. By analyzing that the projection of the entire device's COG is inside or outside the triangle, that comprises the contact point between the device and the uneven ground, we can determine whether the device can land successfully and the condition for capable landing is concluded. After the numerical analysis, the verification experiment is conducted, and by comparing the result of analysis with the experiment, the accuracy of the analysis can be demonstrated.

## 4.1 Reconstruction of the static model

To analyze the contact condition between the arm and the plane, we decomposed the device again, and reconstructed the static model as illustrated in Figure 4.1. Because there is an inevitable occlusion relationship in the three-dimensional anatomical figure, we have utilized dotted lines to mark the occluded part. Similarly, auxiliary lines are also indicated by dashed lines.

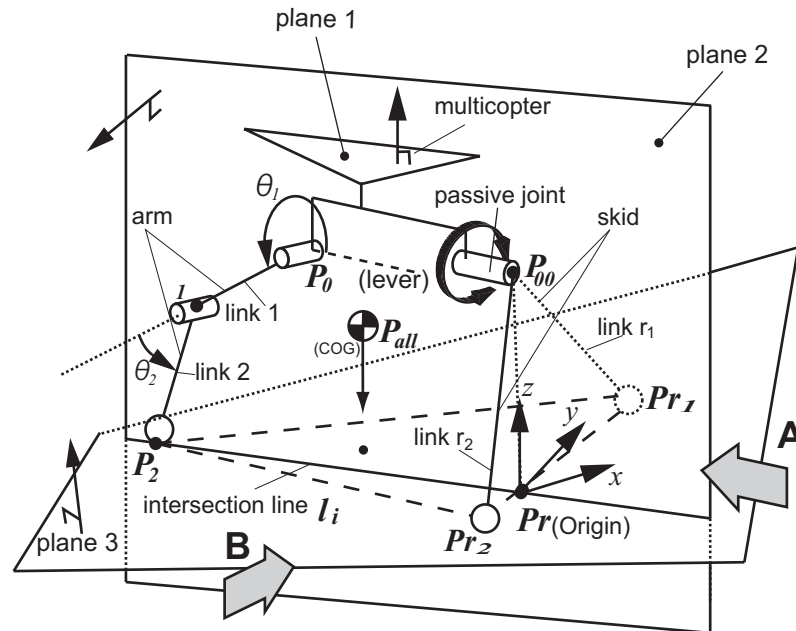


**Figure 4.1: Static model of the entire device.**

Figure 4.1 reproduces the state of a landed device, but this time we concentrate on the robot arm model analysis. As illustrated in Figure 4.1, we assume that there are three planes existing in the environment. Plane 1 denotes the lever plane, and also, to make the multicopter take off smoothly again, the multicopter must maintain its horizontal posture constantly. Thus, plane 1 is not only the lever plane, but also the plane where the body of multicopter is located. We define the direction of gravity as the direction of the  $z$  axis, and plane 2 contains the axis of the passive joint and the normal vector of plane 1. Further, we define that the normal vector of plane 2 as  $y$  axis and the  $x$  axis can be obtained. The line of intersection is denoted as  $l_i$ . We make a perpendicular line downward through the horizontal extension line of the passive joint  $P_{00}$ , and intersect the connection line of feet

$P_{r1}$  and  $P_{r2}$  at point  $P_r$ . Based on the origin  $P_r$ , the space rectangular coordinate system is established. Plane 3 is the plane for landing, the passive joint  $P_0$ , the position vectors, included  $P_0 \in R^3$ ,  $P_1 \in R^3$  and  $P_2 \in R^3$  on the arm are also on plane 2. Two contact points of the passive skid on plane 3 are assumed as  $P_{r1}$  and  $P_{r2}$ . Thus, including  $P_2$ ,  $P_{r1}$  and  $P_{r2}$ , there are three contact points on plane 3 and they are supporting the entire device.

## 4.2 The capable range of slope for landing

For landing on an uneven ground, it is necessary to know what level of ground can make the proposed device land successfully. As mentioned in the previous section, we established that plane 3 is the landing slope, and the most important characteristic, the gradient, will affect landing status. Therefore, the analysis of the capable landing range is given as follows.

### Anatomy of the Static Model

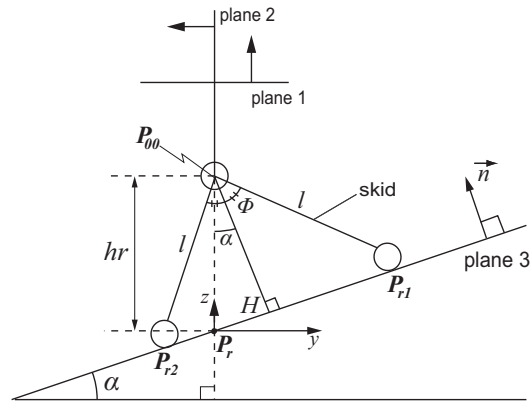
Figures 4.2(A) and (B) are analytical graphs of Figure 4.1 viewed from direction A (the view from x direction) and B (the view from y direction). Aforementioned, plane 2 contains the axis of the passive joint and the normal vector of plane 1, thus plane 2 can be expressed as  $y = 0$ . We define the normal vector of plane 3 as  $\mathbf{n} = [a \ b \ c]^t$ , and we obtain:

$$ax + by + cz = 0. \quad (4.1)$$

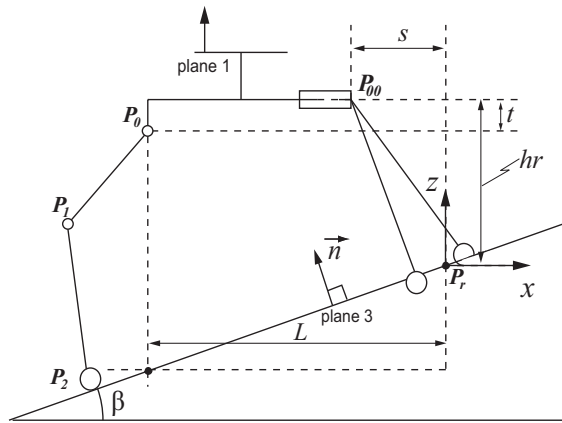
We define that the inclination angle viewed from direction A is  $\alpha$ , and it can be obtained as:

$$\alpha = -\tan^{-1} \frac{b}{c}. \quad (4.2)$$

In Figure 4.2(A) we illustrate that  $H$  is the intersection of plane 3 and the normal



(A)



(B)

**Figure 4.2: View of the device from A and B directions.**

vector of plane 3, which passes through  $P_{00}$ . Then the angle  $\angle HP_{00}P_{r1}$  is defined as  $\phi$ .

We illustrate that the distance between  $P_{00}$  and  $P_r$  is  $h_r$ , and it can be obtained as:

$$h_r = \frac{l \cos \phi}{\cos \alpha}. \quad (4.3)$$

Therefore the position vector of  $P_{r1}$  and  $P_{r2}$  can be obtained as:

$$\mathbf{P}_{r1} = \begin{pmatrix} P_{r1x} \\ P_{r1y} \\ P_{r1z} \end{pmatrix} = \begin{pmatrix} 0 \\ (h_r \sin \alpha + \sin \phi) \cos \alpha \\ (h_r \sin \alpha + \sin \phi) \sin \alpha \end{pmatrix}. \quad (4.4)$$

$$\mathbf{P}_{r2} = \begin{pmatrix} P_{r2x} \\ P_{r2y} \\ P_{r2z} \end{pmatrix} \quad (4.5)$$

$$= \begin{pmatrix} 0 \\ (l \sin \phi - h_r \sin \alpha) \cos(\pi + \alpha) \\ (l \sin \phi - h_r \sin \alpha) \sin(\pi + \alpha) \end{pmatrix}.$$

Figure 4.2(B) is the analytical graph of Figure 4.1 viewed from direction B and similarly we can obtain that:

$$\beta = -\tan^{-1} \frac{a}{c}. \quad (4.6)$$

We denote that the horizontal and vertical distances between  $\mathbf{P}_r$  and  $\mathbf{P}_{00}$  are  $s$  and  $h_r$ , respectively. Thus the position vector of  $\mathbf{P}_{00}$  can be obtained as:

$$\mathbf{P}_{00} = \begin{pmatrix} P_{00x} \\ P_{00y} \\ P_{00z} \end{pmatrix} = \begin{pmatrix} -s \\ 0 \\ h_r \end{pmatrix}. \quad (4.7)$$

For the position vector of  $\mathbf{P}_0$ , we denote that the horizontal distance between  $\mathbf{P}_r$  and  $\mathbf{P}_0$  is  $L$ , and the vertical distance between  $\mathbf{P}_{00}$  and  $\mathbf{P}_0$  is  $t$ . Therefore the position vector

of  $\mathbf{P}_0$  can be obtained as:

$$\mathbf{P}_0 = \begin{pmatrix} P_{0x} \\ P_{0y} \\ P_{0z} \end{pmatrix} = \begin{pmatrix} -L \\ 0 \\ h_r - t \end{pmatrix}. \quad (4.8)$$

As illustrated in Figure 4.1, the angle between link 1 and the lever is  $\theta_1$ , and the angle between link 2 and the extension line of link 1 is  $\theta_2$ . We assume that the length of link 1 and link 2 are  $l_1$  and  $l_2$ . Therefore,  $\mathbf{P}_1$  and  $\mathbf{P}_2$  can be expressed as:

$$\mathbf{P}_1 = \begin{pmatrix} P_{1x} \\ P_{1y} \\ P_{1z} \end{pmatrix} = \mathbf{P}_0 + \begin{pmatrix} l_1 \cos \theta_1 \\ 0 \\ l_1 \sin \theta_1 \end{pmatrix}. \quad (4.9)$$

$$\mathbf{P}_2 = \begin{pmatrix} P_{2x} \\ P_{2y} \\ P_{2z} \end{pmatrix} \quad (4.10)$$

$$= \mathbf{P}_0 + \begin{pmatrix} l_1 \cos \theta_1 + l_2 \cos(\theta_1 + \theta_2) \\ 0 \\ l_1 \sin \theta_1 + l_2 \sin(\theta_1 + \theta_2) \end{pmatrix}.$$

### 4.2.1 Judgment of the ground-contacting state

To assess the ground-contacting condition, contact points  $\mathbf{P}_2$ ,  $\mathbf{P}_{r1}$  and  $\mathbf{P}_{r2}$  are considered, and the view is from the  $y$  direction. Hence, the plane 3 and the device are simplified as points and lines. The intersection of plane 2 and plane 3 is:

$$ax + cz = 0. \quad (4.11)$$

$P_2$  is on that line, thus we obtain

$$aP_{2x} + cP_{2z} = 0. \quad (4.12)$$

When  $\theta_2$  is a constant, and if link 1 rotates around  $P_0$ , the trajectory of  $P_2$  is a circle, and the distance from  $P_2$  to  $P_0$  is the radius  $r$ . We define the functional expression of the circle as:

$$(P_{2x} - P_{0x})^2 + (P_{2z} - P_{0z})^2 - r^2 = 0. \quad (4.13)$$

By simultaneous equation (4.12) and (4.13), and to concretize  $P_{0x}$  and  $P_{0z}$  by equation (4.8), we obtained

$$AP_{2x}^2 + BP_{2x} + C = 0. \quad (4.14)$$

where:

$$A = 1 + \frac{a^2}{c^2}. \quad (4.15)$$

$$B = \frac{2a(h_r - t) - 2L}{c}. \quad (4.16)$$

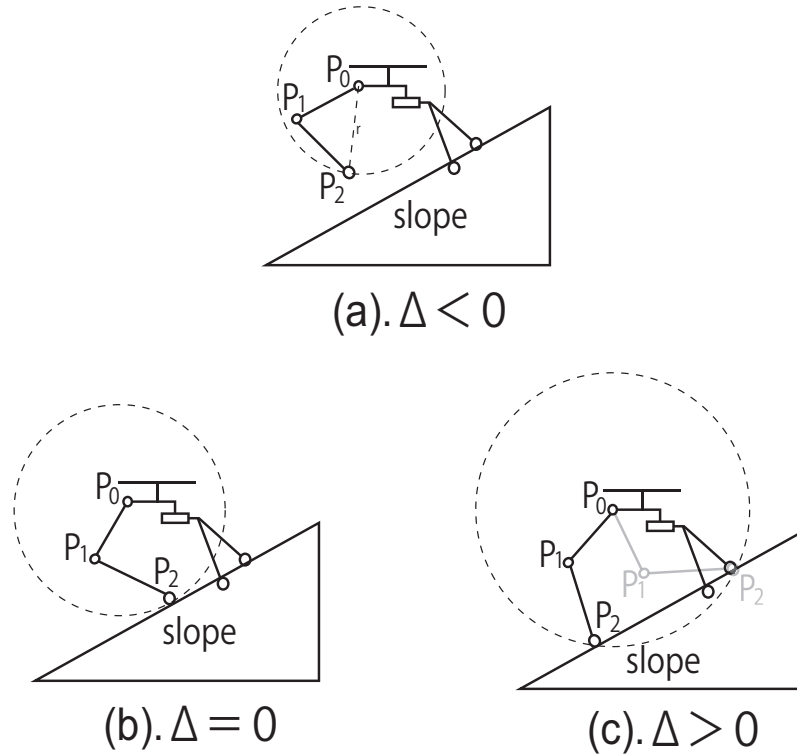


**Figure 4.3: The positional relationship between  $p_2$  and the slope.**

$$C = -L^2 + (h_r - t)^2 - r^2. \quad (4.17)$$

and the discriminant as:

$$\Delta = B^2 - 4AC. \quad (4.18)$$

As illustrated in Figure 4.3, for the discriminant  $\Delta$ , if the condition  $\Delta \geq 0$  can be satisfied, we can conclude that point  $P_2$  and plane 3 have at least one intersection.

### 4.2.2 Condition of non-tilting

The entire device can be divided into four parts: the Part 1 is the link 1, the Part 2 is the link 2 and the multicopter body can be defined as the Part 3. The skid, which

comprises link  $l_{r1}$ , link  $l_{r2}$  and the passive joint, is defined as the Part 4. The position vectors of the COG of Part  $i$  ( $i = 1, 2, 3, 4$ ) are defined as  $\mathbf{P}_{ai}$  ( $i = 1, 2, 3, 4$ ). We define that the mass of each part as  $m_i$ , ( $i = 1, 2, \dots, 4$ ), and then the COG of each part can be obtained. Then the COG of the entire device can be obtained as:

$$\mathbf{P}_{all} = \begin{bmatrix} P_{allx} \\ P_{ally} \\ P_{allz} \end{bmatrix} = \begin{bmatrix} \frac{\sum_{i=1}^4 m_i x_{ai}}{\sum_{i=1}^4 m_{ai}} \\ \frac{\sum_{i=1}^4 m_i y_{ai}}{\sum_{i=1}^4 m_{ai}} \\ \frac{\sum_{i=1}^4 m_i z_{ai}}{\sum_{i=1}^4 m_{ai}} \end{bmatrix}. \quad (4.19)$$

As illustrated in Figure 4.1, the contact points  $\mathbf{P}_2$ ,  $\mathbf{P}_{r1}$  and  $\mathbf{P}_{r2}$  form a triangle located on plane 3. Thus, if the projection of the COG of the entire device can remain inside the triangle consisting of  $\mathbf{P}_2\mathbf{P}_{r1}\mathbf{P}_{r2}$ , the skid-driven multicopter can remain balanced. If the COG stays outside the triangle, the multicopter will tilt.

In this analysis, it is only necessary to consider its projection on the  $x - y$  plane. Therefore, we define that  $\mathbf{p}_{all}$  as COG coordinate of the entire device on  $x - y$  plane, and we define:

$$\mathbf{p}_{all} = \begin{pmatrix} P_{allx} \\ P_{ally} \end{pmatrix}. \quad (4.20)$$

The projection of  $\mathbf{P}_{r1}$ ,  $\mathbf{P}_{r2}$ , and  $\mathbf{P}_2$  are onto the  $x - y$  plane respectively, we define:

$$\mathbf{p}_{r1} = \begin{pmatrix} P_{r1x} \\ P_{r1y} \end{pmatrix}. \quad (4.21)$$

$$\mathbf{p}_{r2} = \begin{pmatrix} P_{r2x} \\ P_{r2y} \end{pmatrix}. \quad (4.22)$$

$$\mathbf{p}_2 = \begin{pmatrix} P_{2x} \\ P_{2y} \end{pmatrix}. \quad (4.23)$$

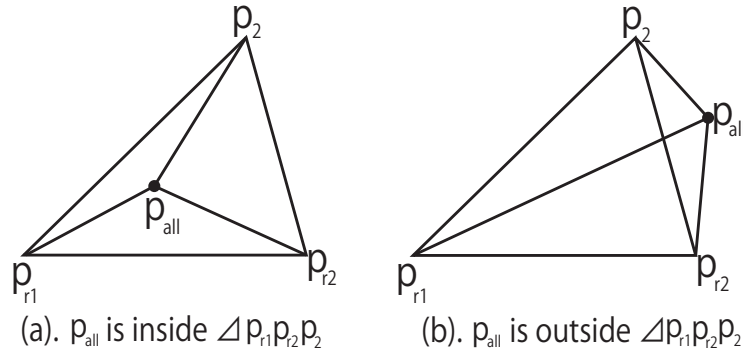


**Figure 4.4: The positional relationship between  $p_{all}$  and  $\triangle p_{r1}p_{r2}p_2$ .**

As illustrated in Figure 4.4, when the projection of  $\mathbf{P}_{all}$  can remain in the range of  $\triangle \mathbf{P}_{r1}\mathbf{P}_{r2}\mathbf{P}_2$  and we connect it to the three vertices of the triangle, three new triangles:  $\triangle \mathbf{p}_{r1}\mathbf{p}_2\mathbf{p}_{all}$ ,  $\triangle \mathbf{p}_{r2}\mathbf{p}_2\mathbf{p}_{all}$ , and  $\triangle \mathbf{p}_{r1}\mathbf{p}_{r2}\mathbf{p}_{all}$  are obtained. Here we define that the area of  $\triangle \mathbf{P}_{r1}\mathbf{P}_{r2}\mathbf{P}_2$ ,  $\triangle \mathbf{p}_{r1}\mathbf{p}_2\mathbf{p}_{all}$ ,  $\triangle \mathbf{p}_{r2}\mathbf{p}_2\mathbf{p}_{all}$ , and  $\triangle \mathbf{p}_{r1}\mathbf{p}_{r2}\mathbf{p}_{all}$  are  $S \triangle \mathbf{P}_{r1}\mathbf{P}_{r2}\mathbf{P}_2$ ,  $S \triangle \mathbf{p}_{r1}\mathbf{p}_2\mathbf{p}_{all}$ ,  $S \triangle \mathbf{p}_{r2}\mathbf{p}_2\mathbf{p}_{all}$ , and  $S \triangle \mathbf{p}_{r1}\mathbf{p}_{r2}\mathbf{p}_{all}$ . If  $\mathbf{p}_{all}$  can remain in  $\triangle \mathbf{P}_{r1}\mathbf{P}_{r2}\mathbf{P}_2$ , we obtain:

$$S \triangle \mathbf{P}_{r1}\mathbf{P}_{r2}\mathbf{P}_2 = S \triangle \mathbf{p}_{r1}\mathbf{p}_2\mathbf{p}_{all} + S \triangle \mathbf{p}_{r2}\mathbf{p}_2\mathbf{p}_{all} + S \triangle \mathbf{p}_{r1}\mathbf{p}_{r2}\mathbf{p}_{all} \quad (4.24)$$

Therefore from equation (4.24) we can determine whether  $\mathbf{p}_{all}$  remains inside or outside  $\triangle \mathbf{P}_{r1}\mathbf{P}_{r2}\mathbf{P}_2$ , and we can also determine whether the entire device can maintain its horizontal posture without tilting. As for where the  $\mathbf{p}_{all}$  in the triangle can make the device the most stable, we consider it as one of the study in the future.

### 4.3 Numerical analysis and theoretical value

Table 4.1 presents the properties of items in the entire system. For an arbitrary slope, the possibility of landing can be determined from equation (4.18) and (4.24). By

**Table 4.1: Properties of items of the entire perching system.**

Mass [kg]	$m_1$	0.240
	$m_2$	0.240
	$m_3$	0.880
	$m_4$	0.086
Length [mm]	$L$	205.000
	$l$	300.000
	$l_1$	150.000
	$l_2$	150.000
	$s$	60.000
	$t$	40.000
	$v$	150.000
	$w$	150.000
Angle [deg]	$\phi$	62.000
	$\theta_{1min}$	135.000
	$\theta_{1max}$	270.000
	$\theta_{2min}$	0.000
	$\theta_{2max}$	180.000

changing  $\alpha$  and  $\beta$ , and using equation (4.18) and (4.24), the range of  $\alpha$  and  $\beta$  on the slope that can be landed is obtained and it is summarized in Figure 4.5.

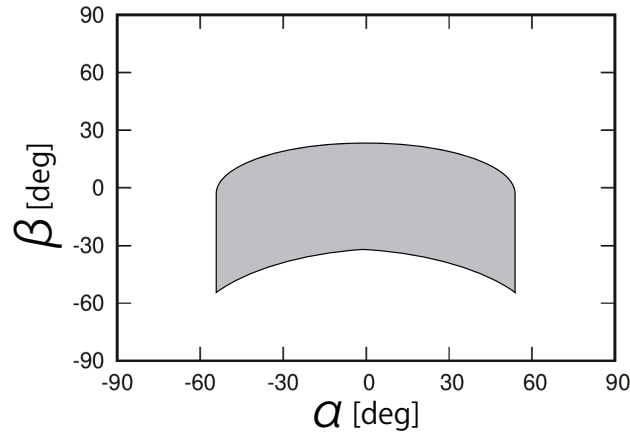
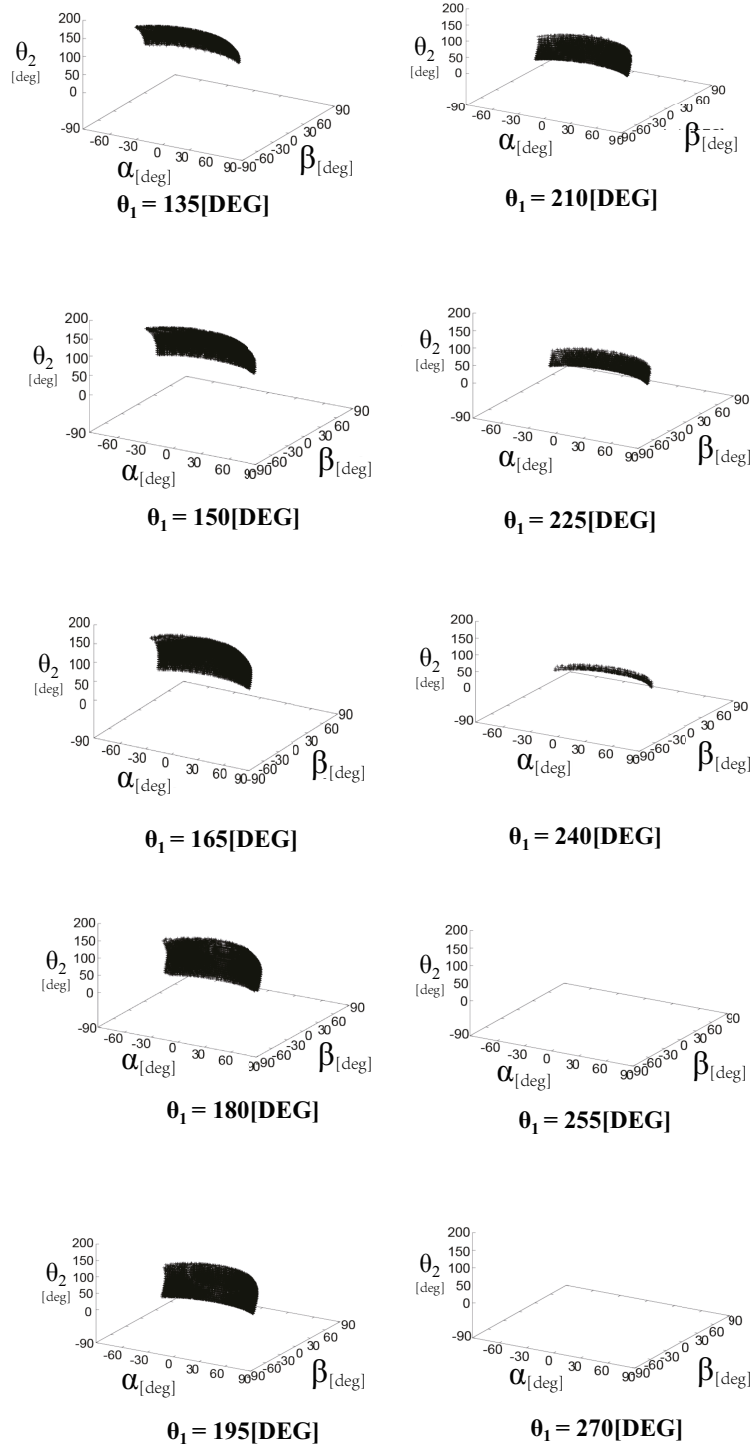
**Figure 4.5: Range of  $\alpha$  and  $\beta$  under landable conditions.**

Figure 4.5 illustrates the feasible range of the inclination angles  $\alpha$  and  $\beta$ . The range of  $\alpha$  is less than  $\pm 60$ [deg], the maximum value of  $\beta$  is approximately  $20$ [deg] and the minimum value is approximately  $-60$ [deg]. Furthermore, the relationship of the inclination angle  $\alpha$ ,  $\beta$  and  $\theta_1$ ,  $\theta_2$  when landing is achievable is summarized in Figure 4.6. In Figure 4.6, the value of  $\theta_1$  is listed from  $135$ [deg] to  $270$ [deg], with an interval of  $15$ [deg].



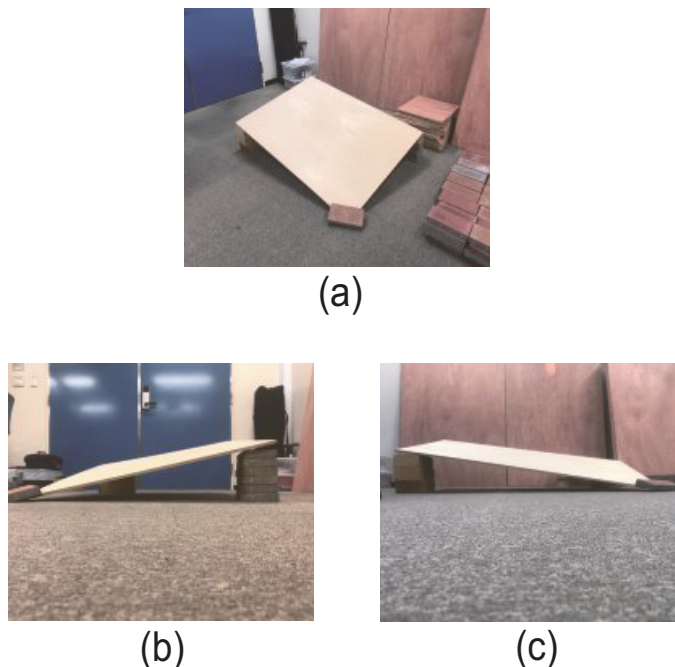
**Figure 4.6: The relationship of the inclination angle  $\alpha, \beta$  and the angle of robot arm  $\theta_1, \theta_2$  when landing is achievable.**

## 4.4 Experiment

The aim of the experiment is to verify that by changing the angle of links and other conditions in actual environment, the entire device can maintain its horizontal posture within the range concluded in the previous sections. By evaluating the performance of the proposed device while landing on a slope with different inclination angles, we aim to verify the consistency of actual experimental and theoretical result.

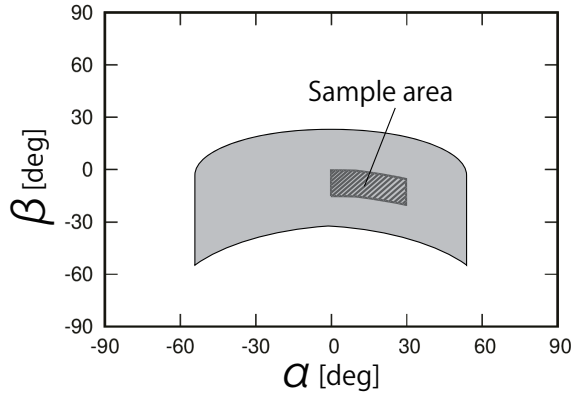
### 4.4.1 Experimental environment

Figure 4.7 illustrates the experimental environment. We chose a board with the length of 1200 mm and width of 850 mm as the slope for the experiment. Several bricks were utilized to support the board at its four corners. By increasing or decreasing the number of bricks needed to alter the supported height of the board, and different inclination angles  $\alpha$  and  $\beta$  were obtained.



**Figure 4.7: The Experimental environment. (a). is the overview of the experimental environment.(b). and (c). are the view from x and y direction of the environment respectively.**

### 4.4.2 Experimental result of arbitrary area



**Figure 4.8: The selected sample area for experiment.**

It is difficult to conduct the experiment of the entire range illustrated in Figure 4.5, because there are too many combinations of  $\alpha$  and  $\beta$ . Therefore, we consider that  $\theta_1$  is a constant of 180[deg]. The calculation of the range for available landing is summarized, and the experiment is conducted in that range. The range for experiment is illustrated in Figure 4.8. Simultaneously, the range of  $\alpha$  is approximately 0 to 30[deg], and the range of  $\beta$  is 2 to -18[deg]. Then we set  $\alpha$  to 0[deg], 10[deg], 20[deg] and 30[deg], and converted  $\beta$  from 2[deg] to -18[deg] in 2[deg] increments to verify whether landing was possible. The result of the verification is illustrated from Figure 4.9 to Figure 4.12, and for all cases can achieve stable landing is shown.

<b><math>\alpha = 0</math> [deg]</b>								
		$\beta = 0$	$\beta = -2$	$\beta = -4$	$\beta = -6$	$\beta = -8$	$\beta = -10$	$\beta = -12$
Cases	$\beta$ [deg]							
For $\theta_2 < 90$ [deg]								
		$\theta_2 = 70$ [deg]	$\theta_2 = 65$ [deg]	$\theta_2 = 50$ [deg]	$\theta_2 = 40$ [deg]	$\theta_2 = 30$ [deg]	$\theta_2 = 20$ [deg]	$\theta_2 = 10$ [deg]
For $\theta_2 \geq 90$ [deg]								
			$\theta_2 = 110$ [deg]	$\theta_2 = 115$ [deg]	$\theta_2 = 120$ [deg]			

**Figure 4.9: Landing situation when  $\alpha$  is equal to 0[deg].**

$\alpha = 10$ [deg]								
Cases \ $\beta$ [deg]	$\beta = 0$	$\beta = -2$	$\beta = -4$	$\beta = -6$	$\beta = -8$	$\beta = -10$	$\beta = -12$	
For $\theta_2 < 90$ [deg]								
	$\theta_2 = 75$ [deg]	$\theta_2 = 65$ [deg]	$\theta_2 = 49$ [deg]	$\theta_2 = 40$ [deg]	$\theta_2 = 30$ [deg]	$\theta_2 = 20$ [deg]	$\theta_2 = 15$ [deg]	
For $\theta_2 \geq 90$ [deg]								
		$\theta_2 = 105$ [deg]	$\theta_2 = 110$ [deg]	$\theta_2 = 120$ [deg]	$\theta_2 = 125$ [deg]	$\theta_2 = 130$ [deg]		

Figure 4.10: Landing situation when  $\alpha$  is equal to 10[deg].

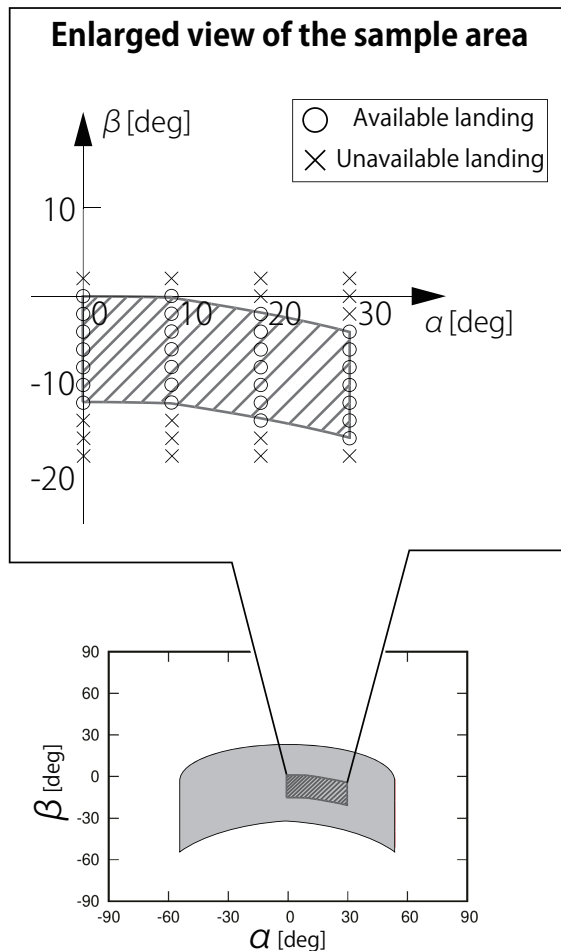
$\alpha = 20$ [deg]								
Cases \ $\beta$ [deg]	$\beta = -2$	$\beta = -4$	$\beta = -6$	$\beta = -8$	$\beta = -10$	$\beta = -12$	$\beta = -14$	
For $\theta_2 < 90$ [deg]								
	$\theta_2 = 80$ [deg]	$\theta_2 = 55$ [deg]	$\theta_2 = 45$ [deg]	$\theta_2 = 35$ [deg]	$\theta_2 = 25$ [deg]	$\theta_2 = 15$ [deg]	$\theta_2 = 10$ [deg]	
For $\theta_2 \geq 90$ [deg]								
	$\theta_2 = 100$ [deg]	$\theta_2 = 110$ [deg]	$\theta_2 = 115$ [deg]	$\theta_2 = 120$ [deg]	$\theta_2 = 125$ [deg]			

Figure 4.11: Landing situation when  $\alpha$  is equal to 20[deg].

$\alpha = 30$ [deg]								
Cases \ $\beta$ [deg]	$\beta = -4$	$\beta = -6$	$\beta = -8$	$\beta = -10$	$\beta = -12$	$\beta = -14$	$\beta = -16$	
For $\theta_2 < 90$ [deg]								
	$\theta_2 = 80$ [deg]	$\theta_2 = 60$ [deg]	$\theta_2 = 45$ [deg]	$\theta_2 = 35$ [deg]	$\theta_2 = 25$ [deg]	$\theta_2 = 20$ [deg]	$\theta_2 = 15$ [deg]	
For $\theta_2 \geq 90$ [deg]								
		$\theta_2 = 105$ [deg]	$\theta_2 = 115$ [deg]	$\theta_2 = 125$ [deg]	$\theta_2 = 130$ [deg]	$\theta_2 = 140$ [deg]		

Figure 4.12: Landing situation when  $\alpha$  is equal to 30[deg].

Figure 4.13 illustrates an enlarged view of the landing range in Figure 4.8. In Figure 4.13, the pattern in hollow circle ( $\circ$ ) implies the cases that stable landing can be achieved, and the pattern in cross ( $\times$ ) implies the cases of unavailable landing. The landing range and the experimental results are similar. This means that it is possible to determine whether landing is possible or not, by the method presented in the previous sections.



**Figure 4.13:** The enlarged view of the sample area's landing range illustrated in Figure 4.8.

#### 4.4.3 Experimental result of area near the border

As shown in Figure 4.14, to make the analysis and conclusions more convincing, the experiment for the area near the border in Figure 4.5 is also conducted. Because the range of  $\alpha$  and  $\beta$  for available landing in Figure 4.5 is a symmetrical arc area, we take the

highest and lowest points on the leftmost side of the range for the verification experiment. The point on the upper left is defined as point A and the point on the bottom left is defined as point B. The coordinates of point A and B are (-53, -6) and (-53, -50) respectively, and an experimental snap shot is shown in Figure 17.

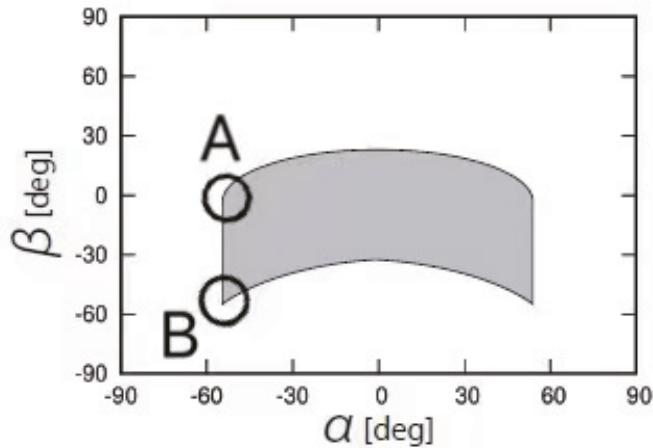


**Figure 4.14: The selected points near the border for experiment.**

Figure 4.15 shows that the device can maintain its horizontal state in the case when the inclination angles are at the point A and B positions. When in the point A coordinate position, the device can maintain its stable state only when the angles of  $\theta_1$  and  $\theta_2$  are  $220^\circ$  and  $20^\circ$  respectively, and also, when in the point B coordinate position, the device can maintain its stable state only when the angles of  $\theta_1$  and  $\theta_2$  are  $140^\circ$  and  $165^\circ$ , respectively.

## Discussion

Analysis of the landing conditions implicated that the feasible range for multicopter landing, and theoretically, we can determine the possibility of landing on a plane with different inclination angles according to the proposed judgment method. However, the analysis at this stage still has some insufficient. One of the limitation is that although the wooden board are utilized to simulate inclined plane in our experiment for simplicity, the actual environment, especially after a disaster, is often much more complicated, and its

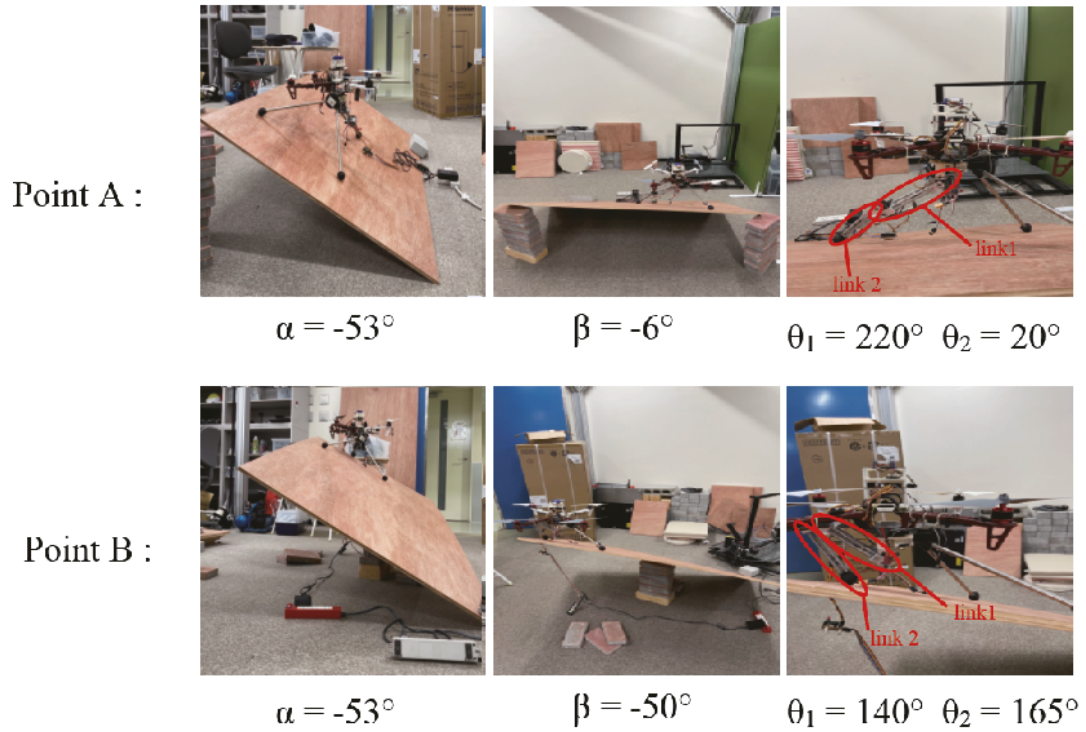


**Figure 4.15: Experiment of the area near the border in Figure 4.5.**

analysis is considered to be improved.

Based on the results of the theoretical and experimental values, the error in analysis is also considered. In this study, two reasons are considered to be the factor of such errors: (1) First is the error in judgment of the COG. Each part of the multicopters COG can be analyzed by hanging, (Plumb Line Technique) and this may cause the error when calculating the COG of the entire device, and also affect determining the available landing; (2) The second possible error is in angle measurement. Although the skid and arm are considered as a single link in static model analysis, they are structures with thickness. When conducting experiments, we measure the angular relationship based on the central axis of these links, which may lead to a few slight errors.

Additionally, the analysis of the contact point to the landing plane is also considered. Although for the same slope, there are many contact points that can make the device landing smoothly, there is an optimal location of the  $P_{all}$  and the contact point. As shown in Figure 4.16, if we define three sides of the triangle  $P_2P_{r1}P_{r2}$  are  $a$ ,  $b$  and  $c$ . Then the

distant between the projection of  $P_{all}$  and those three sides, are defined as  $l_a$ ,  $l_b$ , and  $l_c$ . If the shortest distant of  $l_a$ ,  $l_b$ , and  $l_c$  can be as long as possible, the stability of the device in this case can be considered as the best. As for the location of the contact point under different conditions, when the entire device is the most stable, it is considered as one of the future work.

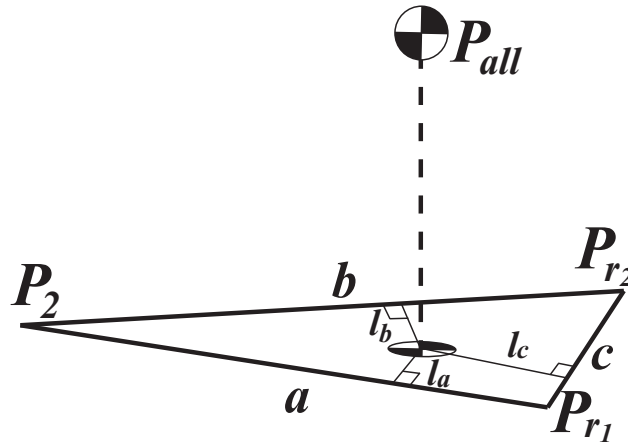


**Figure 4.16:** Explanation for the optimal location of the  $P_{all}$  and the contact point.

## 4.5 Concluding Remark

In this study, we proposed a method to determine whether or not the skid-carried multicopter can land on an uneven ground. The slope range where the multicopter can land is concluded, and the accuracy of the analysis is demonstrated by the verification experiment. However, some weaknesses and improvements also need to be considered in our study. For example, to simplify the analysis, we simulated the uneven ground with slopes with different inclination angles, and this may not a perfect explanation of the correspondence between the device and the rough terrain. Therefore, in the next stage, we consider utilizing an environment with obstacles to simulate uneven ground to make the research closer to reality.

In addition, when considering the coefficient of friction, we solely selected rubber and wood as research objects, and this may cause several study limitations. Thus, in the

future, we plan to analyze the possibility of landing, when the surface of the slope is made of other materials. We also planned to explore how the length will affect the experimental results. If the possibility of landing can be controlled by changing the link length, it would be a very interesting and meaningful study. In addition, we anticipate improving the procedure of the flight controller, and achieving outdoor landings.

## Chapter 5

### Conclusion

In this study, first, I focused on the analysis of an underactuated parallel-link gripper for a multicopter capable of plane perching. As the initial step, the static model is established and all the forces and torque are considered to be analyzed. On the latter, for different cases, including the target with different thicknesses and perching with different embedded depths, are considered, and summarized by classified discussion. Based on the friction cone theory, the feasible condition and range for multicopter capable of plane perching is concluded. Although it is difficult to verify all the cases, one of the situation, which contains the most cases, is regarded as the most suitable situation for conducting the experiment. Finally, the conclusion is demonstrated by comparing the theoretical and experimental values.

Second, I developed a passive skid for multicopter landing on rough terrain. This proposed skid can be considered as a three-legged mechanism, which consisting of a passive joint and two feet. As the most important feature and the embodiment of its innovation, the proposed skid is completely composed of a mechanical structure without any electric-actuated drives, and the analysis of the range of slopes for multicopter available landing is conducted. The frictional torque of the passive joint is also considered in this study, and the determination of whether the multicopter can remain its horizontal state, is concluded. For verification, three experiments are designed to demonstrate the correctness of the theory and analysis in this study. Further, I proposed a extended study based on the passive skid, and concentrated on the influence of different postures of robot arm on possibility of rough terrain landing. Thus, in this extended study, the static model is

reconstructed and by analyzing that the projection of the entire device's COG is inside or outside the triangle comprises the contact points between the device and the rough terrain, whether the device can land successfully can be determined. In this studies involved multicopter landing, to simplify the analysis, the rough terrain is simulated by slopes with different inclination angles and this may lead to some limitations. Thus, in the future, we will consider the use of complex environments for simulating the rough terrain to make our study more persuasive.

## Bibliography

- [1] X. Yang, L. Jiang, X. Tang and X. Ren, “ An improved PCA-SIFT algorithm application in light small UAV image registration,” 2017 Progress In Electromagnetics Research Symposium - Spring (PIERS), 2017, pp. 2554-2558.
- [2] P. B. Quater, F. Grimaccia, S. Leva, M. Mussetta and M. Aghaei, “ Light Unmanned Aerial Vehicles (UAVs) for Cooperative Inspection of PV Plants,” in IEEE Journal of Photovoltaics, vol. 4, no. 4, pp. 1107-1113, July 2014.
- [3] A. Tariq, S. M. Osama and A. Gillani, “ Development of a Low Cost and Light Weight UAV for Photogrammetry and Precision Land Mapping Using Aerial Imagery,” 2016 International Conference on Frontiers of Information Technology (FIT), 2016.
- [4] L. Luo and R. Chai, “Cost-efficient UAV Deployment for Content Fetching in Cellular D2D Systems,” 2020 IEEE 92nd Vehicular Technology Conference (VTC2020-Fall), 2020, pp. 1-5
- [5] D. Costantino, M. G. Angelini and G. Vozza, “ The engineering and assembly of a low cost UAV,” 2015 IEEE Metrology for Aerospace (MetroAeroSpace), 2015, pp. 351-355.
- [6] P. Sedlak, J. Komarkova, O. Macin and J. Jech, “ The Procedure for Processing Images from a Low-cost UAV,” 2019 14th Iberian Conference on Information Systems and Technologies (CISTI), 2019, pp. 1-4.
- [7] E. P. Flynn, “ Low-cost approaches to UAV design using advanced manufacturing

- techniques,” 2013 IEEE Integrated STEM Education Conference (ISEC), 2013, pp. 1-4.
- [8] J. Liu, W. Wang, T. Wang, Z. Shu and X. Li, “ A Motif-Based Rescue Mission Planning Method for UAV Swarms Usingan Improved PICEA,” in IEEE Access, vol. 6, pp. 40778-40791, 2018.
- [9] S. Charalampidou, E. Lygouras, I. Dokas, A. Gasteratos and A. Zacharopoulou, “ A Sociotechnical Approach to UAV Safety for Search and Rescue Missions,” 2020 International Conference on Unmanned Aircraft Systems (ICUAS), 2020, pp. 1416-1424.
- [10] Y. Naidoo, R. Stopforth and G. Bright, “ Development of an UAV for search & rescue applications,” IEEE Africon ’11, 2011, pp. 1-6.
- [11] H. Surmann et al., “ Integration of UAVs in Urban Search and Rescue Missions,” 2019 IEEE International Symposium on Safety, Security, and Rescue Robotics (SSRR), 2019, pp. 203-209.
- [12] E. T. Alotaibi, S. S. Alqefari and A. Koubaa, “ LSAR: Multi-UAV Collaboration for Search and Rescue Missions,” in IEEE Access, vol. 7, pp. 55817-55832, 2019.
- [13] T. Tao and R. Jia, “ UAV decision-making for maritime rescue based on Bayesian Network,” Proceedings of 2012 2nd International Conference on Computer Science and Network Technology, 2012, pp. 2068-2071.
- [14] A. Valsan, P. B., V. D. G. H., R. S. Unnikrishnan, P. K. Reddy and V. A., “Unmanned Aerial Vehicle for Search and Rescue Mission,” 2020 4th International Conference on Trends in Electronics and Informatics (ICOEI)(48184), 2020, pp. 684-687.
- [15] P. Silberberg and R. C. Leishman, “ Aircraft Inspection by Multirotor UAV Using Coverage Path Planning,” 2021 International Conference on Unmanned Aircraft Systems (ICUAS), 2021, pp. 575-581.

- [16] F. Ge, K. Li, W. Xu and Y. Wang, "Path Planning of UAV for Oilfield Inspection Based on Improved Grey Wolf Optimization Algorithm," 2019 Chinese Control And Decision Conference (CCDC), 2019, pp. 3666-3671.
- [17] Q. Wang, H. Xiong and B. Qiu, "The Attitude Control of Transmission Line Fault Inspection UAV Based on ADRC," 2017 International Conference on Industrial Informatics - Computing Technology, Intelligent Technology, Industrial Information Integration (ICIICII), 2017, pp. 186-189.
- [18] M. Perreault and K. Behdinan, "Delivery Drone Driving Cycle," in *IEEE Transactions on Vehicular Technology*, vol. 70, no. 2, pp. 1146-1156, Feb. 2021.
- [19] P. Sanjana and M. Prathilothamai, "Drone Design for First Aid Kit Delivery in Emergency Situation," 2020 6th International Conference on Advanced Computing and Communication Systems (ICACCS), 2020, pp. 215-220.
- [20] K. Feng, W. Li, S. Ge and F. Pan, "Packages delivery based on marker detection for UAVs," 2020 Chinese Control And Decision Conference (CCDC), 2020, pp. 2094-2099.
- [21] H. D. Yoo and S. M. Chankov, "Drone-delivery Using Autonomous Mobility: An Innovative Approach to Future Last-mile Delivery Problems," 2018 IEEE International Conference on Industrial Engineering and Engineering Management (IEEM), 2018, pp. 1216-1220.
- [22] C. E. Lin and S. -K. Yang, "Camera gimbal tracking from UAV flight control," 2014 CACS International Automatic Control Conference (CACS 2014), 2014, pp. 319-322.
- [23] X. Li and L. Yang, "Design and Implementation of UAV Intelligent Aerial Photography System," 2012 4th International Conference on Intelligent Human-Machine Systems and Cybernetics, 2012, pp. 200-203.

- [24] I. Yurchuk, V. Kovdrya and L. Bilyanska, "Segmentation of Digital Images of Aerial Photography," 2019 IEEE 5th International Conference Actual Problems of Unmanned Aerial Vehicles Developments (APUAVD), 2019, pp. 258-261.
- [25] Z. Haifeng, W. Huabo, W. Min, Z. Huizhu and L. Yu, "A Vision Based UAV Pesticide Mission System," 2018 IEEE CSAA Guidance, Navigation and Control Conference (CGNCC), 2018, pp. 1-6.
- [26] F. Ay and G. Ince, "Application of pesticide using unmanned aerial vehicle," 2015 23rd Signal Processing and Communications Applications Conference (SIU), 2015, pp. 1268-1271.
- [27] V. P. Subba Rao and G. S. Rao, "Design and Modelling of an Affordable UAV Based Pesticide Sprayer in Agriculture Applications," 2019 Fifth International Conference on Electrical Energy Systems (ICEES), 2019, pp. 1-4.
- [28] P. Lottes, R. Khanna, J. Pfeifer, R. Siegwart and C. Stachniss, "UAV-based crop and weed classification for smart farming," 2017 IEEE International Conference on Robotics and Automation (ICRA), 2017, pp. 3024-3031.
- [29] J. Dong, K. Ota and M. Dong, "UAV-Based Real-Time Survivor Detection System in Post-Disaster Search and Rescue Operations," in IEEE Journal on Miniaturization for Air and Space Systems, vol. 2, no. 4, pp. 209-219, Dec. 2021.
- [30] J. Q. Cui et al., "Drones for cooperative search and rescue in post-disaster situation," 2015 IEEE 7th International Conference on Cybernetics and Intelligent Systems (CIS) and IEEE Conference on Robotics, Automation and Mechatronics (RAM), 2015, pp. 167-174.
- [31] Z. He, Y. Lu and M. Zheng, "Simulation and analysis of perching maneuvers for morphing UAVs," Proceedings of the 33rd Chinese Control Conference, 2014, pp. 6769-6774.
- [32] X. Ye, Y. Liu and C. Huang, "Modeling and Control Based on a Force Observer for a Flying-Perching Quadrotor," 2018 IEEE 8th Annual International Conference

- on CYBER Technology in Automation, Control, and Intelligent Systems (CYBER), 2018, pp. 758-763.
- [33] J. W. Roberts, R. Cory and R. Tedrake, "On the controllability of fixed-wing perching," 2009 American Control Conference, 2009, pp. 2018-2023.
- [34] H. Jiang et al., "Modeling the dynamics of perching with opposed-grip mechanisms," 2014 IEEE International Conference on Robotics and Automation (ICRA), 2014, pp. 3102-3108.
- [35] C. Luo, L. Yu and P. Ren, "A Vision-Aided Approach to Perching a Bioinspired Unmanned Aerial Vehicle," in IEEE Transactions on Industrial Electronics, vol. 65, no. 5, pp. 3976-3984, May 2018.
- [36] P. F. Wang, Y. F. Zhang, H. L. Qin, F. Lin and S. H. Teo, "Offline perching location selection for quadrotor UAV in urban environment," 2016 12th IEEE International Conference on Control and Automation (ICCA), 2016, pp. 1008-1013.
- [37] V. Perez-Sanchez, A. E. Gomez-Tamm, F. J. Garcia-Rubiales, B. Arrue and A. Ollero, "Analysis of Forces Involved in the Perching Maneuver of Flapping-Wing Aerial Systems and Development of an Ultra-Lightweight Perching System," 2021 International Conference on Unmanned Aircraft Systems (ICUAS), 2021, pp. 1284-1290.
- [38] S. Backus, J. Izraelevitz, J. Quan, R. Jitosh, E. Slavick and A. Kalantari, "Design and Testing of an Ultra-Light Weight Perching System for Sloped or Vertical Rough Surfaces on Mars," 2020 IEEE Aerospace Conference, 2020, pp. 1-12.
- [39] J. Yoo, I. Park, V. To, J. Q. H. Lum and T. Smith, "Avionics and perching systems of free-flying robots for the International Space Station," 2015 IEEE International Symposium on Systems Engineering (ISSE), 2015, pp. 198-201.
- [40] F. J. Garcia-Rubiales, P. Ramon-Soria, B. C. Arrue and A. Ollero, "Magnetic detaching system for Modular UAVs with perching capabilities in industrial environ-

- ments,” 2019 Workshop on Research, Education and Development of Unmanned Aerial Systems (RED UAS), 2019, pp. 172-176.
- [41] J. Moore and R. Tedrake, “Control synthesis and verification for a perching UAV using LQR-Trees,” 2012 IEEE 51st IEEE Conference on Decision and Control (CDC), 2012, pp. 3707-3714.
- [42] K. M. Popek et al., “Autonomous Grasping Robotic Aerial System for Perching (AGRASP),” 2018 IEEE/RSJ International Conference on Intelligent Robots and Systems (IROS), 2018, pp. 1-9.
- [43] K. Zhang, P. Chermprayong, T. M. Alhinai, R. Siddall and M. Kovac, “SpiderMAV: Perching and stabilizing micro aerial vehicles with bio-inspired tensile anchoring systems,” 2017 IEEE/RSJ International Conference on Intelligent Robots and Systems (IROS), 2017, pp. 6849-6854.
- [44] J. W. Yeol, “Design and operation of a small unmanned aerial vehicle with multiple tentacles,” 2015 IEEE International Conference on Robotics and Biomimetics (ROBIO), 2015, pp. 1877-1881.
- [45] J. W. Yeol, D. Toohey and P. Harrigan, “Design and analysis of a mechanical tentacle system for mobile manipulation of small unmanned aerial vehicles,” 2016 13th International Conference on Ubiquitous Robots and Ambient Intelligence (URAI), 2016, pp. 459-460.
- [46] P. Singh, S. Gupta, L. Behera, N. K. Verma and S. Nahavandi, “Perching of Nano-Quadrotor Using Self-Trigger Finite-Time Second-Order Continuous Control,” in *IEEE Systems Journal*, vol. 15, no. 4, pp. 4989-4999, Dec. 2021.
- [47] P. Yu, G. Chamitoff and K. C. Wong, “Perching Upside Down with Bi-directional Thrust Quadrotor,” 2020 International Conference on Unmanned Aircraft Systems (ICUAS), 2020, pp. 1697-1703.
- [48] F. J. Maldonado, J. A. Acosta, J. Tormo-Barbero, P. Grau, M. M. Guzman and A. Ollero, “Adaptive Nonlinear Control For Perching of a Bioinspired Ornithopter,”

- 2020 IEEE/RSJ International Conference on Intelligent Robots and Systems (IROS), 2020, pp. 1385-1390.
- [49] A. Kalantari, K. Mahajan, D. Ruffatto and M. Spenko, “ Autonomous perching and take-off on vertical walls for a quadrotor micro air vehicle,” 2015 IEEE International Conference on Robotics and Automation (ICRA), 2015, pp. 4669-4674.
- [50] A. A. Paranjape, S. Chung and J. Kim, “ Novel Dihedral-Based Control of Flapping-Wing Aircraft With Application to Perching,” in IEEE Transactions on Robotics, vol. 29, no. 5, pp. 1071-1084, Oct. 2013.
- [51] T. Nishio, M. Zhao, T. Anzai, K. Kojima, K. Okada and M. Inaba, “Fixed-root Aerial Manipulator: Design, Modeling, and Control of Multilink Aerial Arm to Adhere Foot Module to Ceilings using Rotor Thrust,” 2021 IEEE International Conference on Robotics and Automation (ICRA), 2021, pp. 283-289.
- [52] M. Orsag, C. Korpela, S. Bogdan and P. Oh, “ Dexterous Aerial Robots-Mobile Manipulation Using Unmanned Aerial Systems,” in IEEE Transactions on Robotics, vol. 33, no. 6, pp. 1453-1466, Dec. 2017.
- [53] W. Chi, K. H. Low, K. H. Hoon and J. Tang, “ An optimized perching mechanism for autonomous perching with a quadrotor,” 2014 IEEE International Conference on Robotics and Automation (ICRA), 2014, pp. 3109-3115.
- [54] H. Zhang, J. Sun and J. Zhao, “ Compliant Bistable Gripper for Aerial Perching and Grasping,” 2019 International Conference on Robotics and Automation (ICRA), 2019, pp. 1248-1253.
- [55] H. Nguyen, R. Siddall, B. Stephens, A. Navarro-Rubio and M. Kovac, “ A Passively Adaptive Microspine Grapple for Robust, Controllable Perching,” 2019 2nd IEEE International Conference on Soft Robotics (RoboSoft), 2019, pp. 80-87.
- [56] K. Tanaka and M. Spenko, “ A Gecko-Like/Electrostatic Gripper for Free-Flying Perching Robots,” 2020 IEEE Aerospace Conference, 2020, pp. 1-7.

- [57] A. E. Gomez-Tamm, V. Perez-Sanchez, B. C. Arrue and A. Ollero, “SMA Actuated Low-Weight Bio-Inspired Claws for Grasping and Perching Using Flapping Wing Aerial Systems,” 2020 IEEE/RSJ International Conference on Intelligent Robots and Systems (IROS), 2020, pp. 8807-8814.
- [58] T. Lin, S. Long and K. A. Stol, “Automated Perching of a Multirotor UAV atop Round Timber Posts,” 2018 IEEE/ASME International Conference on Advanced Intelligent Mechatronics (AIM), 2018, pp. 486-491.
- [59] S. B. Backus, L. U. Odhner and A. M. Dollar, “Design of hands for aerial manipulation: Actuator number and routing for grasping and perching,” 2014 IEEE/RSJ International Conference on Intelligent Robots and Systems, 2014, pp. 34-40.
- [60] A. McLaren, Z. Fitzgerald, G. Gao and M. Liarokapis, “A Passive Closing, Tendon Driven, Adaptive Robot Hand for Ultra-Fast, Aerial Grasping and Perching,” 2019 IEEE/RSJ International Conference on Intelligent Robots and Systems (IROS), 2019, pp. 5602-5607.
- [61] M. A. Estrada, E. W. Hawkes, D. L. Christensen and M. R. Cutkosky, “Perching and vertical climbing: Design of a multimodal robot,” 2014 IEEE International Conference on Robotics and Automation (ICRA), 2014, pp. 4215-4221.
- [62] T. Sato, T. Kominami, H. Paul, R. Miyazaki, R. Ladig and K. Shimomura, “Passive Perching and Landing Mechanism for Multirotor Flying Robot,” 2021 IEEE/ASME International Conference on Advanced Intelligent Mechatronics (AIM), 2021, pp. 396-401.
- [63] Z. Wang, H. She and W. Si, “Autonomous landing of multi-rotors UAV with monocular gimbaled camera on moving vehicle,” 2017 13th IEEE International Conference on Control & Automation (ICCA), 2017, pp. 408-412.
- [64] Z. Gan, H. Xu, Y. He, W. Cao and G. Chen, “Autonomous Landing Point Retrieval Algorithm for UAVs Based on 3D Environment Perception,” 2021 IEEE 7th International Conference on Virtual Reality (ICVR), 2021, pp. 104-108.

- [65] Y. Jung, H. Bang and D. Lee, "Robust marker tracking algorithm for precise UAV vision-based autonomous landing," 2015 15th International Conference on Control, Automation and Systems (ICCAS), 2015, pp. 443-446.
- [66] S. Nazir, S. Aziz, Y. Khaliq and S. M. Adnan, "Vision Based Autonomous Runway Identification and Position Estimation for UAV Landing," 2018 International Conference on Artificial Intelligence and Data Processing (IDAP), 2018, pp. 1-6.
- [67] W. Rui, Z. Zhou and S. Yanhang, "Robust Landing Control and Simulation for Flying Wing UAV," 2007 Chinese Control Conference, 2007, pp. 600-604.
- [68] R. Liu et al., "Vision-guided autonomous landing of multirotor UAV on fixed landing marker," 2020 IEEE International Conference on Artificial Intelligence and Computer Applications (ICAICA), 2020, pp. 455-458.
- [69] U. Papa and G. Del Core, "Design of sonar sensor model for safe landing of an UAV," 2015 IEEE Metrology for Aerospace (MetroAeroSpace), 2015, pp. 346-350.
- [70] G. Ky, S. Alam and V. Duong, "Carousel Inspired Virtual Circulation: A Simulation Model for Uav Arrival and Landing Procedure under Random Events," 2020 Winter Simulation Conference (WSC), 2020, pp. 504-515.
- [71] Z. Wu et al., "Autonomous UAV Landing System Based on Visual Navigation," 2019 IEEE International Conference on Imaging Systems and Techniques (IST), 2019, pp. 1-6.
- [72] A. Miller, M. Shah and D. Harper, "Landing a UAV on a runway using image registration," 2008 IEEE International Conference on Robotics and Automation, 2008, pp. 182-187.
- [73] P. Marcon, J. Janousek and R. Kadlec, "Vision-Based and Differential Global Positioning System to Ensure Precise Autonomous Landing of UAVs," 2018 Progress in Electromagnetics Research Symposium (PIERS-Toyama), 2018, pp. 542-546.

- [74] J. -S. Liu and H. -C. Liu, "Visual Navigation for UAVs Landing on Accessory Building Floor," 2020 International Conference on Pervasive Artificial Intelligence (ICPAI), 2020, pp. 158-163.
- [75] M. Laiacker, K. Kondak, M. Schwarzbach and T. Muskardin, "Vision aided automatic landing system for fixed wing UAV," 2013 IEEE/RSJ International Conference on Intelligent Robots and Systems, 2013, pp. 2971-2976.
- [76] V. F. Vidal, L. M. Honorio, M. F. Santos, M. F. Silva, A. S. Cerqueira and E. J. Oliveira, "UAV vision aided positioning system for location and landing," 2017 18th International Carpathian Control Conference (ICCC), 2017, pp. 228-233.
- [77] A. E. Klochan, A. Al-Ammouri, M. M. Dekhtyar and N. M. Poleva, "Fundamentals of the Polarimetric UAV Landing System," 2019 IEEE 5th International Conference Actual Problems of Unmanned Aerial Vehicles Developments (APUAVD), 2019, pp. 153-156.
- [78] Y. Leng, J. Xiao and B. Leng, "Design of Monitoring Software of Take-Off and Landing for UAV," 2016 International Conference on Network and Information Systems for Computers (ICNISC), 2016, pp. 199-201.
- [79] A. Schanen, J. Dumon, N. Meslem and A. Hably, "Take-off and landing of an AWE system using a multicopter," 2020 American Control Conference (ACC), 2020, pp. 3846-3851.
- [80] W. Chu, H. Guo and W. Xing, "Design of non-similar dual-redundant electromechanical actuation system for UAV landing gear," 2016 IEEE International Conference on Aircraft Utility Systems (AUS), 2016, pp. 592-595.
- [81] D. Fujikura, K. Tadakuma, M. Watanabe, Y. Okada, K. Ohno and S. Tadokoro, "Toward Enabling a Hundred Drones to Land in a Minute," 2020 IEEE/RSJ International Conference on Intelligent Robots and Systems (IROS), 2020, pp. 1238-1245.

- [82] E. A. Voznesenskii, “Automated Battery Charging System for Multi-Rotor Aerial Vehicles,” 2021 Wave Electronics and its Application in Information and Telecommunication Systems (WECONF), 2021, pp. 1-4.
- [83] M. -F. R. Lee, S. K. and A. Jain, “Autonomous Pose Correction and Landing System for Unmanned Aerial Vehicles,” 2020 International Conference on Advanced Robotics and Intelligent Systems (ARIS), 2020, pp. 1-6.
- [84] X. Yang, L. Dong, W. Liaoni and S. Yangyang, “Design and implementation of twin-rotor tail-sitter UAV,” 2015 IEEE Advanced Information Technology, Electronic and Automation Control Conference (IAEAC), 2015, pp. 406-410
- [85] W. Myeong and H. Myung, “Development of a Wall-Climbing Drone Capable of Vertical Soft Landing Using a Tilt-Rotor Mechanism,” in IEEE Access, vol. 7, pp. 4868-4879, 2019.
- [86] S. Anbalagan, G. Raja, K. Kottursamy, G. S. Aparna, J. Kumaresan and M. Ihsan, “Authorized Arming and Safeguarded Landing Mechanisms for Drones,” 2020 IEEE Globecom Workshops (GC Wkshps, 2020, pp. 1-6.
- [87] K. Nagarjuna and G. R. Suresh, “Design of effective landing mechanism for fully autonomous Unmanned Aerial Vehicle,” 2015 3rd International Conference on Signal Processing, Communication and Networking (ICSCN), 2015, pp. 1-6.
- [88] <https://dictionary.cambridge.org/dictionary/english/perch?q=perching>
- [89] <https://dictionary.cambridge.org/dictionary/english/landing>
- [90] A. Patrik et al., “GNSS-based navigation systems of autonomous drone for delivering items,” J. Big Data, vol. 6, no. 1, 2019.
- [91] K. Appeaning Addo, P. N. Jayson-Quashigah, S. N. A. Codjoe, and F. Martey, “Drone as a tool for coastal flood monitoring in the Volta Delta, Ghana,” *Geoenvironmental Disasters*, vol. 5, no. 1, 2018.

- [92] C. Gomez and H. Purdie, "UAV-based Photogrammetry and Geocomputing for Hazards and Disaster Risk Monitoring-A Review," *Geoenvironmental Disasters*, vol. 3, no. 1, 2016.
- [93] Yoshinori Ohnishi, Takeshi Takaki, Tadayoshi Aoyama, and Idaku Ishii Development of a 4-Joint 3-DOF Robotic Arm with Anti-reaction Force Mechanism for a Multicopter, *Proceedings of 2017 IEEE/RSJ International Conference on Intelligent Robots and Systems*, pp.985-991, 2017.
- [94] <https://www.poladrone.com/drone-delivery-advantages-and-challenges/>
- [95] [https://www.dhl.de/content/dam/dhlde/images/ueber\\_uns/content/dhl\\_trend\\_report\\_uav.pdf](https://www.dhl.de/content/dam/dhlde/images/ueber_uns/content/dhl_trend_report_uav.pdf)
- [96] R. Kitchen et al., "Design and Evaluation of a Perching Hexacopter Drone for Energy Harvesting from Power Lines," *2020 IEEE/RSJ International Conference on Intelligent Robots and Systems (IROS)*, 2020, pp. 1192-1198.
- [97] M. Chang, Y. Sun, J. Bai and L. Xiao, "Principles on Longitudinal Perching Dynamics of Fixed-Wing Flying Robots," *2019 4th International Conference on Robotics and Automation Engineering (ICRAE)*, 2019, pp. 191-195.
- [98] Z. Zhang, P. Xie and O. Ma, "Bio-inspired trajectory generation for UAV perching," *2013 IEEE/ASME International Conference on Advanced Intelligent Mechatronics*, 2013, pp. 997-1002.
- [99] <https://journals.sagepub.com/doi/10.5772/58898>
- [100] R. Spica, A. Franchi, G. Oriolo, H. H. Bulthoff and P. R. Giordano, "Aerial grasping of a moving target with a quadrotor UAV," *2012 IEEE/RSJ International Conference on Intelligent Robots and Systems*, 2012, pp. 4985-4992.
- [101] J. D. Crisman, C. Kanojia and I. Zeid, "Graspar: a flexible, easily controllable robotic hand," in *IEEE Robotics & Automation Magazine*, vol. 3, no. 2, pp. 32-38, June 1996

- [102] H. Zhang, E. Lerner, B. Cheng, and J. Zhao, "Compliant Bistable Grippers Enable Passive Perching for Micro Aerial Vehicles," *IEEE/ASME Trans. Mechatronics*, vol. 26, no. 5, pp. 2316-2326, 2021.
- [103] H. Zhang, E. Lerner, B. Cheng and J. Zhao, "Compliant Bistable Grippers Enable Passive Perching for Micro Aerial Vehicles," in *IEEE/ASME Transactions on Mechatronics*, vol. 26, no. 5, pp. 2316-2326, Oct. 2021.
- [104] B. Almasri and F. B. Ouezdou, "New Design of One Motor Driven Under Actuated Humanoid Hand," 2007 *IEEE/RSJ International Conference on Intelligent Robots and Systems*, 2007, pp. 1491-1496.
- [105] B. Massa, S. Roccella, M. C. Carrozza and P. Dario, "Design and development of an underactuated prosthetic hand," *Proceedings 2002 IEEE International Conference on Robotics and Automation (Cat. No.02CH37292)*, 2002, pp. 3374-3379 vol.4.
- [106] A. Nagendran, W. Crowther and R. Richardson, "Biologically inspired legs for UAV perched landing," in *IEEE Aerospace and Electronic Systems Magazine*, vol. 27, no. 2, pp. 4-13, Feb. 2012.
- [107] W. Chi, K. H. Low, K. H. Hoon, J. Tang, and T. H. Go, "A bio-inspired adaptive perching mechanism for unmanned Aerial Vehicles," *J. Robot. Mechatronics*, vol. 24, no. 4, pp. 642-648, 2012.
- [108] L. Daler, A. Klaptocz, A. Briod, M. Sitti and D. Floreano, "A perching mechanism for flying robots using a fibre-based adhesive," 2013 *IEEE International Conference on Robotics and Automation*, 2013, pp. 4433-4438.
- [109] S. Liu, W. Dong, Z. Ma and X. Sheng, "Adaptive Aerial Grasping and Perching With Dual Elasticity Combined Suction Cup," in *IEEE Robotics and Automation Letters*, vol. 5, no. 3, pp. 4766-4773, July 2020.
- [110] I. Park, T. Smith and J. F. Love, "Thermal Design of Astrobee Perching Arm," 2019 *IEEE/SICE International Symposium on System Integration (SII)*, 2019, pp. 444-449.

- [111] A. Ramezani, “Towards biomimicry of a bat-style perching maneuver on structures: the manipulation of inertial dynamics,” 2020 IEEE International Conference on Robotics and Automation (ICRA), 2020, pp. 7015-7021.
- [112] H. W. Wopereis, T. D. van der Molen, T. H. Post, S. Stramigioli and M. Fumagalli, “Mechanism for perching on smooth surfaces using aerial impacts,” 2016 IEEE International Symposium on Safety, Security, and Rescue Robotics (SSRR), 2016, pp. 154-159.
- [113] C. E. Doyle et al., “An Avian-Inspired Passive Mechanism for Quadrotor Perching,” in IEEE/ASME Transactions on Mechatronics, vol. 18, no. 2, pp. 506-517, April 2013.
- [114] C. E. Doyle et al., “Avian-inspired passive perching mechanism for robotic rotorcraft,” 2011 IEEE/RSJ International Conference on Intelligent Robots and Systems, 2011, pp. 4975-4980.
- [115] Maozheng Xu, Takeshi Takaki, Mingjun Jiang, and Idaku Ishii, Development of Parallel-link-passive-gripper by Using a Multicopter’s Own Weight for Perching, Proceedings of the SICE Annual Conference 2019, pp. 431-432, 2019.
- [116] K. Nagarjuna and G. R. Suresh, “Design of effective landing mechanism for fully autonomous Unmanned Aerial Vehicle,” 2015 3rd International Conference on Signal Processing, Communication and Networking (ICSCN), 2015, pp. 1-6.
- [117] K. R. Chandra and S. Ghosh, “Hu-Moment-Based Autonomous Landing of a UAV on a Hemispherical Dome,” 2019 International Conference on Unmanned Aircraft Systems (ICUAS), 2019, pp. 19-25.
- [118] G. Lan, Y. Bu, J. Liang and Q. Hao, “Action synchronization between human and UAV robotic arms for remote operation,” 2016 IEEE International Conference on Mechatronics and Automation, 2016, pp. 2477-2481.

- [119] F. Ruggiero et al., “ A multilayer control for multirotor UAVs equipped with a servo robot arm,” 2015 IEEE International Conference on Robotics and Automation (ICRA), 2015, pp. 4014-4020
- [120] D. Bazylev, A. Kremlev, A. Margun and K. Zimenko, “ Design of control system for a four-rotor UAV equipped with robotic arm,” 2015 7th International Congress on Ultra Modern Telecommunications and Control Systems and Workshops (ICUMT), 2015, pp. 144-149.
- [121] G. Yamauchi, K. Nagatani, T. Hashimoto, and K. Fujino, “ Slip-compensated odometry for tracked vehicle on loose and weak slope,” *ROBOMECH J.*, vol. 4, no. 1, pp. 1-11, 2017.
- [122] P. G. Jayasekara and H. Arisumi, “ Surmounting obstacles by arm maneuver for unmanned power shovel,” *ROBOMECH J.*, vol. 2, no. 1, pp. 1-12, 2015.
- [123] K. Chen et al., “ Compound locomotion control system combining crawling and walking for multi-crawler multi-arm robot to adapt unstructured and unknown terrain,” *ROBOMECH J.*, vol. 5, no. 1, 2018.
- [124] D. Endo and K. Nagatani, “ Assessment of a tracked vehicle’s ability to traverse stairs,” *ROBOMECH J.*, vol. 3, no. 1, pp. 1-13, 2016.
- [125] S. Nakajima, “ Stair-climbing gait for a four-wheeled vehicle,” *ROBOMECH J.*, vol. 7, no. 1, 2020.
- [126] Ananta Adhi Wardana, Takeshi Takaki, Mingjun Jiang, Idaku Ishii, Development of a single-wheeled inverted pendulum robot capable of climbing stairs, *Advanced Robotics*, Vol. 34, No. 10, pp. 674-688 (2020).
- [127] K. Ohara et al., “ Energy-efficient narrow wall climbing of six-legged robot,” *ROBOMECH J.*, vol. 5, no. 1, 2018.
- [128] K. Yamamoto and T. Aoki, “ Development of novel mobile robot with semicircular wheels,” *ROBOMECH J.*, vol. 7, no. 1, 2020.

- [129] Y. Bai, J. -H. Hong and A. Zolotas, “Development of a Novel Water Landing UAV with Deflatable Floater,” 2019 Workshop on Research, Education and Development of Unmanned Aerial Systems (RED UAS), 2019, pp. 166-171.
- [130] Z. Zhao, J. Zhao and H. Liu, “An asteroid landing mechanism and its landing simulation,” 2012 IEEE International Conference on Robotics and Biomimetics (RO-BIO), 2012, pp. 205-210.
- [131] M. Xu, N. Sumida and T. Takaki, “Development of A Passive Skid for Multicopter Landing on Rough Terrain,” 2020 IEEE/RSJ International Conference on Intelligent Robots and Systems (IROS), 2020, pp. 1316-1321.
- [132] [http://dl.djicdn.com/downloads/flammewheel/en/F550\\_User\\_Manual\\_v2.0\\_en.pdf](http://dl.djicdn.com/downloads/flammewheel/en/F550_User_Manual_v2.0_en.pdf)

## Acknowledgement

Firstly, I would like to express my sincere gratitude to my advisor, **Prof. Takaki Takeshi**, who gave me an opportunity to be a member of the Smart Robotics Laboratory, Hiroshima University, and has guided me through these five years. From **Prof. Takaki Takeshi** I learned not only the skills, methods, experiences, but also the passion and attitude as a researcher, which can guide me in my future. I want to express my gratitude again to **Prof. Takaki Takeshi**.

Additionally, I would like to express my gratitude to **Prof. Ishii Idaku**, **Assoc. Prof. Taku Senoo**, **Assis. Prof. Mingjun Jiang**, **Assis. Prof. Shaopeng Hu**, **Designated. Assis. Prof. Sushil RAUT**, **Designated. Assis. Prof. Kohei Shimasaki**, and **Dr. Ananta Adhi Wardana**. They helped me overcome countless difficulties since I joined our laboratory.

I would like to express my heartfelt gratitude to **Ms. Yukari Kaneyuki**, and **Ms. Michiko Kanzaki** (educational administrator), and **Ms. Rumi Horiuchi** and **Ms. Arisa Tomura** (laboratory secretary). They were my most reliable staff in our laboratory, and I received thoughtful assistance both in life and my study.

I want to express my sincere thanks to the bachelor, master, and doctoral students in Robotics Laboratory for their help in my life and research.

Finally, I want to express my deepest gratitude to my family. They have supported everything possible for me no matter what difficulties I have. My success is inseparable from their support.

November, 2021

Xu Maozheng